Adaptive complex nanocomposite alloys for burning plasma-material interface tunability

DE-Grant # DE-SC0014267

FINAL REPORT

Submitted to the U.S. Department of Energy
Office of Science
Office of Fusion Energy Sciences (OFES)

Lead Principal Investigator: Jean Paul Allain, Professor, University of Illinois at Urbana-Champaign

Lead PI Institution: University of Illinois at Urbana-Champaign
Department of Nuclear, Plasma and Radiological Engineering
104 South Wright Street, 216 Talbot Lab, Urbana, IL 61801

DOE/Office of Science Program Office: Fusion Energy Sciences, SC-24.2
Topic: Materials Science and Enabling Technologies for Fusion

DOE/Office of Science Program Office Technical Contact: Mr. Daniel Clark

Point of Contact: J.P. Allain, University of Illinois at Urbana-Champaign
PI Contact: (217) 244-4789 (voice), (765) 765-9036 (cell)
(765) 333-4906 (fax)

Email: allain@illinois.edu

THIS PAGE LEFT BLANK

Executive Summary

The focus of this program is discovery and development of novel *self-healing* and *adaptive* materials for the PMI (plasma-material interface) envisioned for future plasma-burning extreme environments in thermonuclear fusion reactors that can provide enhanced radiation-tolerance or resistance. This program was conceived and stems from the PI's DOE Early Career Award work on harnessing nanotechnology and mesoscale materials design in refractory metals to address gaps in PMI research. These gaps pertain to the lack of understanding of multi-scale interactions at the plasma-material interface and the development of novel material interfaces that can be designed to adapt to extreme fusion reactor conditions. The final report is separated into two primary sections: The first section consists of the program's first two years (FY16-FY17) performance period. The second section consists of FY18 to FY19 period, where the FY19 period was a supplemental addition to support the completion of a PhD thesis and continuation of another. This work consists of an excellent team consisting of a co-PI, one postdoctoral researcher, two graduate students, two undergraduate students and collaborators both domestic and abroad.

The program has three primary objectives: **1) Processing of self-healing and adaptive complex materials for PMI, 2) High-heat flux testing and *in-situ* characterization, and 3) Multi-scale computational modeling of the plasma-material interface with these materials.** The overall goal of this program is to lay the foundation of developing advanced materials for the plasma-material interface that enable plasma-burning fusion reactor operation. Development of materials unique to these extreme conditions take extraordinary effort and the goal is to study very specific questions that motivate a more extensive development phase. The work in this program combines fundamental and applied research that establishes yet unknown process-composition-property relationships of novel "self-healing" and "adaptive" plasma-facing interfaces. To achieve this goal the PI has put together a team of both national and international collaborators to tackle some of the most elusive questions in fusion PMI to date. The PI brings a unique perspective of tailoring nano to mesoscale functionalities to control PMI properties such as ion-induced desorption, particle recycling, impurity emission, phase separation, fuel retention and sub-surface defect dynamics and tests these hypotheses on numerous platforms that capture various scales of extreme conditions expected in fusion reactors of the future. The program focuses on a range of studies from extreme-refined doped refractory metals (for optimum stabilization) to complex nanocomposites including the use of mesoporous metal systems as scaffolds for low-melting point metals (e.g. Li, Sn). The program is also exploring other novel materials for the PMI including: metallic glass, high-entropy alloys and self-autonomous materials. However, focus remains on W-based materials for now. The program also focuses on both surface/interface and thermo-mechanical properties under simulated PMI extreme conditions using state-of-the art *in-situ* characterization at various platforms both at UIUC and national/international centers. Although bulk properties of refractory alloys and porous-based systems are of interest to the program in general focus is on surface and near-surface properties relevant to plasma-material interactions and coupling. This unique focus establishes functional and performance research in areas that intersect surface chemistry and physics, materials science and plasma physics. The training of both PhD students and postdoctoral researchers reflects this philosophy in both academic settings and professional development including: conferences, peer-reviewed publications and seminar talks.

The program has enlisted some of the world's leading advanced fusion materials testing facilities (see section on Equipment, Facilities and External Resources for more detail). At the University of Illinois

at Urbana-Champaign the program has established a significant collaboration with Prof. Jessica Krogstad in the Department of Materials Science and Engineering. Along with co-PI Prof. Jim Stubbins, this effort has focused on the development of synthesis of dispersion-strengthened tungsten materials designed for fusion PMI applications using spark plasma sintered (SPS) techniques.

Section 1: FY16-FY17 Program Activities

Of the various materials options at the plasma-material interface in future burning-plasma magnetic fusion devices (i.e., graphite, liquid metals, etc.) refractory metals (molybdenum, tungsten etc.) are attractive for use during steady-state, high-temperature (700-1000 C) operation with heat flux ranging between 10-20 MW/m^2. However, both molybdenum and tungsten have serious performance issues regarding radiation tolerance (brittle fracture, hardening, swelling, transmutation, surface erosion even at relatively high temperature) and hydrogen retention/permeation that must be addressed to make them a viable option for steady-state burning plasma operation in fusion reactors (e.g. DEMO). As a plasma-facing material, additional tungsten limitations include: irradiation-driven nanostructuring on tungsten surfaces (e.g. morphology evolution), blistering and embrittlement of tungsten due to high exposure from hydrogen and helium irradiation, and extremely low tolerances for tungsten impurity emission into the core plasma. However, compared to low Z materials such as carbon and beryllium, tungsten's high melting point, high thermal conductivity, low tritium retention, and low plasma-induced sputter threshold has rendered it one of the best candidate materials for the extreme fusion environments (e.g., 0.1-1.0 dpa, > 5 MW/m^2) encountered, for example, in the ITER burning plasma.

Given most of the attention in PMI has focused on conventional solid PFCs, there is a critical need for both fundamental investigation and translational development of transformative PFC technologies to meet the demand of reactor-relevant material interfaces facing the plasma. This program builds on the work from Prof. Allain's DOE Early Career Grant (DE-SC0004032, *Harnessing nanotechnology for fusion plasma-material interface research in an in-situ particle-surface interaction facility*), which investigated both processing and high heat-flux performance of extreme-refined and multi-modal grained tungsten as a robust class of PMI materials. **In this program we leverage this knowledge to investigate novel *self-healing* and *adaptive* materials for the PMI (plasma-material interface) that can provide enhanced radiation-tolerance or resistance. The context is focus on the plasma-material interface and the systems studied range from extreme-refined doped refractory metals (for optimum stabilization) to complex nanocomposites including the use of mesoporous metal systems as scaffolds for low-melting point metals (e.g. Li, Sn). We focus on both surface/interface and thermo-mechanical properties under simulated PMI extreme conditions using state-of-the art *in-situ* characterization.**

The program focuses on tungsten-based materials and alternates that are introduced as either a bulk plasma-facing material of few mm thickness materials (i.e. envisioned to be harnessed or coupled to a thicker substrate tile) or a coating with properties that can have a positive effect on the edge plasma (e.g. reduction of erosion, reduction of heat flux deposition, lower Zeff, among others). Coupling of the refractory alloy to low-Z ultrathin films (e.g. lithium, boron, etc.) is explored along with low atomic concentration doping at grain boundaries. In addition, non-traditional materials such as porous and hierarchical structures at the nano and mesoscale as scaffolds for liquid metals are also explored. The materials design approach adopted here will also investigate and establish a new class of materials systems for the PMI. These materials could have either self-healing properties where "self-healing" is

defined as materials that freely can repair themselves after damage without any external influence from their environment; or adaptive materials properties. Where "adaptive" is defined as *intrinsic* properties coupled to an external influence (e.g. radiation stimulant), whereby during exposure to a defined extreme environment the material performance is maintained or improved. This paradigm to PMI materials design is transformative in that the design of the plasma-material interface is closely coupled with its behavior under well-defined magnetic fusion plasma edge conditions and studied with robust *in-situ* performance characterization to decipher the *dynamic* material properties as they evolve during plasma exposure and thus help define the processing schemes to design the same. The overall program explored these complex refractory metal-based systems from both a process-structure-property point of view and also for their plasma-material interaction (PMI) functionality. PMI properties studied include: multi-component thermal, physical and chemical sputtering, surface charge dynamics, ion reflection, ion-driven surface segregation and diffusion, ion-induced mixing, and surface topography.

Key Achievements of the Program to Date (Sept 2015 through Sept 2017)

- Discovery of the balance of low-Z to high-Z interaction during high duty cycle plasma exposures (e.g. Li on W) and surface coverage (Neff)
- *In*-operando He/D interactions on low Z to high Z systems and fuel retention (Neff)
- Synthesis of DSW with SPS (Lang)
- Synthesis of porous W (Lang, Kapat)
- Wettability of nano to mesoporous W with liquid Li: new temperature window (Kapat)
- Pre-irradiated W exposed to high-fluence D/He plasmas (Lang)
- *In-situ* measurement of sputter yields from dispersion-strengthened W (Lang)
- Establishing the methodology to measure hydrogen content in irradiated surfaces (Neff)

Key Results of the Program (FY 16 to FY 17)

The following are some of the key highlights and results of the program from September 2015 to September 2017.

Synthesis, characterization and testing of dispersion-strengthened tungsten and PMI properties

Tungsten (W) is the current plasma-facing material of choice for divertor region of fusion reactors for its high melting point and high sputtering threshold; however, it is not without its issues. Under low energy He irradiation, W develops surface nanostructures that alter its plasma-facing properties [Nishijima 2004]. Also, W is an intrinsically brittle material, exhibiting intergranular fracture below ~300-400 C, and is further embrittled under irradiation [Zinkle 2000]. In order to address these issues, a variety of approaches have been taken including the development of nano-grained W via severe plastic deformation and spark plasma sintering methods, which have exhibited enhanced ductility and radiation tolerance [El-Atwani 2015, El-Atwani 2017, El-Atwani 2014, El-Atwani 2013]. However, these materials also undergo rapid grain growth and are unstable at high temperature [Suslova 2014]. A second class of materials is dispersion-strengthened W alloys, which are tungsten materials micro-alloyed with small amounts of transition metal carbides added to capture impurity oxygen atoms to purify grain boundaries. The second phase additions

pin W grains and may enhance grain boundary cohesion to increase ductility [Xie 2015, Kitsunai 1999]. Work at UIUC has focused on the development of advanced, W-based alloys and testing of their PMI properties.

This class of novel tungsten materials for PMI applications under investigation at UIUC in collaboration with Dr. Jessica Krogstad of the Materials Science and Engineering Department is dispersion-strengthened tungsten (DS-W) alloys, which are fabricated with varying amounts (1-10 wt.%) of TiC, TaC, and ZrC in order to study the effect of the second phase on the material performance under irradiation. Samples are fabricated via spark plasma sintering (SPS), a rapid consolidation, advanced manufacturing technique that produces dense, fine-grained samples in minutes [Groza 2000]. Tungsten powder is mixed with the alloying element and loaded into a graphite die for sintering, during which a pulsed DC current joule heats the powder and an applied uniaxial load compresses it. Upon heating to 1800°C at 100°C/min under a uniaxial pressure of 60 MPa for 3 minutes, consolidated alloys to ~95% relative density are produced.

The rapid consolidation nature of SPS produces samples with micron-sized grains, with the grain size decreasing as the amount of dispersed second phase increases. The addition of the second phase provides a clear grain pinning effect, with dispersoids distributing at W grain boundaries to limit W grain growth during fabrication to 1 μm in size, down from 11 μm without a second phase present, indicated in **Fig. 1**. Compositional analysis with XRD and XPS shows the formation of transition metal oxide and tungsten carbide phases, indicating that the second phase materials capture oxygen impurities. The formation of oxides indicates that oxygen atoms are not isolated within tungsten grain boundaries, which should enhance grain boundary cohesion and ductility.

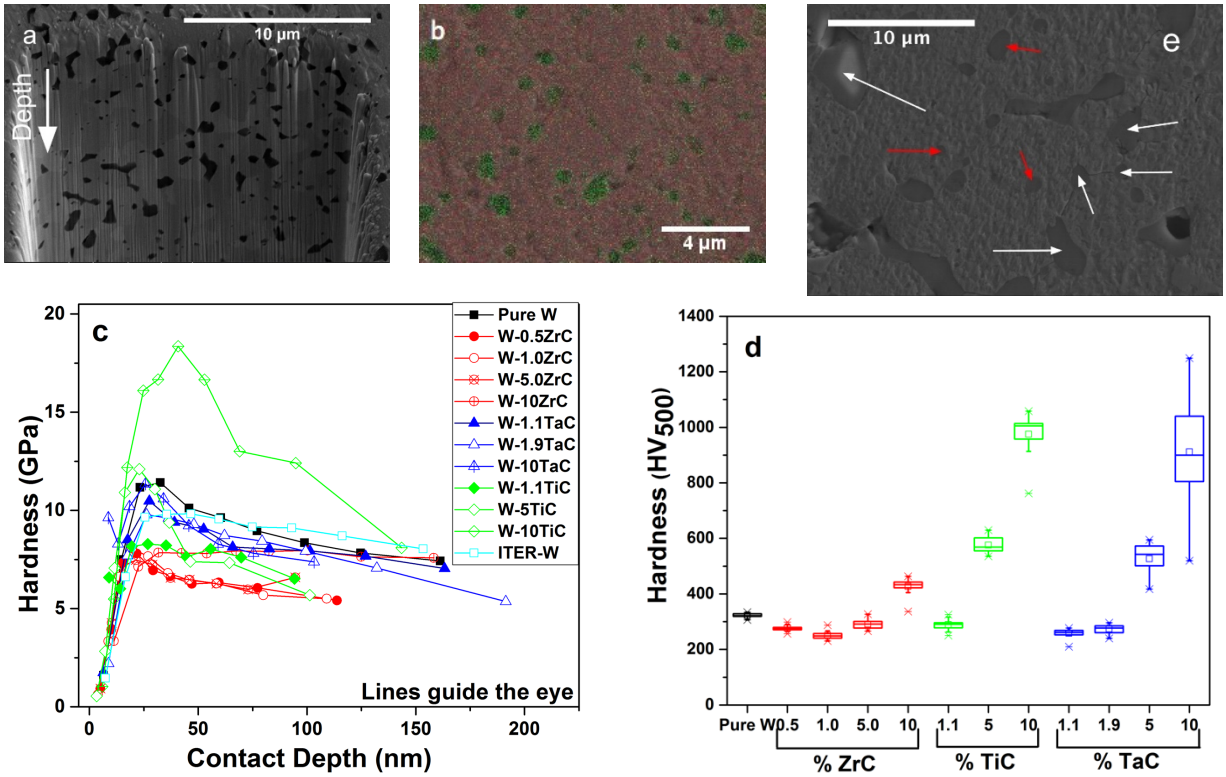

Figure 1: a) Cross-sectional FIB depth profile of a W-10TiC alloy showing TiC particles (black) present in W grain boundaries (W grains visible as light grey) providing a pinning effect. **b)** EDS map of a W-5TiC sample showing micron-sized Ti-rich dispersoids (green) within the W (red) matrix. **c)** Nanoindentation hardness as a function of contact **d)** Hardness as function of sample composition **e)** SEM micrograph of W-5TaC sample showing TaC precipitates intergranularly (white arrows) and intra-granularly (red arrows).

A grain boundary pinning effect is observed as Vickers hardness values increase as the amount of second phase is increased (shown in **Fig. 1c-d**), with TaC and TiC additions providing an increased hardening effect versus ZrC. The hardening increase can be attributed to the introduction of an intrinsically hard second phase providing second phase strengthening, the reduction in tungsten grain size (results indicate a Hall-Petch type relationship), and grain boundary pinning provided by the second phase particles. The enhanced hardness of the W-10TiC vs. W-10TaC sample as measured with nanoindentation can be attributed to a larger fraction of the surface covered with TiC vs. TaC, resulting in a higher likelihood of the indenter tip hitting a TiC region vs. TaC region.

Ultrafine-grained W under high heat flux exposures has exhibited rapid grain growth, nullifying the benefits provided by the initial fine-grained microstructure [Suslova 2014]. Thus, the ability to maintain a fine microstructure at high temperatures, such as those reached during transient events in reactors, remains an important hurdle for advanced W materials. Annealing of pure W and W-ZrC alloys to 1000-1600°C showed that the alloys did not undergo recrystallization. As shown in **Fig. 2a** a pure W sample exhibited a drop in hardness between 1200°C and 1400°C while the alloyed samples exhibited no drop in hardness. Also, EBSD analysis, shown in **Fig. 2 b-c, i**ndicated that the W-1.0ZrC sample maintained its fine grain size after annealing, while the pure W sample showed clear grain growth. This result indicates that the addition of small amounts of ZrC to W can effectively pin grain boundaries and prevent grain growth during high temperature exposure. Thus, DS-W alloys can overcome the limitations of nanocrystalline W and prevent grain boundary migration. Further studies of other alloys and exposures to higher temperatures are needed to determine if the DS-W materials all exhibit enhanced recrystallization resistance by providing grain boundary pinning. Additionally, bulk mechanical tests, such as tensile testing of these alloys, are underway to determine if these alloys alter the ductile-to-brittle behavior of tungsten.

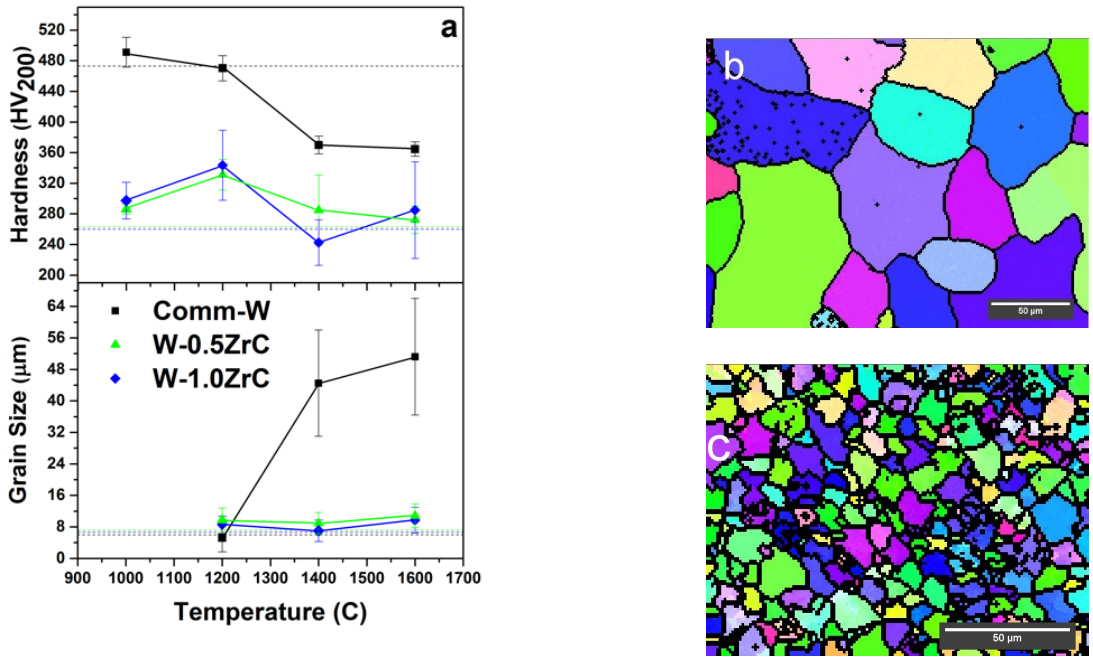

Figure 2: a) Vickers hardness and average grain size as a function of annealing temperature **b-c)** EBSD map of a pure W sample after annealing at 1600°C (**b**), and a W-1.0ZrC sample after annealing at 1600°C (**c**)

Despite the amount of bulk mechanical testing needed for DS-W materials, there is a fundamental lack of understanding of their behavior under irradiation and their PMI properties. Our ability to test the fundamental response of these materials to low-energy ion irradiation demonstrates the unique aspects of our work. The IGNIS facility at UIUC is the ideal platform to study early stage, ion-induced damage in these materials and their corresponding surface chemistry changes in-situ during irradiation in order to elucidate the impact of the second phase particles on surface chemistry, morphology, and advanced PMI properties such as sputtering and hydrogen retention. Under exposures to 250 eV D ions to a $1x10^{17}$ cm^{-2} fluence, these alloys demonstrate no surface blistering, and in-situ XPS demonstrates that the surface composition remains unchanged after irradiation. Exposures to 250 eV He ions to a $1x10^{20}$ cm^{-2} fluence begin to alter the material surface. At 600°C, rippling nanostructures are observed in Ti-rich regions the TiC-alloyed samples, while these regions appear set-back from the flat W surface. However, no nanostructuring is observed in Ta- or Zr-rich regions in the other alloys. Similarly, no damage is observed on the W grains in the alloys or on a pure W reference. Irradiations at 800°C induce more significant changes in the W surface morphology. Ripples and pores begin to emerge on all W grains, regardless of the amount and type of added second phase. At a $1x10^{20}$ cm^{-2} fluence, early-stage damage features such as nano-pores (~10nm in size) are observed on W grains, with no clear difference in the distribution or size of the pores on alloyed vs. unalloyed samples or on the amount of added second phase.

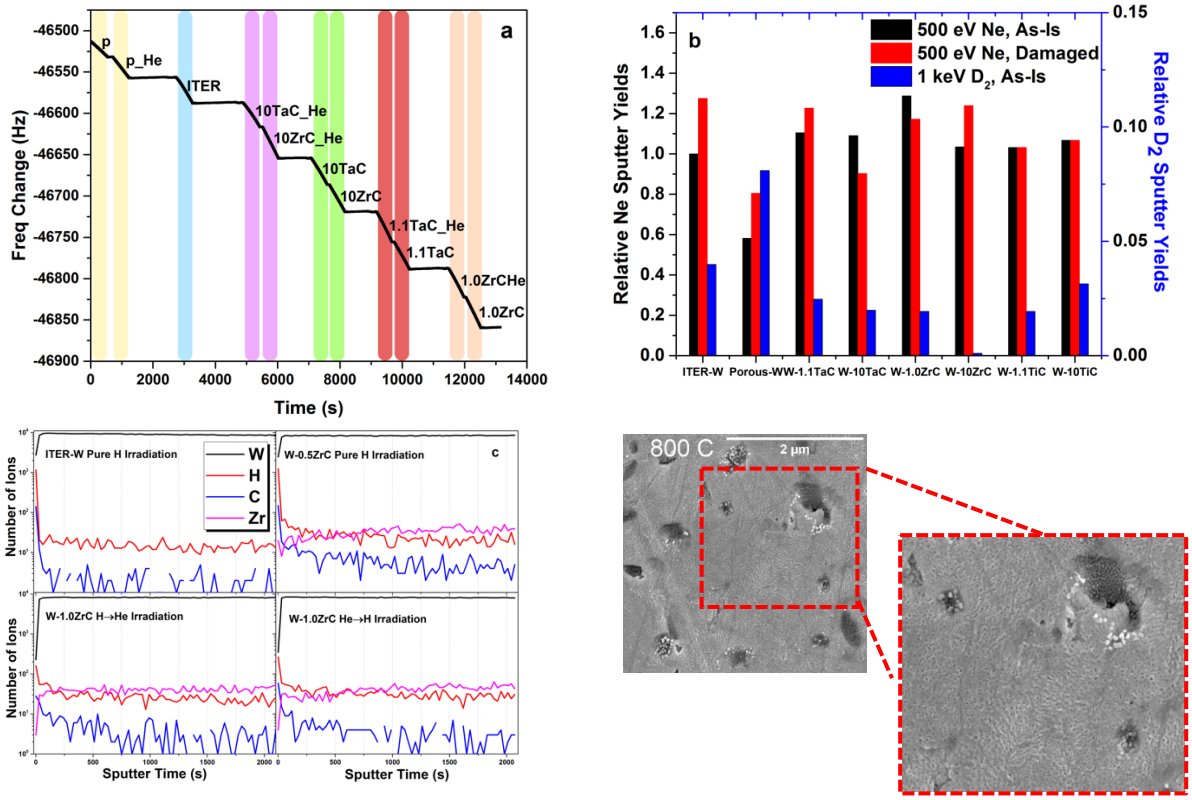

Figure 3: a) In-situ QCM-DCU Frequency change as a function of time recorded by the in IGNIS. **b)** Relative sputtering yields of W-based materials induced by ion irradiation as indicated. **c)** SIMS depth profile of the pure W and W-alloy samples exposed to high fluence H/He irradiations at Magnum-PSI. **d)** SEM micrograph of a surface of a W-1.1TiC alloy after He irradiation to $1x10^{20}$ cm^{-2} at 800°C demonstrating appearance of W surface pores and advanced surface nanostructuring in the Ti-rich regions.

On a pure W sample, ~200nm wide polyp-like protrusions off the surface are observed at grain boundaries. These structures are not observed on most W-alloys, indicating pure W may show damage at advanced stages. No nanostructures were observed in the Ta-rich regions of W-TaC and only sparse features observed on Zr-rich regions of W-ZrC alloys, indicating that those second phases resist nanostructure formation under these irradiation conditions. This result is consistent with experiments done under similar conditions with W-Ta alloys which demonstrated a higher fluence threshold necessary for fuzz formation [Gonderman 2017]. The 10 wt.% alloys, which had the smallest grain size, still exhibited W nano-pores, indicating that the grain size reduction from 11-1 µm did not trigger grain boundary-mediated reduction in He-induced surface morphology. However, the addition of 10 wt.% TaC limited the formation of nanostructures over the largest surface area due to the presence of Ta-rich regions covering a large portion of the surface. Thus, ZrC and TaC alloying may offer the most resistance to He-induced morphology damage.

Investigation of the fundamental PMI sputtering properties of the W alloys, investigated with Ne and D ions at 30° incidence before and after He ion irradiation in-situ in the IGNIS facility, further expands our knowledge of the surface properties of the alloys. **Figure 3a** shows the frequency change of the quartz crystal microbalance-dual crystal unit (QCM-DCU) as a function of time. The slopes of the linear portions of the plot can be examined to extract relative sputter yield

information. As shown in **Fig. 3b,** compared to a smooth, pure W sample, all the alloys have marginally higher sputtering yields under 500 eV Ne ion bombardment, but lower yields under 1 keV D ion bombardment. Pre-damaging with 250 eV He ions (as described above) increases the sputtering yields for both pure W and DS-W alloys as compared to undamaged samples; however, the damaged alloys have lower sputtering yields than the damaged pure W sample, perhaps because a smaller fraction of the surface is nanostructured due to the presence of non-structured second phase dispersoids (as in the W-10TaC alloy described above). High-fluence studies were conducted at Magnum-PSI in DIFFER to elucidate on the latter stages of PMI damage. Hydrogen plasma exposures to fluences of about 10^{22} cm^{-2}, resulted in no nanostructuring. However, with sequential H to He irradiations at fluences of 10^{22} cm^{-2} and 10^{21} cm^{-2}, for H and He, respectively, fine tendril structures in some regions of the surface were observed of a W-1.0ZrC DS-W. H retention was examined in these samples for the first 100 nm with SIMS and depth profiles are shown in **Fig. 3c.** Data suggests the DS-W samples retained more hydrogen relative to the control W sample. More work is needed with TDS to determine how H is retained and how much. **Fig. 3d.** shows the resultant surface nanostructure.

Studies of low-Z to high-Z complex composites

Studies of low-Z coatings with high-Z refractory alloy substrates were conducted during the first two years of this program under various irradiation conditions. The premise of this work was to explore the plasma-material interaction (PMI) properties of low-Z coatings (i.e. lithium-based coatings) on refractory metal substrates. In particular, the surface migration properties of Li coatings on irradiated W substrates. Two primary experimental thrusts of this work consisted of: 1) low-fluence (early stage) irradiation interactions to understand Li surface and sub-surface migration as well as sputtering and mixing, and 2) high-fluence, high-temperature conditions to test the limits of Li surface resilience. One hypothesis also explored the ability for lithium mixing in tungsten to suppress the growth of fuzz on the basis of earlier work by Baldwin and Doerner [Baldwin 2009] using metal-doped (i.e. Be, C) He/D plasmas suppressing fuzz growth.

Low-fluence, early-stage irradiation of Li/W surfaces: Early-stage Li/W surfaces were examined with *in-situ* surface characterization with the new IGNIS facility at Illinois. The facility is currently under development in this program with complementary surface-sensitive characterization *during* high-fluence particle irradiation under fusion-relevant conditions of: ion energy, incident angle, temperature, gas pressure and multi-beam exposure. Krstic and Allain [Krstic 2013, Taylor 2011, Taylor 2013, Taylor 2014] discovered enhanced D retention in lithium-treated graphite surface by local oxygen content. In this work, mixed He/D beams are used to study PMI surface properties of Li/W finding that He ions break apart the Li-O-D complex synergistically during He/D irradiation thus reducing overall D retention while simultaneously suppressing D bulk diffusion [Neff 2014].

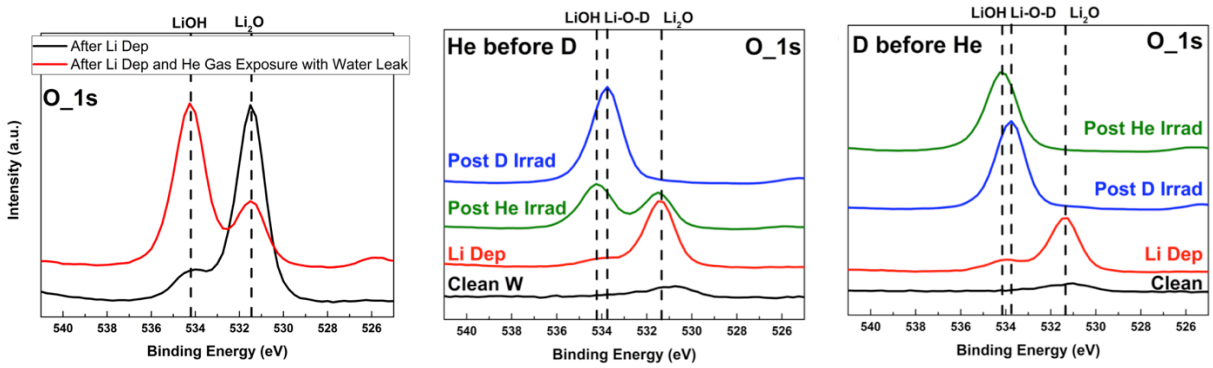

Figure 4: (left) Control test of Li-O-H complex to test H2O exposure during He irradiation for a case with a water vapor influx (red) and without (black). Two sequenced tests to examine role of irradiation-driven effects by energetic He ions.

The irradiation-driven effects on Li-coated W surfaces are critical in determining retention of fuel-based particles in fusion reactors. One key aspect of the surface kinetics discovered in this work was the identification of the role oxygen plays on fuel retention. *In-situ* and *in-operando* irradiation studies were conducted in IGNIS facility at UIUC. A sequenced study was conducted to decipher how D and H atoms were retained in Li-coated/W systems during energetic exposure to D particles. Experiments tested the hypothesis that oxygen in lithium coatings would enable retention of D during D plasma exposure reducing oxygen from ambient water in the system (e.g. vacuum H2O of about 10^{-8} torr comparable to existing and future fusion tokamak vacuum environments). The level of retention would be controlled by energetic He particles given their inert state and kinematic energy match with H and D complexes in Li. This synergistic effect between He and D irradiation has been observed to increase the retention of D atoms near tungsten surfaces, however very little is understood on how low-Z coatings would influence this retention.

In one test, after deposition *in-situ* of Li on W, surfaces were exposed to He plasmas (to avoid chemical effects from the energetic beam and isolate those with background water vapor) combined with water vapor exposure. **Fig. 4** for post-He irradiation shows a distinct LiOH peak identified in the O1s region spectra and an associated Li2O peak due to breakdown of water on the surface of lithium coatings. However, when water vapor is not present and a D2 beam used (with same kinetics e.g. 4 amu as those of He irradiations), the post-D irradiation surfaces show a Li-O-D complex without Li oxide showing that the oxide on Li reduces completely to the Li-O-D complex at 533.5 eV. This discovery was supported by computational modeling results in collaboration with P. Krstic. A control experiment was used as a standard to determine the Li-O-H peak at 534 eV with controlled water vapor exposure and without after lithium deposition on W. This Li-O-D functionality is then found to be controlled *and decreased* by inserting a gradual increase of He ion flux with D beams on the sample surface testing the ability to tune D retention with He energetic particles. This result is shown in figure below. First results of *in-operando XPS* with He/D ions on lithiated W surfaces are shown in **Fig. 5**. The significance of these results is the high-pressure XPS measurements demonstrates how significant mTorr level gas *combined with irradiation of D ions* work to synergistically entrap D atoms on the Li/W surfaces. This is the first time such a mechanism is measured and indicates that the enhanced D trapping may in fact be driven by combined energetic and thermodynamic mechanisms at the complex Li/W surfaces. More importantly even a small percentage of He is found to *significantly decrease this entrapment*

mostly due to the weak bonding of D in the Li/W system that is the result of the intrinsic synergy between D and He on the surface. The last year of the program is investigating the role of this mechanism beyond Li-based coatings and into pure and complex W-based fusion-relevant materials.

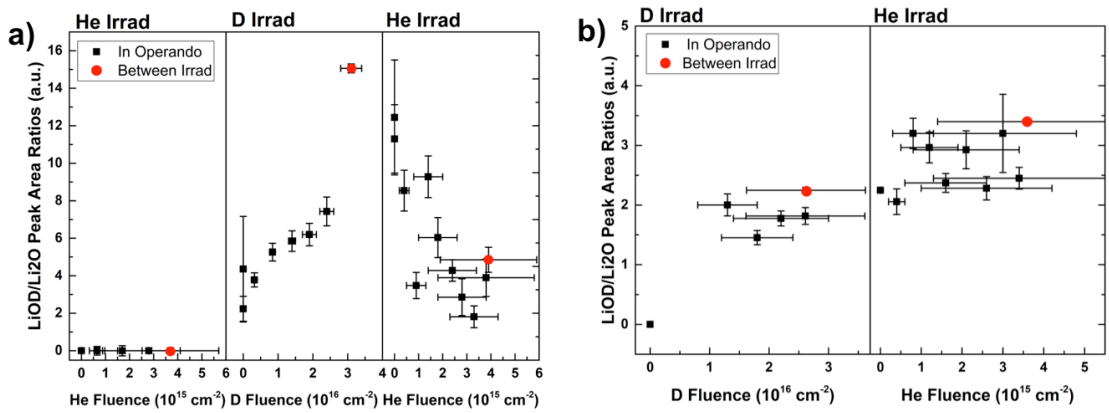

Figure 5: (a) *in-operando* LiOD/Li2O peak area ratio derived from O1s XPS spectra of Li/W system exposed to He irradiation sequenced by D irradiation and He irradiation showing the effect of ballistic bond-breaking mechanism of He of the LiOD surface complex. (b) D irradiation followed by simultaneous He irradiation with water vapor exposure showing enhanced LiOH from oxygen reduction during irradiation.

High-fluence high-temperature Li/W surfaces: Experiments in Pilot-PSI at DIFFER tested W substrates with low-Z Li coatings at the conditions to produce fuzz. Although work by the PI and El-Atwani (El-Atwani 2013) found surface W grain orientation played a role in surface nano-patterning at pre-fuzz fluences, no effort in these experiments were conducted with the intention of testing various W samples with different surface texture (e.g. orientation of grain crystallographic orientation). Lithium layers of thicknesses of ~2 um were deposited on coarse grained, refined grained, and ITER reference grained W and exposed to a He plasma in Pilot-PSI with energies of 35 eV and flux of 1-2x10^{23} $m^{-2}s^{-1}$ up to a fluence of 1-2x10^{26} m^{-2} at a T_{surf} of 1200°C or 900°C. To monitor the Li emitted of the surface during irradiation, optical emission spectroscopy (OES) monitored the Li I line. Following irradiation, SEM and FIB-SEM showed that Li did not affect the appearance or thickness of W fuzz. However, with the use of secondary ion mass spectroscopy (SIMS), we observed that Li does persist on the surface when compared to control samples even at temperatures above 900 °C. To determine where among the fuzz the Li persisted, electron energy loss spectroscopy (EELS) was used to map lithium on the fuzz tendrils. Additional studies also examined Li percolation and wetting properties within the nanoscale tendril porous structure to determine possible self-healing properties. Leveraging from this work on Low-Z/High-Z systems, the program established a novel approach combining multi-scale hierarchical structures to control micron-scale liquid-metal integration on a nano to mesoporous scaffold structure as a potential PFC. Details in next section.

Synthesis, characterization and testing of nanoporous and mesoporous W and PMI properties

A low-Z/high-Z hybrid system combining multiple phases (e.g. solid and liquid) may address some concerns intrinsic to pure solid materials and free-surface flowing liquid-metal systems. The concept proposed here was to devise a material system that combined a ductile phase (in liquid metal form) combined by a mesoporous phase (to provide stability to the LM) enabling adaptation to irradiation to energetic plasma particles and heat flux. By exploiting the external stimulus of particle and heat fluxes and utilizing a "healing/shielding" agent i.e. Li, to delay the onset of mechanical failure and mitigate its propagation [White 2011]. The incoming flux can induce segregation of Li embedded in a W structure as a protective layer between exposed W and form a protective vapor cloud via evaporation above the PFC to reduce incident heat flux through radiative dissipation [Eden 2016]. Porous W would be an ideal scaffold for a liquid metal, with the porosity tunable to a desired balance of surface wetting and evaporation to reach optimal edge plasma conditions. Recent work [Jaworski 2013, Abrams 2015] demonstrated that surface structure can have a significant effect on the stability of a free-surface flowing LM exposed to PMI fusion conditions. Earlier work demonstrated that LM can percolate into micron-scale topography of a refractory metal and thus provide an ideal hybrid system combination for PMI LM delivery. At Illinois development of porous tungsten via spark plasma sintering (SPS) is currently being tested both for mechanical properties and PMI properties. With the tunability of controlled porosity and presence of liquid metal, it is hypothesized that a hybrid system, when exposed to the particle fluxes and heat loads of a burning plasma fusion device, can mitigate the heat and particle flux and provide a self-healing material interface. Additional conjectures have also considered local reductions of mechanical/structural stress while maintaining higher thresholds from detrimental surface morphology induced by high temperature and high-fluence He irradiation conditions on refractory metal surfaces. This program examines both the surface wetting ability of hierarchical porous refractory metals (e.g. W or Mo alloys) as well as PMI properties and thermal-mechanical properties. Beyond SPS, the PI is currently establishing a collaboration with additive manufacturing experts to design tailored PMI hierarchical scaffolds for these hybrid systems whereby both PMI and thermal-mechanical properties can be tuned to desired function.

In the period between FY16-FY17 synthesis of mesoporous tungsten PFCs was developed with SPS. While SPS was used to create >90% dense W samples, altering the fabrication parameters allows the design of ~60-70% dense materials, demonstrating the versatility of SPS and its ability to synthesize a variety of novel materials. Utilizing 50-nm W powder, shown in **Fig. 6a**, and sintering under 40 MPa uniaxial pressure to a maximum temperature of 1050°C, porous samples, shown in **Fig. 6b**, were created. While the porosity is not well-controlled or cellular in nature, interconnected pores are created which can act as a sufficient bed for liquid metals, such as Li-Sn nanoparticles shown in **Fig. 6c**.

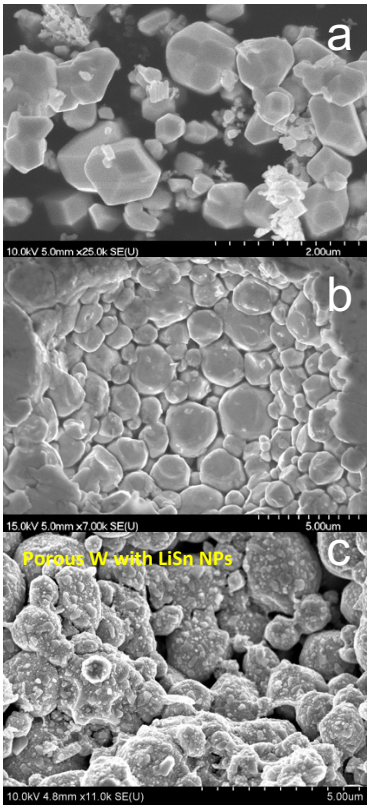

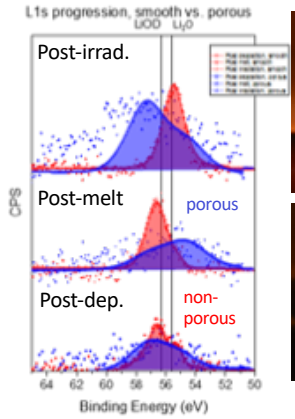

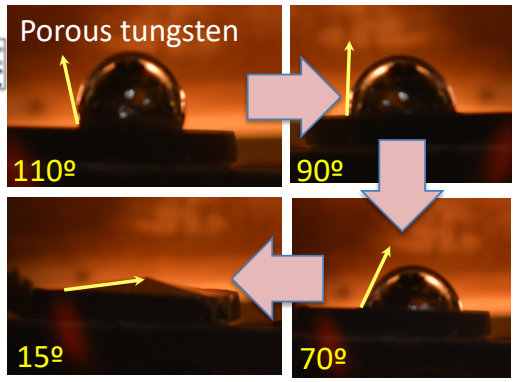

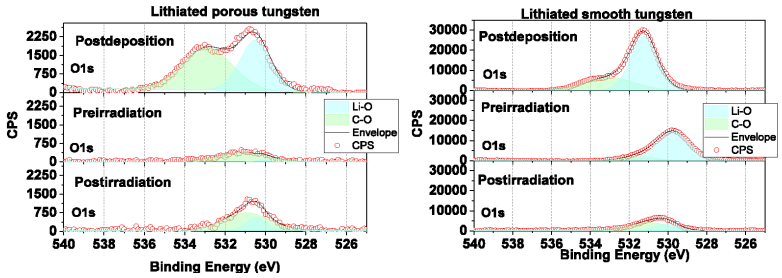

Figure 6 (left): (a) 50nm W powder used **b)** 70% dense porous W via SPS **c)** Li-Sn nanoparticles integrated within porous W **Figure 7 (top right):** Wetting and percolation process at 350°C in the span of 9 seconds **Figure 8 (bottom right):** XPS spectra of O_1s regions of lithiated porous and smooth W.

Effective lithium wetting on the porous tungsten substrate is critical for minimizing lithium ejection from the wall, and mitigating damage such as cracks in the porous substrate itself. Additionally, lithium wetting will impact processes such as retention, and surface replenishment from the bulk to the surface. Experiments were conducted in the MCATS test stand at the Center for Plasma Material Interactions (CPMI) to visually characterize the wetting angle of a lithium droplet on the porous substrate at various temperatures. The results shown in **Fig. 7** indicates complete wetting (contact angle ~ 0°) as early as 250°C, compared to the wetting temperature of lithium on smooth tungsten at 337°C to 349°C to get an acute wetting angle, depending on the surface treatment [Fiflis 2014]. Further, **Fig. 7** shows the percolation process of the lithium droplet into the porous bulk within 10 seconds of the dropping onto the 350°C surface. One of the key plasma material interactions to consider is the hydrogen isotope inventory within a plasma facing components. Experiments were done at the MIT DIONISOS facility to quantify the about of deuterium retained as well as the depth profile of the lithium and deuterium within the material with *in-operando* Elastic Recoil Detection (ERD). Accompanying XPS data are shown in **Fig. 8.**

Approximately one micron of lithium was deposited onto a porous tungsten sample and then heated to ~180-270°C; a high energy O^{4+} analysis beam (8900eV) was incident on the sample, during which a lithium peak is seen, shown in **Fig 9**., where Li is expected according to SIMNRA simulations, A The sample was then irradiated with a deuterium plasma to a fluence of ~ 1.2×10^{19}

cm^{-2}. Throughout the irradiation, as well as before and after Li deposition, a low energy O^{3+} analysis beam (7200eV) was incident on the sample to obtain spectra with resolvable lithium and deuterium peaks (such is not possible with the high energy beam since there is an overlap of deuterium and lithium at the higher energy), which is seen in **Fig. 9**. In **Fig 9**, lithium is seen (located as predicted by SIMNRA) following deposition.

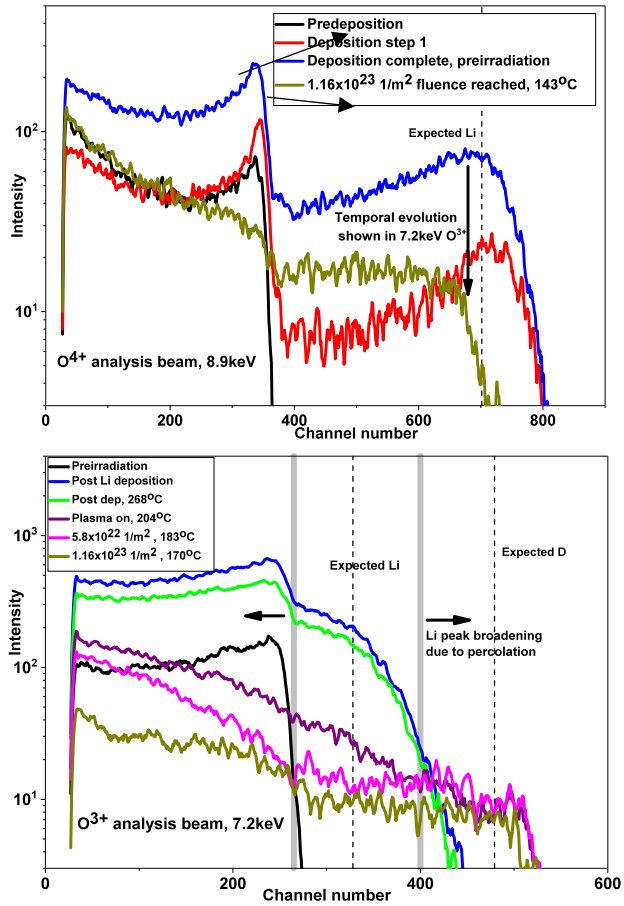

Figure 9: (a) ERD spectra before, during and after Li deposition as well as after irradiation obtained with a high energy oxygen analysis beam. **(b)** ERD spectra before, during and after deuterium irradiation as well as after Li deposition, obtained with a low energy oxygen analysis beam. The blue and dark yellow plots correspond to the same steps, so the evolution in between, during irradiation is shown in the low energy analysis beam plot

During the irradiation process, the lithium peak is seen to broaden in signal. Furthermore, a signal is detected where deuterium is expected as the irradiation starts but there are no conclusive results as to the behavior of the deuterium throughout the irradiation. The broadening of the lithium signal is indicative of percolation into porous substrate and this mixing with the substrate is responsible for the broadening of energy spectra. It is undetermined whether or not deuterium is following the lithium behavior, indicative of deuterium retention within the percolating lithium. Further studies will be conducted with Nuclear Reaction Analysis to investigate. One of the conjectures behind the porous tungsten design was that the increased surface area (per volume) will act as a defect sink and thus decrease the amount of intra-grain He nucleation for a given fluence of He, increasing

the fluence threshold for surface morphology. The samples exposed in the previously described He chemistry experiments had their surfaces examined with *post-mortem* using Scanning Electron Microscopy to look for any induced morphology.

Program Summary and Conclusions for FY16-FY17

The FY16-F17 activities have been very successful in establishing the synthesis and characterization capabilities at Illinois and with key partners. Significant progress has been made to identify synthesis parameters of SPS-based tungsten dispersion-strengthened composites and porous W. The focus of this program has been to develop these materials with focus on the PMI properties. Great value from key collaborations both in the U.S. and abroad has expanded these studies resulting in testing of Illinois materials across multiple fusion-relevant exposure platforms. Although the first two years have been very successful there remains some important challenges. The process-structure-property development for W-based materials and how PMI induces dynamic changes to these properties are still to be determined. Although, great progress was made with wetting and sputtering mechanisms the remaining links to high-fluence damage of these interfaces and understanding how to define "damage" from a PMI perspective (e.g. whether indeed these nanoscale morphology is *detrimental* to fusion performance) remains an open question. The last year is currently focused on thermos-mechanical testing and correlations to structure as well as computational modeling of the surface impurity interactions with metallic-based substrates effecting fuel retention.

BIBLIOGRAPHY & REFERENCES CITED:

References:

Baldwin M.J., et al., *J. Nucl. Mat.* 390-391 (2009) 886-890
Eden G.G, T. W. Morgan, U.B. Aussems, et al., Phys. Rev. Lett. 116, (2016)
El-Atwani, O., et al. *J. Nucl. Mater*. **434** (2013) 170–177.
El-Atwani, O., et al. *Nucl. Fusion* **54** (2014) 083013.
El-Atwani, O., et al. *Sci. Rep.* 5, 18207 (2015)
El-Atwani, O., et al. *Fus. Engr. Des.* 93 (2015) 9-14.
El-Atwani, O. et al. *Mat. Res. Lett.* 5:5 (2017) 343-349
Evitkhin V.A. et al. Plasma Phys. Control. Fusion 44 (6) (2002) 955-977
Fiflis P. et al. *Fusion Eng. And Des.* 89 (2014) 2827-2832
Ghoniem, N. et al. *Appl. Surf. Sci.* 331 (2015) 299-308
Gonderman, S., et al. *J. Nucl. Mater.* **491** (2017) 199-205.
Groza, J., et al. *Mater. Sci. and Eng. A* **287** (2000) 171–177.
Kitsunai, Y., et al. *J. Nucl. Mater*. **271&272** (1999) 423-428.
Lang. E. et al. *Nucl. Mat. Energy* (2017)
Mazzitelli G., et al. *Fusion Eng. Des.* 86 (2011) 580-583
Neu R. et al. *Physica Scripta* T138 (2008) 01403
Neff. A. et al. *J. Nucl. Mat.* 463 (2014) 1147-1151
Nishijima, D., et al. *J. Nucl. Mater.* **329–333** (2004) 1029–1033.
Ou W. et al *Nuclear Fusion* 55 (2015) 043015
Roth J., *Nuclear Fusion Research* 78 (2005) 203-224
Suslova, A., et al. *Sci. Rep*. **4**, 6845 (2014).
Taylor, C.N., et al. *J. Appl. Phys.* **109**, 053306 (2011)
Taylor, C.N., et al. *J. Nucl. Mater.* **415**, (2011) S777-S780
Taylor C.N., et al., *Phys. Plasmas* 21 (2014) 057101
Taylor C.N., et al., *J. Appl. Phys.* 114 (2013) 223301
White S.R., J.F. Patrick, M.J. Robb, N.R. Sottos et al. Nature 540, 363-370 (2011)
Wright, G.M., et al. Rev. Sci. Inst. 85, 023503 (2014)
Xie, Z. M. et al. *Sci. Rep*. **5**, 16014 (2015).
Zinkle, S.J., et al. *Fusion Eng. and Design* **51–52** (2000) 55–71.

PRODUCTS:

Theses:

1. A. Neff. *Dynamic interactions between energetic D and He ions on lithium-tungsten plasma-facing interfaces.* Ph.D. Thesis. University of Illinois at Urbana-Champaign, USA. 2017.

2. E. Lang. *Synthesis, characterization, and properties of carbide dispersion- strengthened tungsten alloys for use as a plasma-facing material in nuclear fusion reactors*. Master's Thesis. University of Illinois at Urbana-Champaign, USA. 2017.

3. A. Kapat, *Design and characterization of novel liquid metal-porous tungsten hybrid systems for plasma-material application in nuclear fusion reactors*. Master's Thesis University of Illinois at Urbana-Champaign, USA. 2018.

Papers:

1. E. Lang, N. Madden, C. Smith, J. Krogstad, J.P. Allain. *Microstructural and compositional effects of transition metal carbide additions on dispersion-strengthened W alloys fabricated via spark plasma sintering.* International Journal of Refractory Metals and Hard Materials. Submitted Jan 2018.
2. E. Lang, et al. *Elucidating that role of second phase particles on fuel retention and surface morphology in dispersion-stengthened tungsten alloys under low and high flux D/He irradiations.* To be submitted, 2018.
3. E. Lang, A. Kapat, J.P. Allain. *Deciphering surface behavior and deuterium retention in tin-lithium-coated fuzzy tungsten substrates.* Nuclear Materials and Energy 12, 2017, 1352-1357.

Posters:

1. E. Lang, A. Kapat, J.P. Allain. "Behavior of a SnLi liquid metal eutectic on D-irradiated, porous tungsten substrates." 58th Annual Meeting of the APS Division of Plasma Physics, San Jose, CA, USA, October 31-November 4, 2016.

2. E. Lang, A. Kapat, J.P. Allain. "Determining liquid metal behavior and deuterium retention in tin-lithium-coated fuzzy tungsten substrates." Fusion Materials Workshop, Knoxville TN, USA, July 27, 2016.

3. E. Lang, A. Kapat, J.P. Allain. "Deciphering deuterium retention in D-irradiated porous low-Z coated tungsten nanostructures." 22nd International Conference on Plasma Surface Interactions in Controlled Fusion Devices, Rome, Italy, May 30-June 3, 2016.

4. A. Kapat, E. Lang, J.P. Allain, "D retention and wetting studies on tungsten-liquid metal hybrid systems" 16th International Conference on Plasma-Facing Materials and Components for Fusion Applications 16th-19th May 2017 Neuss/Dusseldorf, Germa

5. A. Kapat, J.P. Allain. "Li-based chemical dynamics on porous W during D_2 irradiation under simulated fusion PMI conditions" 5th International Symposium on Liquid metal Applications for fusion, Moscow, Russia, September 25-27, 2017.

6. E. Lang, N. Madden, C. Smith, J. Krogstad, J.P. Allain. "Development and characterization of dispersion strengthed tungsten alloys via spark plasma sintering." 59th Annual Meeting of the APS Division of Plasma Physics, Milwaukee, WI, USA, October 23-27, 2017.

7. A. Kapat, J.P. Allain. "Thermomechanical and chemical properties of porous W/liquid Li hybrid systems as plasma-facing self-healing surfaces" 59th Annual Meeting of the APS Division of Plasma Physics, Milwaukee, WI, USA, October 23-27, 2017.

8. E. Lang, N. Madden, C. Smith, J. Krogstad, J.P. Allain. "Development and characterization of dispersion strengthened tungsten alloys via spark plasma sintering." 19th International Conference on Fusion Reactor Materials, Aomori, Japan, November 5-10, 2017.

External Facilities and Collaborators:

At the national and international level, the program has established several **major-scale and extensive collaborations** with Oak Ridge National Laboratory (ORNL), Los Alamos National Laboratory (LANL) and the Dutch Institute for Fusion Energy Research (DIFFER) in Eindhoven, Netherlands. Collaboration with ORNL's Yutai Katoh's group is focused on: thermo-mechanical testing of candidate DSW and ITER-grade W materials as well as high-intensity plasma and radiation exposures. Collaboration with LANL's Stu Malloy's group focuses on: advanced nanocomposite and nanocrystalline W studies, in-situ TEM studies, advanced metallic glass and high-entropy alloy studies and ion beam analysis. Collaborations at DIFFER primarily consist of testing with combined quiescent and transient high-heat flux plasma conditions in Magnum-PSI, although plans to expand these tests in the Proto-MPEX facility at ORNL is under works (we are currently collaborating with Juergen Rapp's Proto-MPEX team to design a target test end station with in-situ PMI capability). These collaborations include multiple visits to collaborator centers by the PI and students as well as visits by collaborators to UIUC.

In addition to the major collaboration above, minor-scale collaborations have been started or planned to be expanded in the near future. These include: 1) work with Stephen Donnelly at the University of Huddersfield in the UK with the in-situ TEM ion-beam analysis MIAMI-2 facility to be inaugurated in Spring 2018, 2) work with Elodie Bernard and Emmanuelle Tsitrone at the new WEST fusion tokamak facility in Cadarache, France focused on W-based materials PMI testing under ultra long-pulse tokamak plasmas, 3) work with Dennis Whyte, Brian La Bombard and their team at MIT using the DIONISOS facility to study fuel retention with in-situ ion beam analysis under high-fluence plasma exposures, 4) work with Sybrand van der Zwaag (TU Delft) and Eduardo Saiz (Imperial College) on advanced Fe-Au alloys and refractory systems, respectively and 5) computational PMI materials science work with Brian Wirth (U. Tennessee) and Davide Curreli (UIUC) on coupling

our atomistic multi-scale surface response simulation modeling to their DOE SciDAC PMI modeling activities.

DIFFER (Dutch Institute for Fusion Energy Research) (access: 1-2 wk/yr): Magnum-PSI is a high-flux irradiation facility in the Netherlands that allows for low energy, high temperature, high fluence studies of D/He irradiations of surfaces utilized to study the material response under extreme, reactor-relevant conditions. Recent upgrades allow for the exposure of materials to simultaneous quiescent and transient pulsed plasmas and high heat fluxes to simulated off-normal events in fusion reactors.

TAMU (Texas A&M University) (access: 1-2 wk/yr): In collaboration with Dr. Lin Shao at Texas A&M University and the Ion Beam Lab, we expose W samples to high energy (3.5 MeV) W ions to mimic neutron damage. Pure W and DS-W samples are exposed to heavy ion pre-irradiation and subsequently exposed in IGNIS and Magnum-PSI to investigate the synergy between bulk damage and surface effects on PMI properties such as fuel retention and migration, surface morphology, and material erosion.

DIONISOS (MIT): Operated by the Plasma Science and Fusion Center at the Massachusetts Institute of Technology, The Dynamics of ION Implantation and Sputtering Of Surfaces (DIONISOS) allows for the investigation of surface with *in-situ* ion beam analysis during exposure to low temperature, high density edge/divertor plasmas. Equipped with a 1.7MeV tandem ion accelerator, the DIONISOS facility is capable of quantifying the evolution of relevant PMI processes, such as hydrogen isotope inventory and erosion/re-deposition through IBA (ion-beam analysis) techniques such as Nuclear Reaction Analysis (NRA), and Elastic Recoil Detection (ERD). The RF helicon plasma source is capable of fluxes on the order of 10^{22} $m^{-2}s$ and electron temperatures on the order of 4-8eV.

University of Huddersfield: MIAMI Facility (1 wk/yr): The MIAMI facility at the University of Huddersfield is an in-situ ion irradiation TEM facility that allows for concurrent irradiation and material characterization in an in-situ TEM device. We will utilize this platform to study the irradiation-induced defect dynamics of W-based materials in-situ, in real-time to understand the sub-surface dynamics that drive the surface response and properties.

Below are additional collaborations that leverages the resources and capabilities of each enabling critical testing, characterization and synthesis of various materials systems studied in this program with the unique focus that these systems are tailored for the PMI. These collaborators are not funded directly from this program but rather leverage other support including non-DOE-FES support. The expertise and interaction with these collaborators also provide significant training and professional development for young scientists at Illinois building a talent bridge to these major laboratories. One key example was Anton Neff who was funded from this program and obtained a DOE postdoctoral fellowship and now works at ORNL.

ORNL (year-round): Oak Ridge National Lab is an important collaborator for mechanical testing of DS-W materials, offering a wide platform of bulk mechanical testing and characterization facilities. We have an active collaboration with Dr. Lauren Garrison, allowing us to utilize the vast functionality ORNL offers. Some of the capabilities utilized at ORNL include: furnaces for recrystallization studies, mechanical test stages for tensile testing, platform for thermal

conductivity testing, and advanced microstructural characterization techniques. Furthermore, the Proto-MPEX facility being developed and its associated target test station offers a unique facility to test material behavior under transient and quiescent plasma conditions. This collaboration includes links with Dr. Juergen Rapp and Zeke Unterberg who now has Anton Neff as a DOE postdoctoral fellow working for him.

LANL (year-round): Los Alamos National Lab is becoming a critical partner in the design of advanced PFCs for extreme conditions expected in future fusion reactors. Under the leadership of Dr. David Teter, the Materials Science and Technology (MST) Division has partnered with Prof. Allain's group at UIUC to develop advanced PMI materials including: W alloys, high-entropy alloys and nanostructured refractory systems. Collaboration include work with Stu Malloy and Osman El-Atwani (a LANL postdoctoral fellow and former PhD student of Prof. Allain at Purdue).

WEST-EFDA (1-2 wk/yr): Elodie Bernard and Emmanuelle Tsitrone at the new WEST fusion tokamak facility in Cadarache, France focused on W-based materials PMI testing under ultra long-pulse tokamak plasmas.

INL (1-2 wk/yr): In collaboration with Dr. Chase Taylor (former PhD student of Prof. Allain at Purdue) at INL, the fuel retention and permeation characteristics of W-based materials will be examined. Their expertise in deuterium and tritium handling and variety of analytical tools allows for the retained fuel inventory in samples to be studied. The Tritium Plasma Experiment (TPE) allows for an understanding of the depth profile of T permeation throughout materials, and a variety of analytical tools, including GD-OES and TDS, will be utilized to study the D retention and permeation in these novel W-based materials.

SNL (1 wk/yr): Sandia National Lab is an important collaborator for in-situ mechanical testing of W-based materials. In collaboration with Dr. Stuart Malloy and Dr. Osman El-Atwani, micro-mechanical testing of W-based materials in-situ in an SEM will allow us to understand the mechanical properties W alloys. Using these techniques, we can understand how ion-induced surface damage alters the micro-mechanical behavior of tungsten alloys and correlate those properties with grain size, orientation, and composition. Additionally, their expertise in the fabrication of nanocrystalline materials and high-entropy alloys offers the opportunity to study unique materials at UIUC.

MIT (several weeks/yr): In collaboration with the Plasma Science and Fusion Center at the Massachusetts Institute of Technology, the dynamics of hydrogen isotope inventory in the hybrid liquid metal/porous W systems is being examined with the DIONISOS device, with Dr. Kevin Woller and Dr. Felipe Bedoya**.**

TU Delft: Collaboration with Sybrand van der Zwaag and his students on self-healing Fe-Au metallic alloys included a 2-week visit by PhD student that worked with Anton Neff on in-situ TEM characterization.

Imperial College: Collaboration with Prof. Eduardo Saiz will examine smart ceramic coatings in FY18.

Section 2: FY18-FY19 Program Activities

Summary

Tungsten is the material of choice for plasma-facing components in future plasma- burning fusion reactors because of its high melting point, high sputter threshold, and low hydrogenic species retention. However, tungsten is an intrinsically brittle material, displaying no room temperature ductility and only exhibiting non-brittle failure at temperatures at high temperatures. In addition to its limited ductility, tungsten's high melting point and low recrystallization temperature pose complications during fabrication and limit its temperature operating window in a future fusion reactor. Traditional synthesis routes tend to result in non-fully dense samples with coarse-grained microstructures. As a consequence, there is a desire for a fine-grained, fully-dense tungsten material that exhibits enhanced ductility.

Tungsten is embrittled by impurity oxygen atoms residing at grain boundaries. It is theorized that by microalloying tungsten with transition metal carbides that capture the oxygen atoms, the impurity distribution can be altered to beneficially impact the mechanical properties. Additionally, altering the interface concentration and type can increase the irradiation tolerance of tungsten. Through the advent of advanced powder processing techniques such as spark plasma sintering, dense, fine-grained tungsten samples can be developed with these microalloyed microstructures. Spark plasma sintering is a powder compaction technique that provides high pressure and heating rates, allowing for a lower final temperature and hold time for compaction.

In the work for FY18-FY19, spark plasma sintering is employed to develop tungsten materials alloyed with tantalum carbide, titanium carbide, or zirconium carbide, subsequently referred to as dispersion-strengthened tungsten. Samples are fabricated with varying compositions of added carbides (from 0.5-10 wt.%), and the sintering process results in >90% dense samples with grains <10 μm in size. Control of the microstructure and impurity distribution within the matrix is evident through the second phase addition, showing this technique can be used for advanced tungsten synthesis. The behavior of these dispersion-strengthened tungsten materials under reactor-like thermal and irradiation conditions is investigated to understand the plasma-material interaction properties and near-surface mechanical response of these materials to fusion-relevant irradiation conditions.

Under high temperature exposure, the enhanced recrystallization inhibition of dispersion-strengthened tungsten materials is shown up to 1800ºC and the long-term annealing properties exhibit increased incubation time for recovery, as a high number of tungsten-dispersoid interfaces is presented to pin grain boundaries and enhance mechanical properties. However, deuterium irradiation results in surface blistering, while the dispersoid composition and distribution in the bulk samples has been shown to increase deuterium transport and retention. Multiscale helium irradiations show no enhanced surface sputtering compared to pure tungsten nor preferential sputtering, indicating surface compositional stability for stable properties under irradiation. Diminished surface nanostructuring under helium irradiation due to altered helium trapping and decreased bubble formation within the microstructure is demonstrated. The altered helium bubble dynamics is attributed to the dispersoid composition and the W-dispersoid interface chemistry, which help mitigate the detrimental effects of helium on the tungsten microstructure.

This work shows the promise of dispersion-strengthened tungsten materials to prevent the detrimental effects of helium irradiation of pure tungsten, while also preventing recrystallization of tungsten under high temperature exposure. Compared to pure tungsten in a fusion environment, these results indicate a wider temperature operating window and show greater helium irradiation resistance, demonstrating enhanced thermo-mechanical and irradiation properties that can benefit future fusion reactor plasma-facing materials development.

Products

Peer-reviewed papers (links can take reader to the manuscript DOI)
These papers contain "Section 2" work representing Chapters 3-5 of Lang PhD thesis not included here due to size restrictions with Final Report.

- Lang, E., Kapat, A., Morgan, TW., **Allain, J.P.** (2020) "High Flux Helium Irradiation of Dispersion-Strengthened Tungsten Alloys and Effects of Heavy Metal Impurity Layer Deposition" Journal of Nuclear Materials, online November 13, 2020.

- Lang, E., Schamis, H, Madden, N., Smith,C., Kolasinski, R., Krogstad, J., **Allain, J.P.** (2020) "Recrystallization Suppression Through Dispersion-Strengthening of Tungsten", Journal of Nuclear Materials, 152613, online November 4, 2020.

- Lang, E., Taylor, CN., **Allain, J.P.** (2020) "GD-OES study of the influence of second phase particles on the deuterium depth distribution in dispersion-strengthened tungsten", Journal of Nuclear Materials, 2020.

- Lang, E., Madden, N., Smith, C., Krogstad, J., **Allain**, **J**.**P**. (2019) "Deciphering the role of second phase precipitates on early-stage surface morphology development of dispersion-strengthened W alloys under low energy He irradiation", Nuclear Materials and Energy, Vol. 19, May 2019, Pages 47-54.

- Lang, E., Reid, N., Garrison, L., Parish, C., **Allain, J.P.** (2019) "Pre-Irradiation Comparison of W-Based Alloys for the PHENIX Campaign: Microstructure, Composition, and Mechanical Properties", Fusion Science and Technology, May 2019.

- Lang, E; Madden, N; Smith, C; Krogstad, J; **Allain, J.P.** (2018) "Microstructural and compositional effects of transition metal carbide additions on dispersion-strengthened tungsten fabricated via spark plasma sintering", International Journal of Refractory Metals and Hard Materials, Vol 75, p.p. 279-286, September 2018.

TABLE OF CONTENTS

CHAPTER 1: BACKGROUND AND INTRODUCTION..... 1
CHAPTER 2: EXPERIMENTAL AND ANALYSIS FACILITIES.....45
CHAPTER 6: CONCLUSIONS.....226
CHAPTER 7: FUTURE WORK.....240
APPENDIX A: SPUTTERING YIELD CALCULATIONS.....255
APPENDIX B: ESHELBY CALCULATION.....261

CHAPTER 1: BACKGROUND AND INTRODUCTION

Nuclear fusion

As the world's energy demands continue to grow, we must confront the energy crisis and meet our energy demands with alternative energy sources that limit carbon emissions [1, 2]. An ideal energy source is competitive and predictable, offers economic and environmental incentives for production, has a low risk of accident (i.e. considered "safe"), and has an abundant fuel supply [3]. Confined nuclear fusion as an energy source has the potential to meet these needs.

Nuclear fusion offers the prospect of MWs of energy (ITER will generate ~1500 MW_{th}) [4] while minimizing the radioactive waste that plagues fission reactors. Nuclear fusion reactor concepts take many designs, but the most successful fusion device configuration to date has been magnetic confinement fusion. Magnetic confinement fusion devices such as tokamaks generate very hot plasmas capable of fusing together atomic nuclei such as deuterium and tritium (D-T), and release energy. In a standard DT reaction, fusing deuterium and tritium, a 3.5 MeV alpha particle is generated along with a 14.1 MeV neutron [2]. A tokamak, pictured in Figure 1.1 uses toroidal, poloidal, and vertical magnetic fields to confine particles and causing charged particles to move in helical orbits, as shown in Figure 1.2.

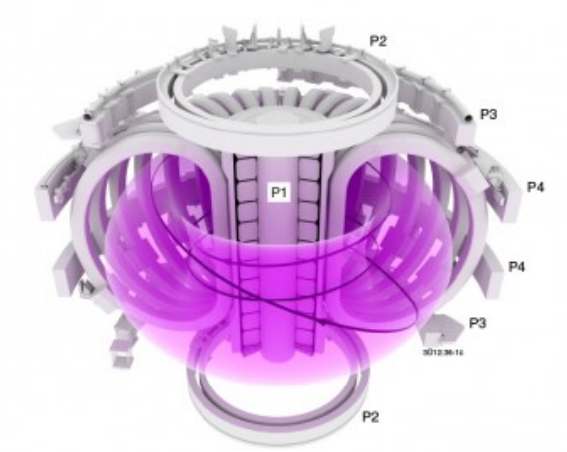

Figure 1.1: Schematic of a toroidal tokamak device for magnetic confinement [5].

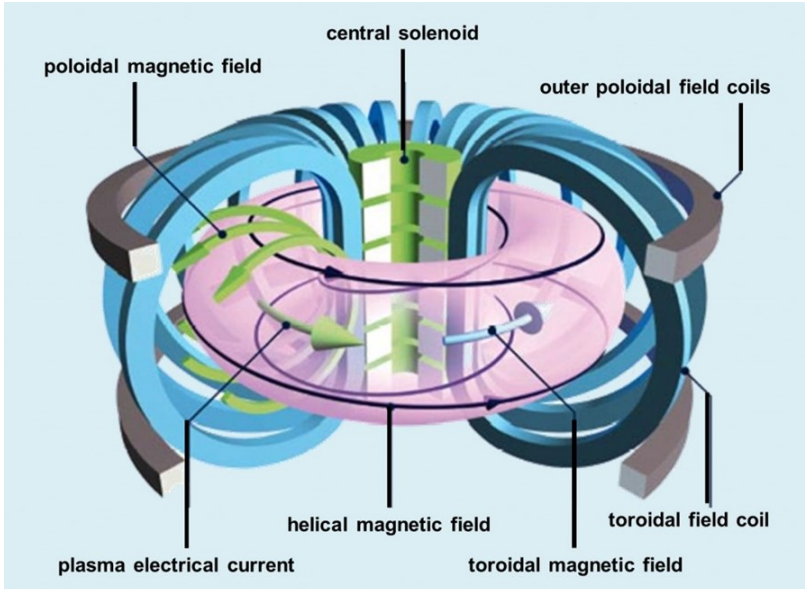

Figure 1.2: Schematic of a tokamak showing magnetic field coils and lines and charged particle trajectories in a tokamak [6].

In a tokamak, charged particles traverse the device in helical orbits, their motion restricted by the magnetic fields. Successful confinement and energy production in a magnetic fusion device depends on the Lawson Criterion, which dictates that the triple product of the ion density n, ion temperature T, and energy confinement time τ must reach a threshold value to sustain a reaction [7]. Over time, the product of $nT\tau$, has continually increased towards the point of energy breakeven, in which more energy is gained than is put in, as shown in Figure 1.3 [8].

To improve the triple product, better control over impurity migration from the wall to the core plasma is necessary. Impurities are introduced into the plasma via interactions with the walls such as sputtering, evaporation, and melting, and these impurities can cause disruptions that hinder the fusion reactions and can cause device failure [9]. Plasma material interactions (PMI) are linked to the ability to successfully generate a fusion device. Impurities can enter the core plasma and dissipate a large amount of energy through raising the effective atomic number, Z_{eff}, of the plasma and cool the plasma through Bremsstrahlung radiation, thus decreasing the Lawson Criterion [2, 10]. Controlling impurities and fuel recycling is crucial to understanding PMI and advancing fusion energy. Throughout the years, different materials for plasma-facing applications have been employed. Carbon, beryllium, and tungsten will be used as the plasma-facing materials in ITER, while stainless steels and molybdenum have been used in prior reactors. Low-Z materials, such as carbon and lithium, have been used in the past for their high tolerable impurity concentration. High-Z materials, like tungsten and molybdenum, have less erosion and higher melting points, but the fraction of tolerable impurities in the plasma is much lower [11, 12].

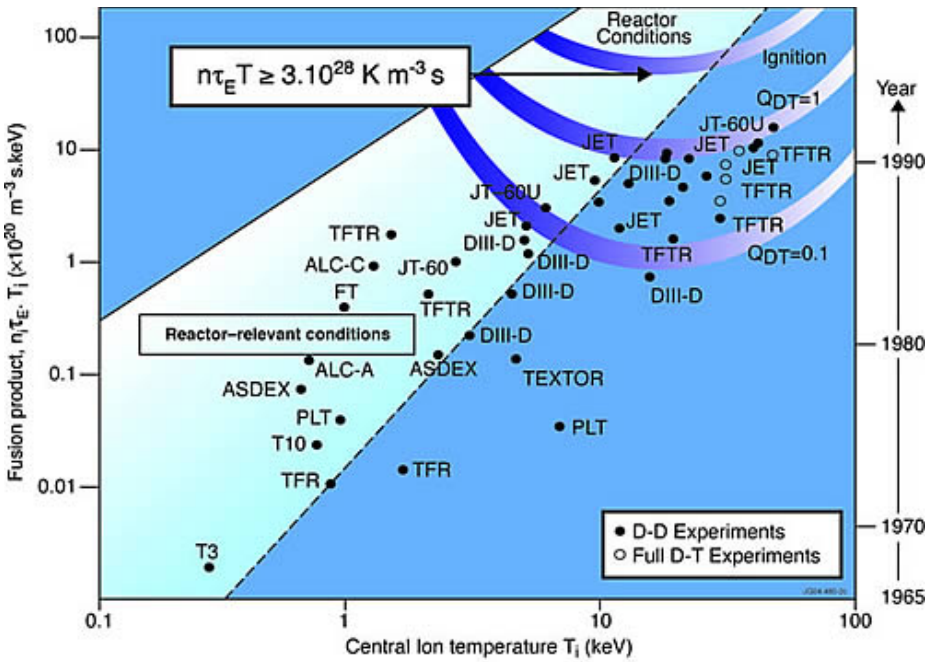

Figure 1.3: Lawson Criterion of fusion progress in various tokamak devices showing progress towards breakeven, ignition, and reactor conditions [8].

Materials for fusion

The choice of plasma-facing material in a fusion reactor can greatly impact the performance of the plasma. The main region for plasma-material interactions in a tokamak is the divertor region as shown in Figure 1.4. In ITER, the divertor will be made of tungsten and the first wall will be beryllium [12].

The divertor in a tokamak is the region in which particles lost to the scrape-off layer are directed. As ions and electrons escape from the core, they diffuse to the plasma edge, where magnetic field lines direct these particles along the scrape-off-layer, the outer edge of the core plasma just at the separatrix in Figure 1.4, to a sacrificial region at the bottom of the tokamak, the divertor. Large heat and particle loads can be focused on the divertor strike points (referred to as "Target plate" in Figure 1.4) which can cause erosion of the divertor material. The divertor region can experience peak heat fluxes of 10-20 MWm^{-2}, particle energies of 1-30 eV, particle fluxes of 10^{24} m^{2}s^{-1}, and temperatures above 1000 C [9, 13].

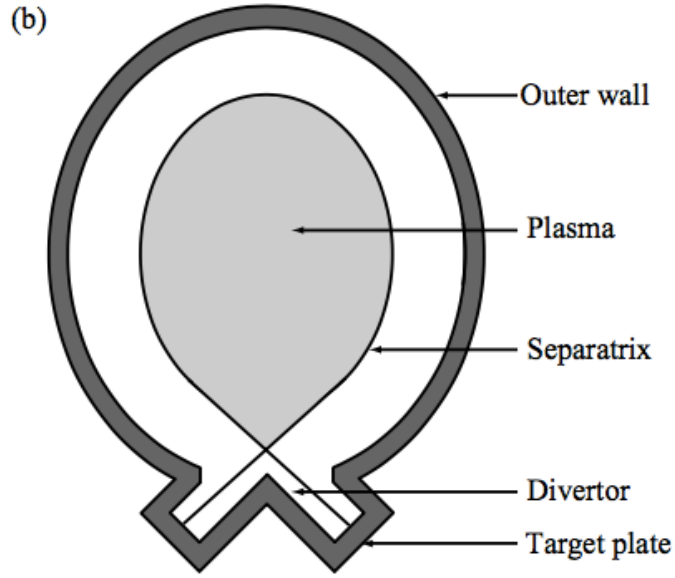

Figure 1.4: Cross-sectional diagram of a tokamak showing the plasma, separatrix, and white region showing scrape-off layer directing particles to the inner and outer strike points of the divertor, denoted as the "Target plate" [2].

Materials in the divertor region need to be resistant to damage by energetic particles (14 MeV neutrons, and low energy D and T ions), operate at high temperatures, and maintain good thermomechanical properties [13]. The divertor also needs to minimize impurity injection into the plasma, which can cool the plasma through radiation losses [9]. The divertor can be eroded by sputtering (both self-sputtering and impurity-induced sputtering) and local melting (through unipolar arcs). Eroded material can migrate and form a redeposited layer, whose composition can differ from the nominal wall material [14]. The divertor minimizes the overall plasma-surface interaction to a small area away from the core of the plasma.

Graphite was first used as a PFC in fusion reactors because it has a low atomic number and does not melt. However, carbon has a high chemical sputtering yield and has elevated D and T retention levels, which introduces a safety and fueling hazard, limiting its effectiveness. The issues regarding sputtering and fuel retention led to the exploration of high-Z materials for use as PFCs.

Tungsten is to be used as the divertor PFC in ITER as it has favorable thermomechanical properties, a very high melting point, and a high sputtering threshold. However, a high-Z material has a much lower tolerable impurity concentration in the plasma, so erosion must be minimized [11, 15]. This fraction of tolerable impurities is shown in Figure 1.5. Tungsten has a higher sputtering threshold than carbon and has a higher melting point.

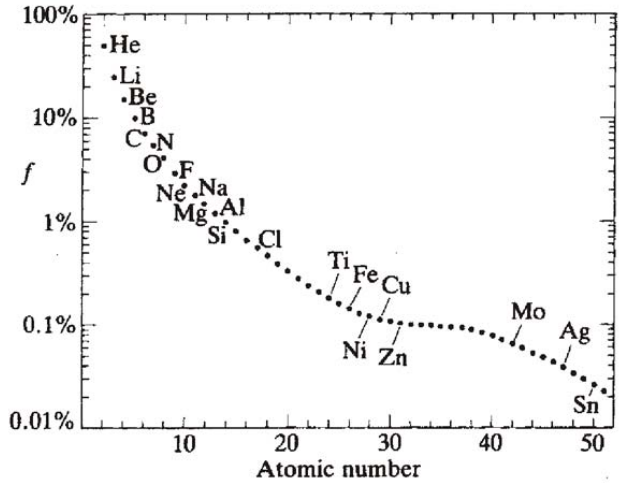

Figure 1.5: Tolerable fraction of impurities *f* as a function of atomic number *Z* showing how little high-Z contamination from plasma-facing materials can be tolerated [11].

Conditions in a fusion reactor environment

Materials employed in a fusion reactor will be exposed to a harsh heat and particle irradiation environment, including low energy (<100 eV) D and He bombardment, high energy neutron irradiation (neutron energy spectrum peaking at 14 MeV accumulating up to 30 dpa/year), steady-state thermal loads of 0.1-1 MWm^{-2}, temperatures of 500-3200 C, and transient thermal loads in excess of 20 MW m^{-2}. High flux (~$1x10^{15}m^{-2}$) neutron bombardment will lead to significant He (~50 appm/dpa) and He (~15 appm/dpa) accumulation in the bulk. The multitude of environmental challenges that plasma-facing material will face in a fusion reactor are shown in Figure 1.6 below [16].

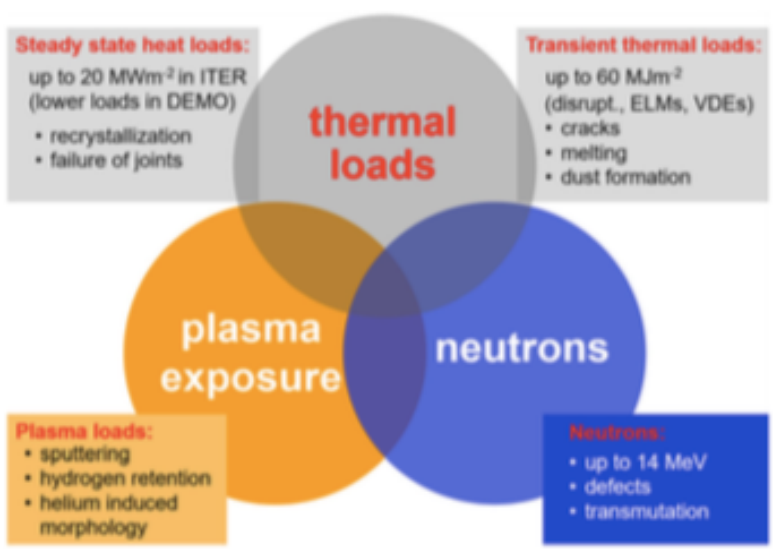

Figure 1.6: Schematic of the synergistic thermal, neutron, and plasma loads plasma-facing materials will face during D-T plasma operation [16].

Fusion neutron energy spectrum compared to fission neutron energy spectrum [17] with the differences in the spectra shown in Figure 1.7 [16]. Materials selected to be used in these environments must be able to tolerate the conditions and maintain their performance and properties. One major concern for plasma-facing materials is the interaction of high energy neutrons generated in the plasma. The neutron energy spectrum in a fusion reactor or fast fission reactor differs significantly from that of a fission reactor. These high energy neutrons will have different effects on the material microstructure and composition. The neutron bombardment will change the material properties, the details of which on tungsten will be elaborated in Chapter 1.3.

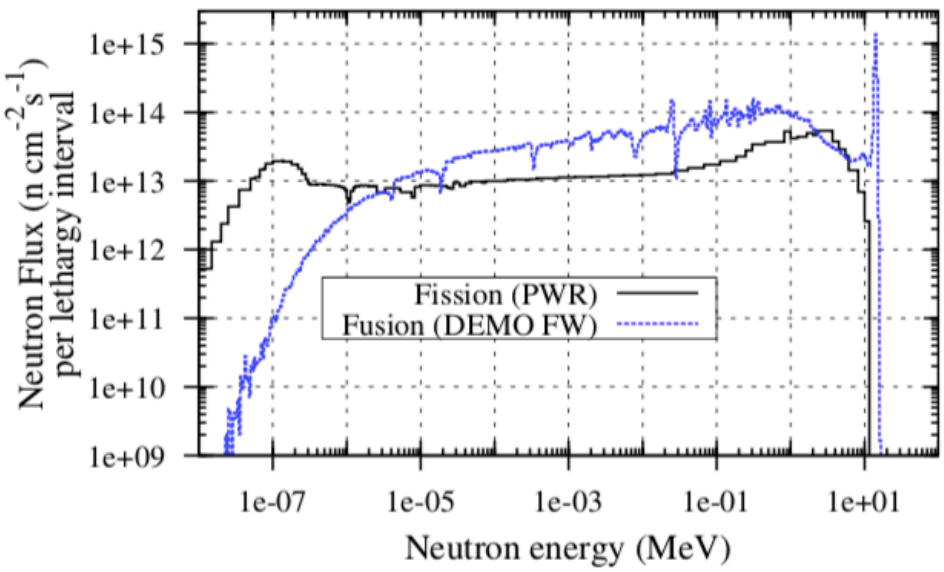

Figure 1.7: Fission and fusion neutron energy spectra, demonstrating the high energy peak of fusion neutrons [17].

Synergistic effects of charged particle and neutron irradiation, high temperatures and transient temperature excursions can induce numerous effects on plasma-facing materials, such as: cracking and melting, hydrogen-induced blistering, neutron-induced voids and precipitates, and helium-induced bubbles. All of these can degrade the plasma-facing materials and alter their properties. A summary of the impacts of the fusion environment on the plasma-facing material performance is shown in Figure 1.8.

Additionally, neutron-driven transmutation reactions can lead to the generation of H and He in the bulk. In a fusion reactor environment, it is predicted that the He/dpa ratio will be ~50-100 times greater than in a fission reactor [18]. Thus, the material challenges that will be faced in a fusion reactor environment cannot be accurately simulated via other methods. This is shown in Figure 1.9 from S. Zinkle, et al. demonstrating that the damage and He production environments that materials will encounter in future nuclear reactors are unprecedented compared to current fission reactors [18].

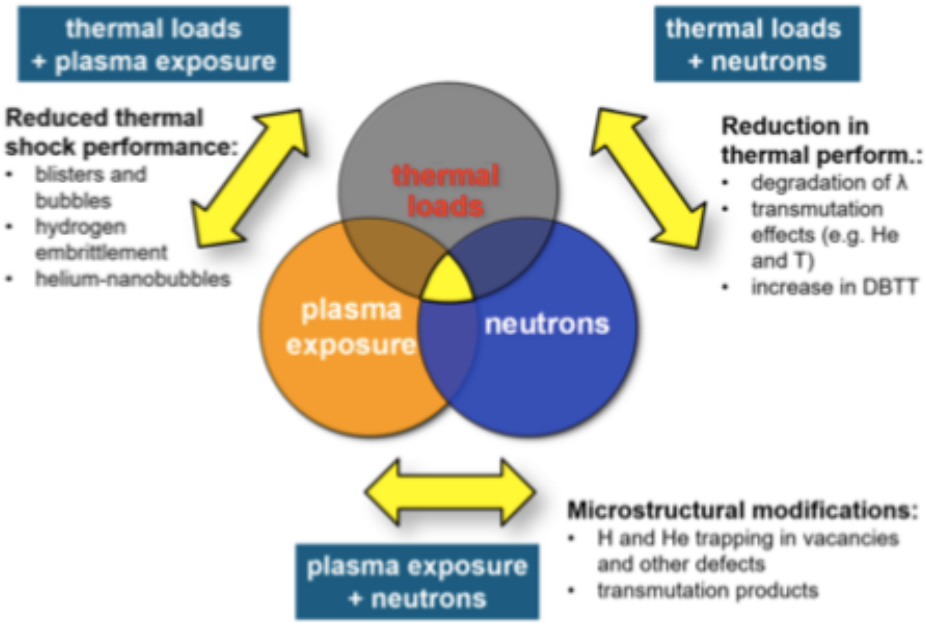

Figure 1.8: Summary of the particle and heat loads on plasma-facing materials and resulting impacts on material properties and performance [16].

The combination of temperature and dpa damage that structural materials in fusion reactors and advanced fission reactors must tolerate show that there is little experience and knowledge on how materials will behave in these environments. However, materials must be designed with these operating conditions in mind.

Fundamentals of Ion Bombardment, Damage Cascades, and Defect Dynamics

When materials undergo particle (ion or neutron in a tokamak) bombardment, a displacement cascade is generated within the matrix creating vacancies and interstitials, as the incident ion and subsequently impacted matrix atoms can remove lattice atoms from their sites. An interstitial is a matrix atom that is displaced from its original lattice site and resides not in a lattice site while a vacancy is a lattice site that is missing an atom. During a cascade, vacancies and interstitials recombine to self-annihilate and no end damage is created. Most vacancies and interstitials that are initially formed eventually recombine, however the residual ones that do not recombine contribute to radiation damage [19-21].

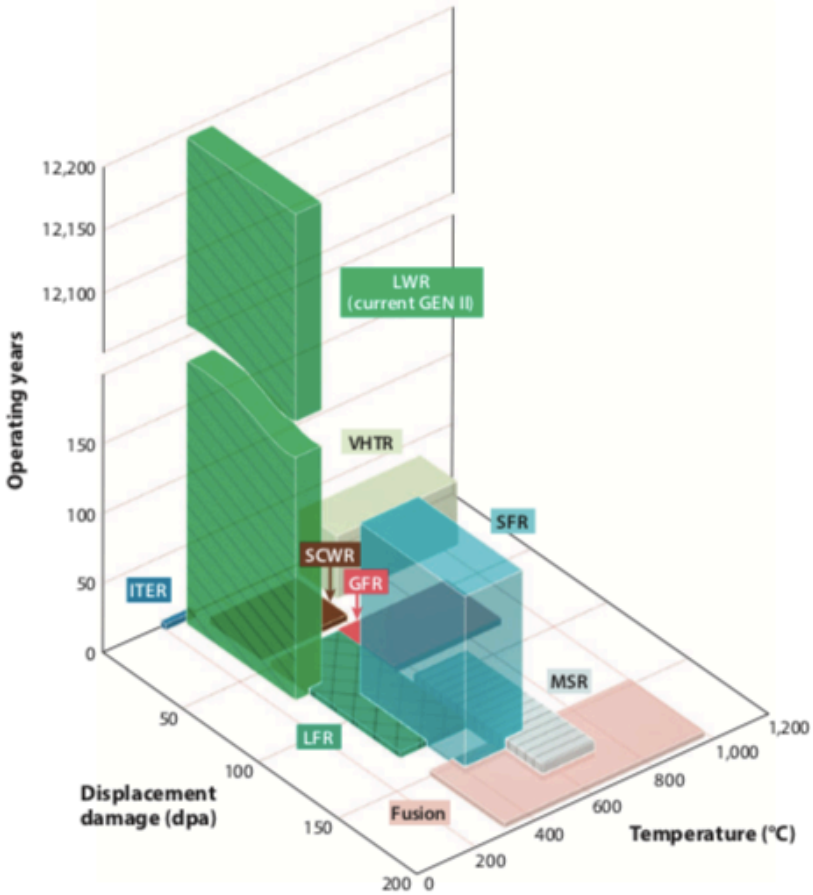

Figure 1.9: Plot of operating temperature, cumulative operation displacement damage, and operating lifetime for materials in current and future fission and fusion nuclear reactors [18].

The radiation damage can take the form of defect clusters, including dislocation loops and voids as the irradiation-induced damage accumulates [19, 20]. During the cascade, grain boundaries preferentially absorb interstitials, and leave a vacancy-rich grain. Vacancies that are near a grain boundary can be annihilated via interstitial emission, where an interstitial is released to recombine with the vacancy. Thus, grain boundaries are sinks for point defects. Complete healing of radiation damage occurs when interstitials and vacancies recombine. Introducing a high density of sinks for point defect recombination can enhance the irradiation tolerance, with grain boundaries, precipitates, dislocations, and second phase particles having different sink strengths [22-24]. To be able to function in a nuclear radiation environment without large degradation of the properties, a material must tolerate the radiation damage and prevent point defect damage accumulation. The figure below shows the damage cascade near a grain boundary, showing how interstitials and vacancies interact at low temperatures (left boxes), medium temperatures (center boxes), and high temperature (right boxes) showing recombination and annihilation near grain boundaries to tolerate radiation damage [22]. Therefore, introducing a high number of sinks for recombination can increase the radiation tolerance of materials.

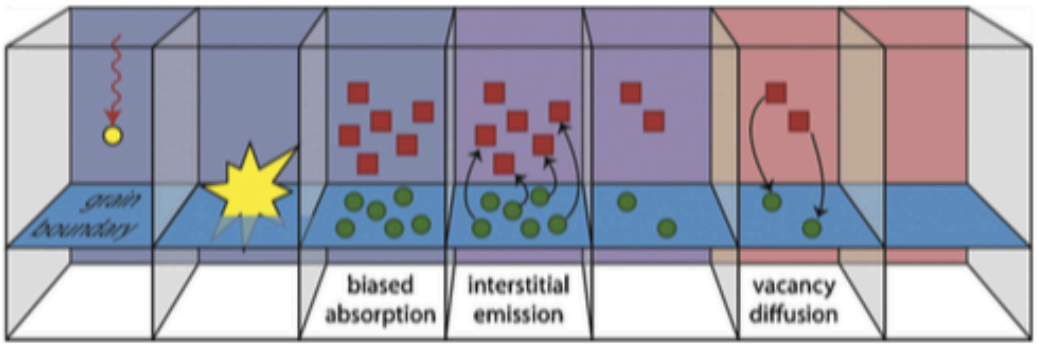

Figure 1.10: Schematic of radiation damage annihilation near grain boundaries showing how having a high density of recombination sites, such as grain boundaries, can enhance the radiation tolerance [22].

Nanocrystalline Metals

One potential class of materials that may tolerate such harsh environments is nanocrystalline metals. The high damage dose that materials in future reactors will incur will introduce significant point defect damage that must be mitigated to avoid detrimental changes to the material properties. Nanocrystalline materials have a high density of grain boundaries which can introduce sinks that will improve the radiation tolerance of the material. As shown pictorially in Figure 1.11, grain boundaries are effective defect sinks, absorbing and re-emitting self-interstitials to annihilate vacancies in a region surrounding the grain boundary [23]. If a high enough grain boundary density exists, then the annihilation region relative to the entire material will be large, and effective suppression of the radiation damage can occur. The strength of the grain boundaries as a defect sink is inversely proportional to the square of the grain size [25].

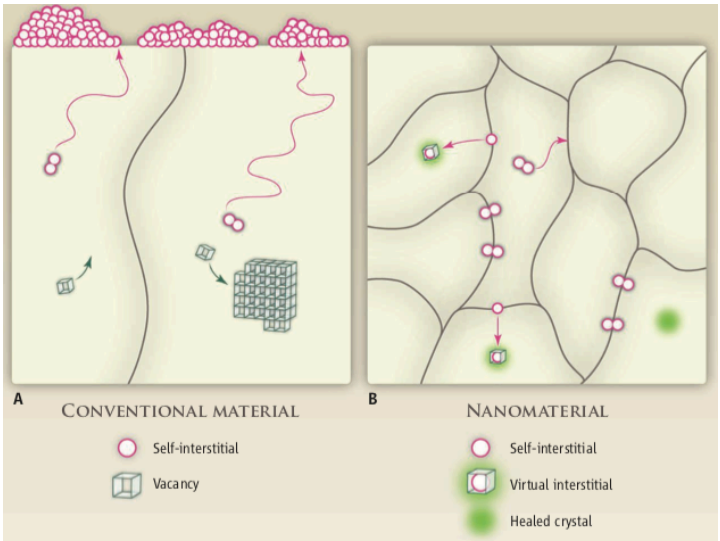

Figure 1.11: Schematic displaying self-healing ability of nanocrystalline materials due to the high density of grain boundaries to absorb interstitials and promote interstitial-vacancy recombination [23].

Nanocrystalline metals have been shown to have enhanced ability to suppress point defects compared to coarse-grained materials under a variety of irradiation conditions. M. Rose, et al. showed that nanocrystalline Pd had a reduction in defect clusters under 4 MeV Kr^+ bombardment if the Pd grain size was below 50 nm [26]. Similarly, N. Nita, et al. demonstrated lower defect densities in nanocrystalline Ni and Cu under Ni and p^+ bombardment [27]. Y. Chimi, et al. showed similar results in nanocrystalline Au under C^+ irradiation [28]. In a more fusion-relevant context, nanocrystalline Fe has been shown to lower the He bubble density compared to coarse-grained W, due to bubbles coalescing at grain boundaries. Nanocrystalline W has also been shown to enhance the fluence threshold of He-induced surface modification by increasing the grain boundary density in the bulk to serve as sinks for the He bubbles [29-32], shown in Figure 1.12. For W in a fusion reactor context, grain boundaries can absorb He-Vacancy complexes that results in reduced He bubble densities. However, large bubble sizes are reported on the grain boundaries [32].

Nanocrystalline metals also have mechanical properties that differ from their coarse-grained counterparts. Nanocrystalline W and Ta has exhibited higher hardness and strength and lower DBTT [33] compared to a coarse-grained reference [34-35].

However, nanocrystalline materials are not without their flaws. They are unstable, and can undergo grain growth at temperatures well below those of a coarse-grained material. Nanocrystalline W, Cu, and many other metals have demonstrated this behavior [36-39]. Therefore, the benefits provided by the nanocrystalline microstructure can be diminished if the refined grain size is not stable. Efforts must be taken to ensure that the microstructure is stable, commonly through the addition of solute particles or second phases [40].

Many recent studies have focused on the radiation performance of oxide dispersion-strengthened steels (ODS steel). These are steels strengthened with oxide particles, commonly yttria, to enhance the swelling and creep resistance. These materials have also shown to have enhanced radiation tolerance under a range of irradiation conditions. ODS particles have been shown to absorb defects without introducing swelling or hardening [41-44]. The matrix-nanoparticle boundaries have been observed to be preferential nucleation and trapping sites for He bubbles, which may reduce the free He bubble density that may cause detrimental effects on material performance [43]. Carbide precipitates in steels also trap He preferentially, and limit the He concentration in the matrix [42].

The motivation for the work presented in this document stems from the enhanced radiation tolerance of nanocrystalline W, the enhanced performance of dispersion-strengthened steels, and the desire to control the instability of nanocrystalline W at high temperatures to maintain its microstructure. Inhibition of grain growth is important for processing of nanocrystalline materials. Grain growth reduces the grain boundary energy of the material as atoms diffuse along grain boundaries to re-define grain structure and is enhanced at high temperatures. Dispersing a second phase particle in the primary material matrix can inhibit grain growth, and has been shown in many materials. This technique can also be employed in tungsten to stabilize the microstructure.

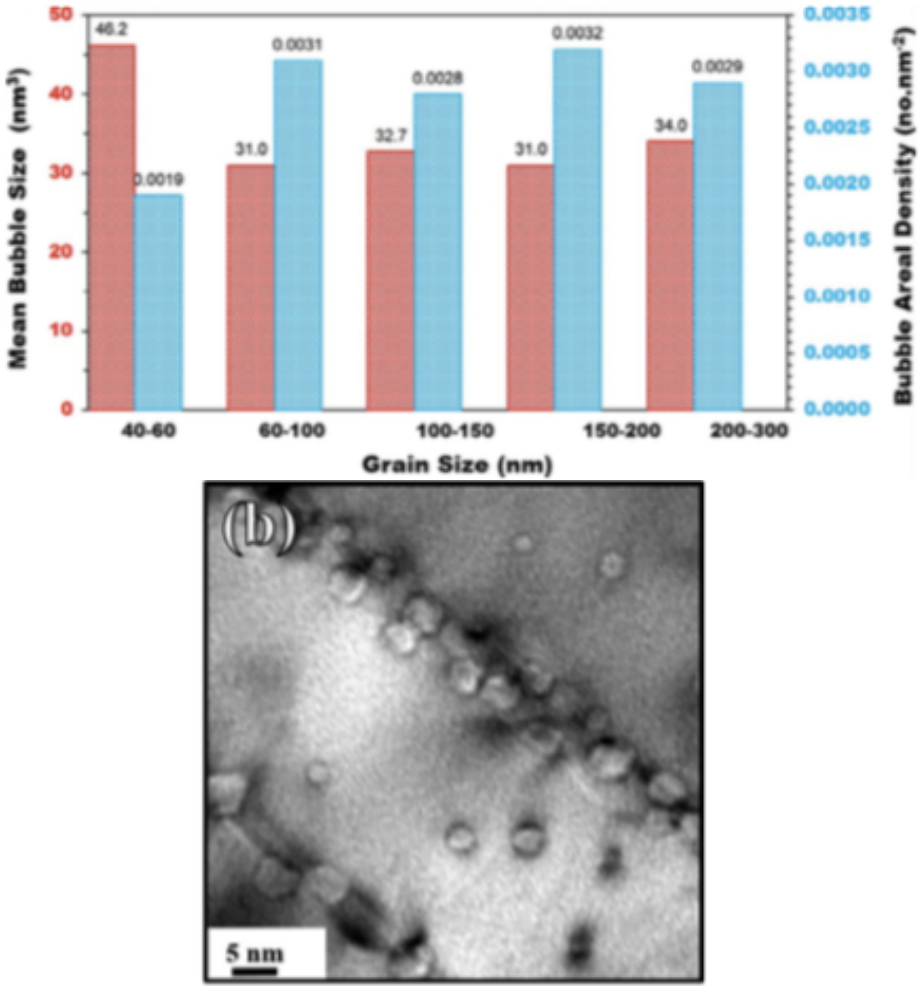

Figure 1.12: Average He bubble size and bubble density as a function of W grain size, showing that nanocrystalline W grains (<60nm in size) have larger, but fewer bubbles. (b) TEM micrograph of nanocrystalline W grains showing larger and more He bubbles at grain boundaries and fewer within grains [32].

Tungsten

Tungsten properties

Tungsten is a refractory metal with atomic number 74 and atomic mass of 183.8 amu. It has a body-centered-cubic crystal structure with the highest melting point of all elements, 3695 K. Due to its high melting point, tungsten is a material of interest in many extreme environments. The density of tungsten is among the highest of all metals, at ~19.3 g/cm^3 [45].

Overall, tungsten has a high strength and yield point, but has limited ductility and a high ductile-to-brittle transition temperature (DBTT) of ~300-400°C. Tungsten acts in a brittle manner at room temperature when subjected to tensile stresses. Tungsten has a high yield strength and good creep resistance; however, tungsten undergoes rapid oxidation at 300-400°C [45-47].

Tungsten is an intrinsically brittle material, as fracture of tungsten usually occurs in an intergranular nature. The grain boundaries represent the weakest links due to segregation of impurities (H, C, O, N, etc.) to the grain boundaries. Figure 1.13 below shows typical load-

displacement curves for tungsten under tensile stress from 150°C to 500°C. Under tensile stress, the typical failure mechanism of tungsten is intergranular failure [48]. As the test temperature is increased, tungsten can be shown to undergo transgranular failure, common in less-brittle materials, as shown in Figure 1.14.

In addition to its intrinsic brittle nature, tungsten also undergoes increased embrittlement due to recrystallization and irradiation. While the exact temperature for recrystallization depends on the fabrication history and microstructure of the material, and experimental parameters, common tungsten typically undergoes recrystallization around 1100-1300°C. Recrystallization embrittlement reduces the grain boundary strength as the concentration of impurities in the grain boundaries increases because the grain boundary density decreases. This increases the chance of intergranular fracture and raises the DBTT even more. However, if the microstructure can be controlled during high temperature exposure, such as through grain size reduction or addition of second phase particles, the recrystallization behavior and mechanical properties of tungsten can be improved and maintained. The schematic shown in Fig. 1.15 shows how the grain structure and mechanical properties change as the temperature increases. The grey region indicates the potential operating regime for future fission and fusion reactors.

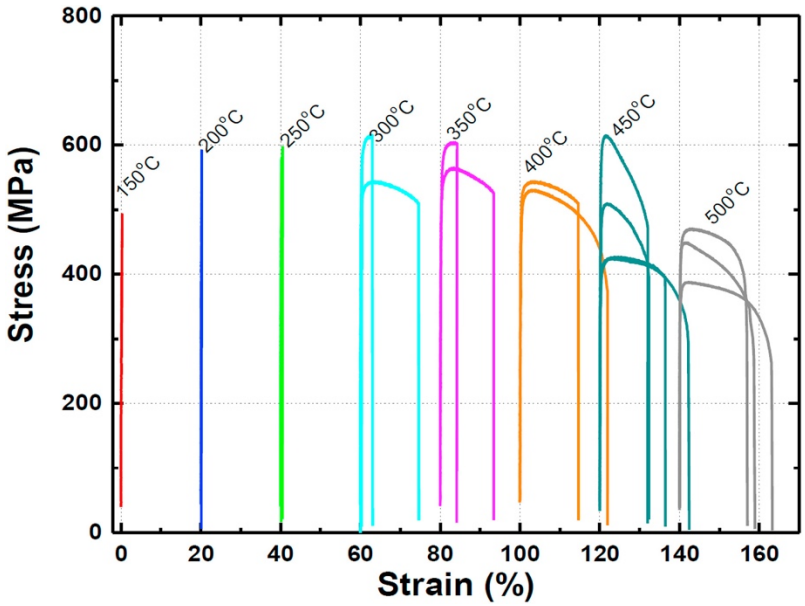

Figure 1.13: Typical load-displacement curves for tungsten tested at temperatures from 150-500 C showing the DBTT of W is above 300 C [47].

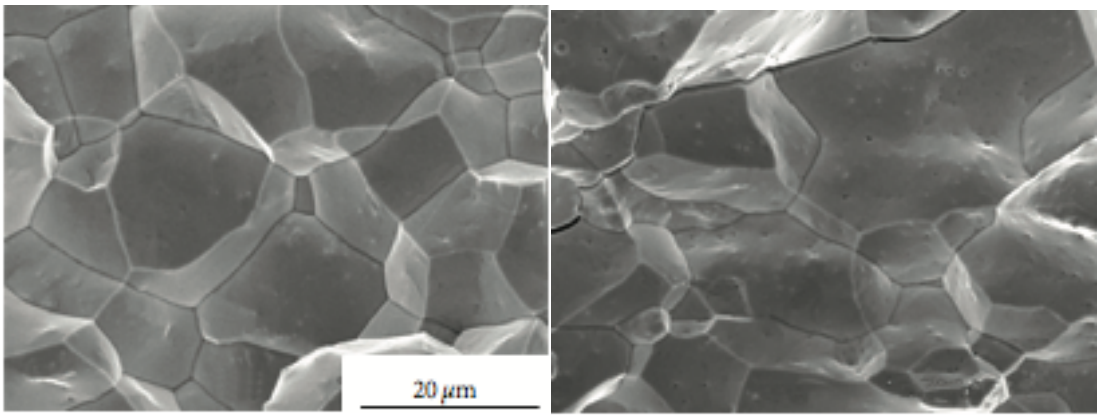

Figure. 1.14: Intergranular (left) and transgranular (right) fracture surfaces of tungsten [49].

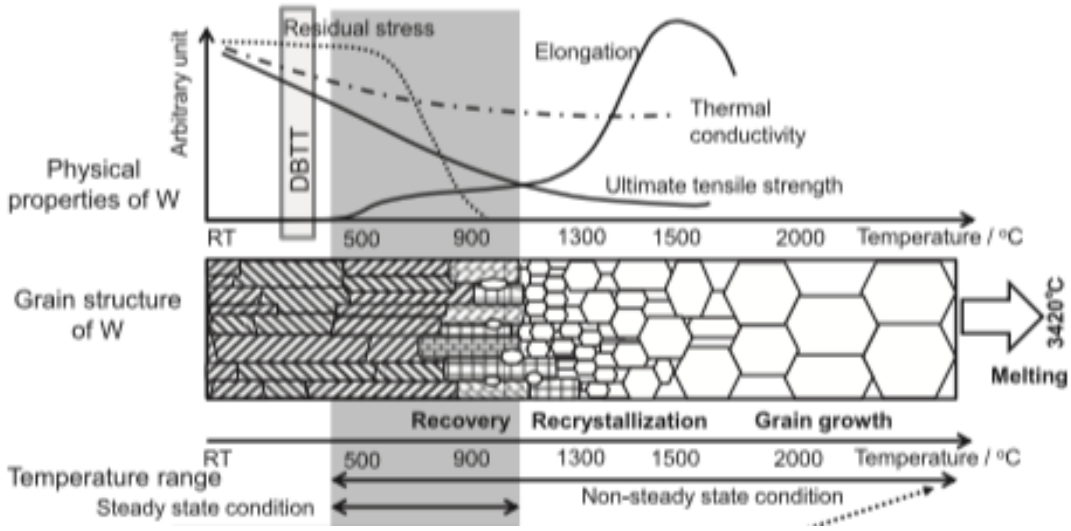

Figure 1.15: Microstructure and material property changes as a function of temperature overlaid on the fusion reactor temperature operating regime (grey) [51]. This shows that pure W has a narrow window of reliable operation in a fusion reactor and higher temperatures result in changing material properties and microstructure.

In pure tungsten, neutron damage causes knock-on damage leading to defects such as loop and void damage in the bulk material. The effects of neutron will depend intimately on the irradiation dose and temperature, but the Fig. 1.16 summarizes the effects of neutron damage on W.

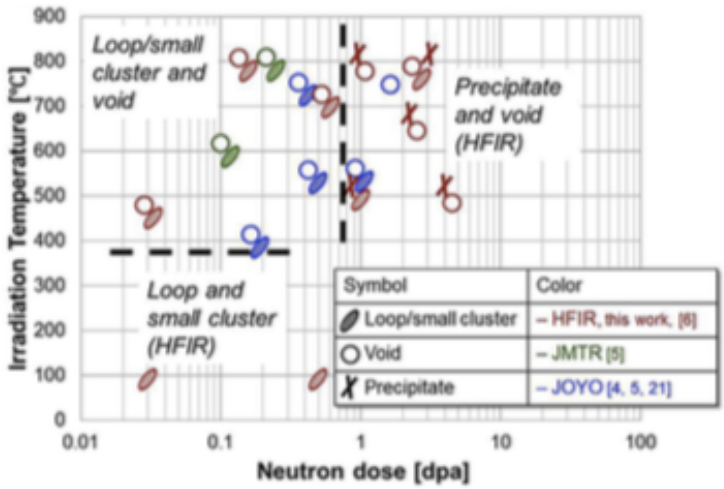

Figure 1.16: Microstructural changes in W under neutron irradiation as a function of neutron irradiation dose and temperature [52].

Additionally, transmutation reactions lead to the material elemental composition changing as W transmutes to Re and Os. After 5 years exposure in a fusion power plant, it is hypothesized that the composition of a W plasma-facing component will be 3.8 wt.% Re, 1.4 wt.% Os [53] as shown in Fig. 1.17.

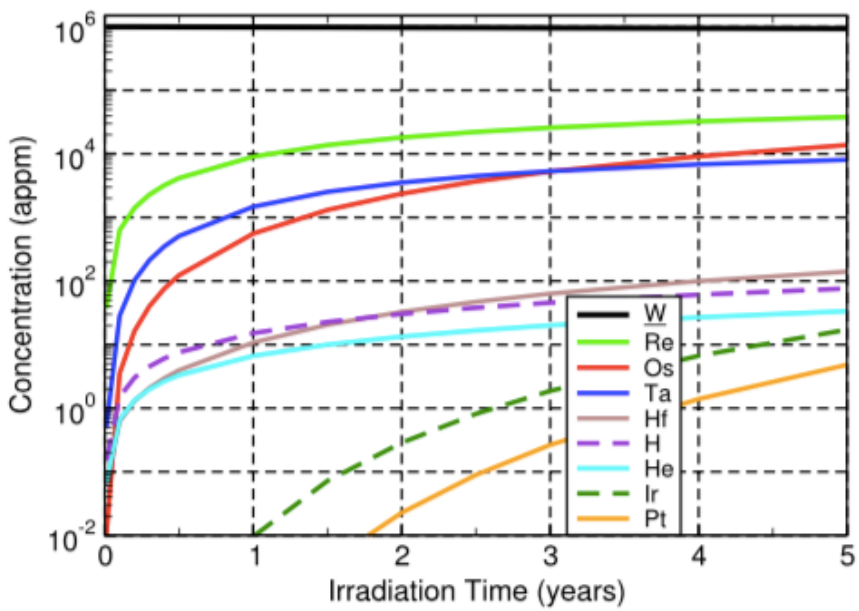

Figure 1.17: Compositional change of pure W as a function of neutron irradiation time showing transmutation to Re and Os [53].

The transmutation to Re and Os leads to the development of Re/Os-rich precipitates that will significantly alter the mechanical properties, that are shown in the STEM-EDS maps in Fig. 1.18. Significant Re and Os precipitation combined with loop and void damage cause hardening and loss of ductility in W, shown in Fig. 1.19 [52]. Additionally, the transmutation to Re and Os may alter the plasma-material interactions, such as D retention and He behavior and morphology [54-56] shown in Fig. 1.20.

The behavior of W alloys under neutron irradiation is not well known, but predictions of W-30%Ta and W-30%Ti alloys show that after 5 years of irradiation in a fusion power plant they may have altered H and He buildup,compared to pure W [53]. Additionally, neutron irradiation simulations of Zr have shown resistance to He-induced embrittlement, similar to W and Ta [53].

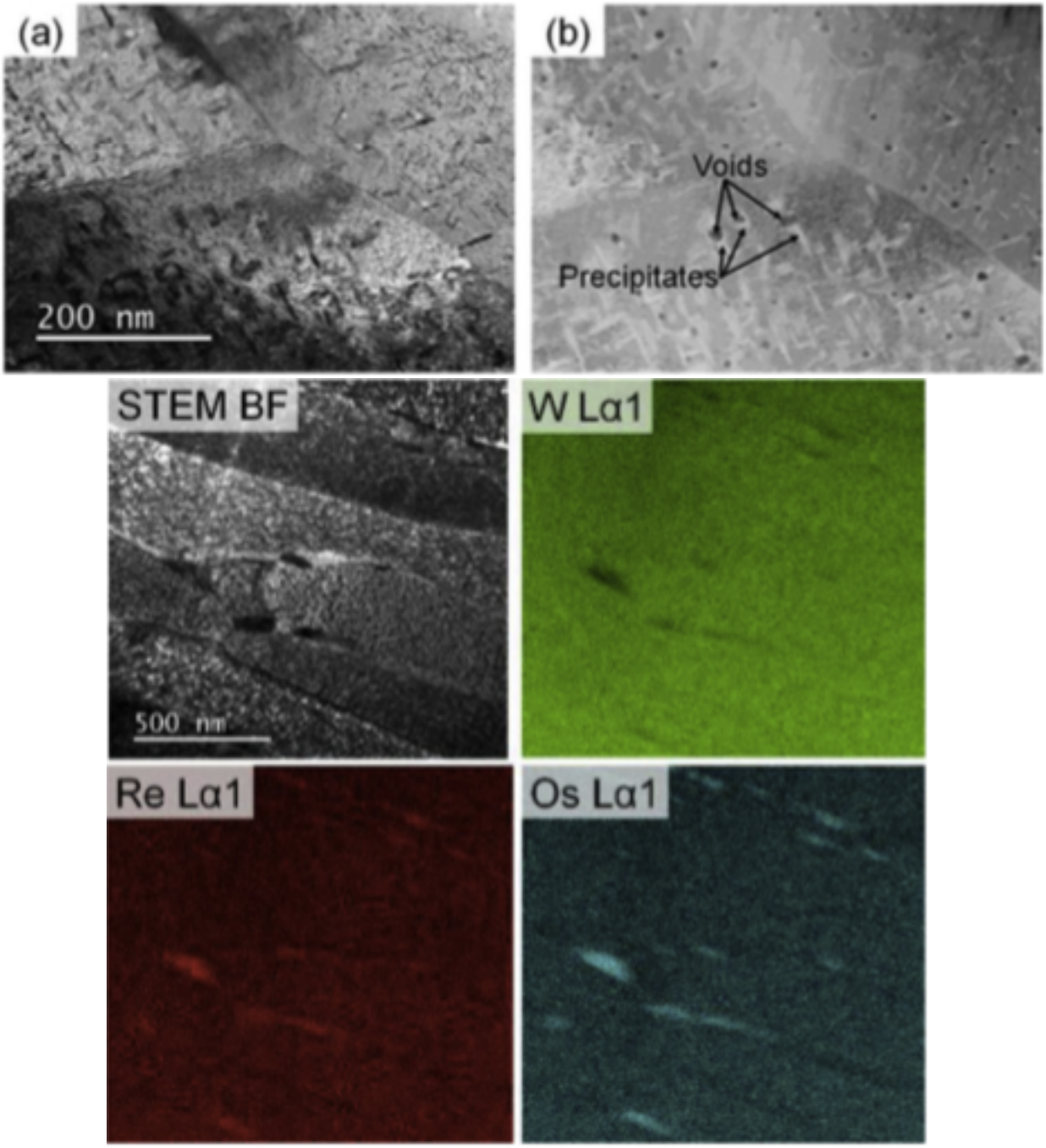

Figure 1.18: TEM/STEM micrographs of W after neutron irradiation showing loop, void, and Re/Os precipitate development [52].

In a reactor environment, the temperature operating window will be dictated by the temperature-induced mechanical property changes. Figure 1.21 shows the temperature operating

windows for W and other potential PFC materials. For W, the lower limit will be set by its low temperature fracture toughness and brittle nature. However, irradiation of W at low temperature can lead to significant hardening and increases in the DBTT. Brittle failure has been observed in pure W after neutron irradiation at 500 C to a $1x10^{26}$ m^{-2} neutron dose (< 2 dpa). Therefore, the minimum operating temperature is one that avoids radiation hardening and embrittlement, and is ~700-1000 C for pure W. The upper limit on the operational window is set by creep, void swelling, corrosion, and He embrittlement. Low swelling is predicted for W, but high temperatures may also drive recrystallization of W, which would affect its mechanical properties. In W, the upper temperature limit is estimated to be ~1200-1300 C [57].

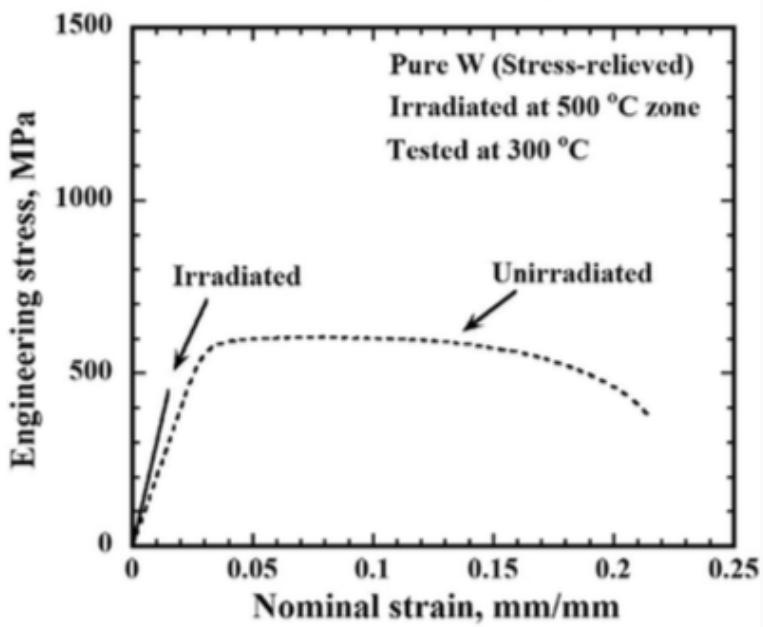

Figure 1.19: Stress-strain behavior of W before and after neutron irradiation indicating loss of ductility after neutron irradiation [55].

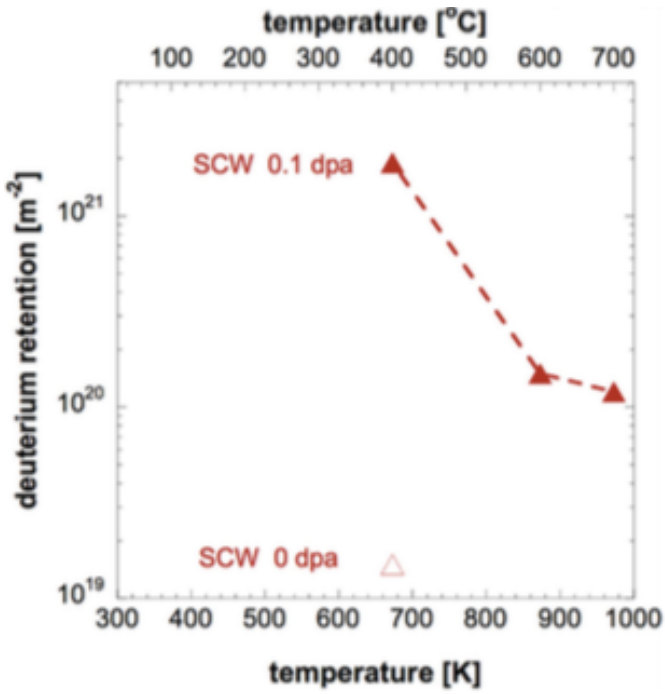

Figure 1.20: Deuterium retention in W with (0.1 dpa) and without (0 dpa) neutron irradiation showing neutron irradiation increases D retention [56].

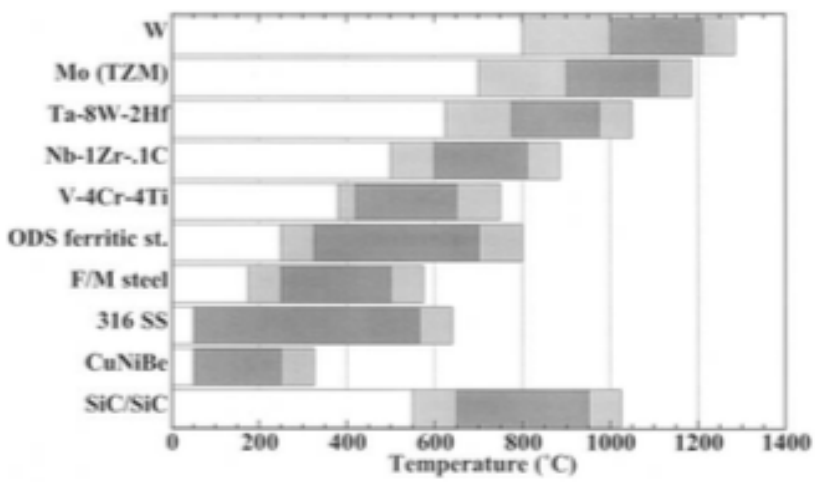

Figure 1.21: Ideal temperature operating windows for various materials in a fusion reactor environment [57].

To best identify the best plasma-facing material, there is a need to balance the bulk mechanical properties with the surface plasma-material interactions. The schematic in Fig. 1.22 shows that there is a need to balance oxidation, mechanics, deuterium interactions, transmutation, sputtering, and thermal properties to ensure that the material can be effectively used as a PFC. The schematic shows that tungsten is adequate in the thermal properties, sputtering, and D/H/T interactions categories. However, improvements must be made in the oxidation stability, mechanics, and transmutation properties. To improve on these properties, as indicated in the schematic, fabrication of W alloys or composites can improve the mechanical and oxidation

performance. However, these alterations will also have an impact on the other properties, including H/D/T interactions, sputtering, and thermal properties (and helium effects, not shown in schematic). This work attempts to explore alternative W-based materials to examine their properties in these categories to identify a material that has improved overall performance compared to pure W, and is acceptable in all categories. The motivation for this work came from the desire to improve the toughness and lower the DBTT of W. The work evolved to be multi-faceted to test the performance of the developed materials on many of these properties.

For example, the temperatures needed to ensure the material is in the ductile regime may also be a temperature at which ion-induced surface modification is enhanced. Therefore, there is a balance between the bulk and surface properties that must be considered when choosing the operating conditions. One must consider all material thermomechanical and irradiation properties at different temperatures to decide on the ideal material and operating condition. For example, ion-induced morphological changes must be balanced with recrystallization phenomenon with deuterium retention. Therefore, the materials of choice must be chosen that is acceptable in all categories, not just superb in one category. Additionally, there is a disconnect between the bulk material properties and how they correlate back to the surface to affect the plasma-material interactions. This synergy between the bulk (~µm's beneath the surface) and the near surface (~100's of nm's beneath the surface) is not well understood, but can dictate material performance.

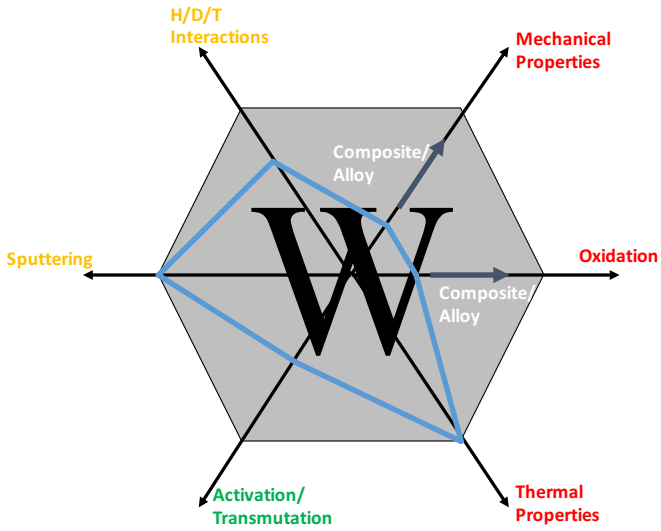

Figure 1.22: Radar chart of properties relevant in a fusion PFC environment and corresponding W performance, adapted from [58].

Novel Tungsten Materials and Tungsten Alloys

Controlling the microstructure of tungsten can alter the mechanical properties and behavior of tungsten on the macroscale. Significant efforts have been made to alter the grain size and distribution in tungsten, from creating nanocrystalline tungsten to bi-modal grained tungsten to tungsten alloys.

Characteristics of tungsten alloys

Tungsten's embrittlement issues and low ductility limit the effectiveness of tungsten for wide-reaching structural applications. The primary cause of embrittlement in tungsten is due to the segregation of impurities (O, C, N, S) to the grain boundaries, which weakens grain cohesion and introduces preferential cracking sites [45-47]. If the microstructure of a material can be controlled, for example, preventing the accumulation of impurities at grain boundaries, then the mechanical properties of materials can be altered.

Attempts to modify the microstructure of tungsten include adding oxides and carbides. Oxide- dispersion strengthened (ODS) alloys have been investigated, with compounds such as La_2O_3, ThO_2, and Y_2O_3 dispersoids being used [59-62]. Oxide dispersoids have been shown to distribute between tungsten grains and pin grain boundaries to limit grain growth. The addition of oxide particles shows the formation of metal-W-O complexes at grain boundaries, but excessive amounts of oxide particles can agglomerate at grain boundaries and act as crack initiation sites.

Strengthening tungsten with transition metals and their carbides has shown promise, as TiC [63], ZrC [64], HfC [65], and TaC [66] additions have demonstrated the ability to control the microstructure and impurity distribution to improve mechanical properties. Tungsten strengthened with TiC, TaC, and ZrC have shown increased strength by strengthening the grain boundaries and decreasing the average grain size. The second phase elements have an affinity for oxygen and carbon and can capture impurities and "clean" the grain boundaries. Dispersed particles were found intra-granularly as well as in grain boundaries. Dispersoids at boundaries pin grain boundaries, raise the recrystallization temperature, and form W-metal- C-O compounds that purify the boundaries and enhance grain boundary cohesion to enhance the ductility and increasing the hardness and toughness [63-75]. Z.M. Xie et al identified zirconium-carbon-tungsten-oxygen complexes at grain boundaries, creating coherent interfaces with the tungsten matrix. The coherent boundaries allowed for the improvement in strength and ductility, as shown below, by pinning dislocations within grains and capturing oxygen at grain boundaries and pinning grain boundary motion [64]. G. Song et al. have conducted extensive studies of ZrC/W composites with up to 50 vol.% ZrC [77]. Post-fabrication studies with XRD and EDS have shown the formation of zirconia, zirconium carbide, and tungsten carbide phases, attributed to the interdiffusion of carbon between ZrC and W powders during compaction. A (Zr, W)C solid solution is formed at W-ZrC interfaces, which can enhance grain boundary bonding [69]. These composites also demonstrated increased high temperature ablation resistance and good thermal shock resistance, attributed to the oxidative resistance of ZrC as compared to tungsten [69, 77]. Due to the enhanced grain boundary cohesion, the failure modes of W-ZrC composites are altered, from intergranular failure in pure W to transgranular failure in the composites.

Improvements in the ductility and toughness have also been achieved through alloying with titanium carbide and hafnium carbide [63, 70-75, 78, 79]. Reductions in the grain size were observed with TiC particles existing at and pinning grain boundaries. X. Ding et al. studied the impact of 1 wt.% TiC strengthening, showing increased hardness and decreased grain size when TiC added. Under nanoindentation, the Young's modulus of the alloy was determined to be 387 GPa, similar to the modulus of pure tungsten. However, W-TiC alloys demonstrated drastically reduced thermal conductivities as compared to pure tungsten [78].

Similar results are obtained in 0.5 wt.% TiC-strengthened tungsten as studied by S. Miao et al. The alloys exhibited a higher recrystallization temperature of 1600°C, but the TiC particles were stable, indicating their high temperature stability. As before, W-Ti-O-C complexes were observed in EDS investigations with particles both inter-granularly and intra-granularly [70]. C. Ren et al. demonstrated that, like ZrC, titanium-rich second phase particles can capture impurity oxygen from grain boundaries and pin tungsten grains, as shifts in the XPS spectra of Ti_2p region indicate the formation of titanium oxide instead of metallic titanium [78].

Few studies have been conducted on tantalum and tantalum carbide-strengthened tungsten. Small additions (0.5 wt.%) of TaC have been shown to decrease the DBTT of tungsten to 200-250°C by capturing oxygen impurities and forming homogenously distributed Ta_2O_5 particles in the tungsten matrix. The formation of these complexes enhance grain boundary strength and limit grain size, which contribute a fine grain size and enhanced low temperature ductility and toughness [80]. Additions of 1 wt.% TaC have been shown to increase the hardness of tungsten by pinning grains, while also having a higher thermal conductivity than pure tungsten [66].

Spark Plasma Sintering

Production of refractory metals such as W, Mo, V, and Ta is complicated by their high melting points. Common production methods are arc melting, sintering, hot pressing, and plasma spraying, all powder metallurgy techniques [45, 46]. Conventional sintering of tungsten powder is typically done with long hold times and high temperatures, resulting in coarse microstructures. However, in recent years, new sintering methods (such as spark plasma sintering) have been developed to provide rapid heating rates and short hold times for rapid consolidation to provide fine-grained microstructures. In this work, spark plasma sintering was used for sample fabrication to produce fine grained specimens.

Sintering

Sintering refers to the application of heat to a specimen to promote consolidation via thermally-activated mass transport. Conventional sintering is performed with radiative heating. Conventional sintering requires compaction of a Green Body and application of external heat to thermally activate mass transport. However, this technique typically utilizes long hold times and low heating rates, which commonly results in coarse-grained materials.

New methods employ electrical currents to provide “activated sintering.” These techniques are commonly called Spark Plasma Sintering (SPS), but also has many other names such as Plasma Assisted Sintering (PAS), Pulsed Electrical Current Sintering (PECS), electro-consolidation, and Field Assisted Sintering Technique (FAST) [81-84]. From now on in this document, the technique will solely be referred to as SPS. In all, SPS consists of concurrently applied pulsed electrical current and uniaxial pressure to enhance consolidation of the sample. This is shown in the schematic in Figure 1.23.

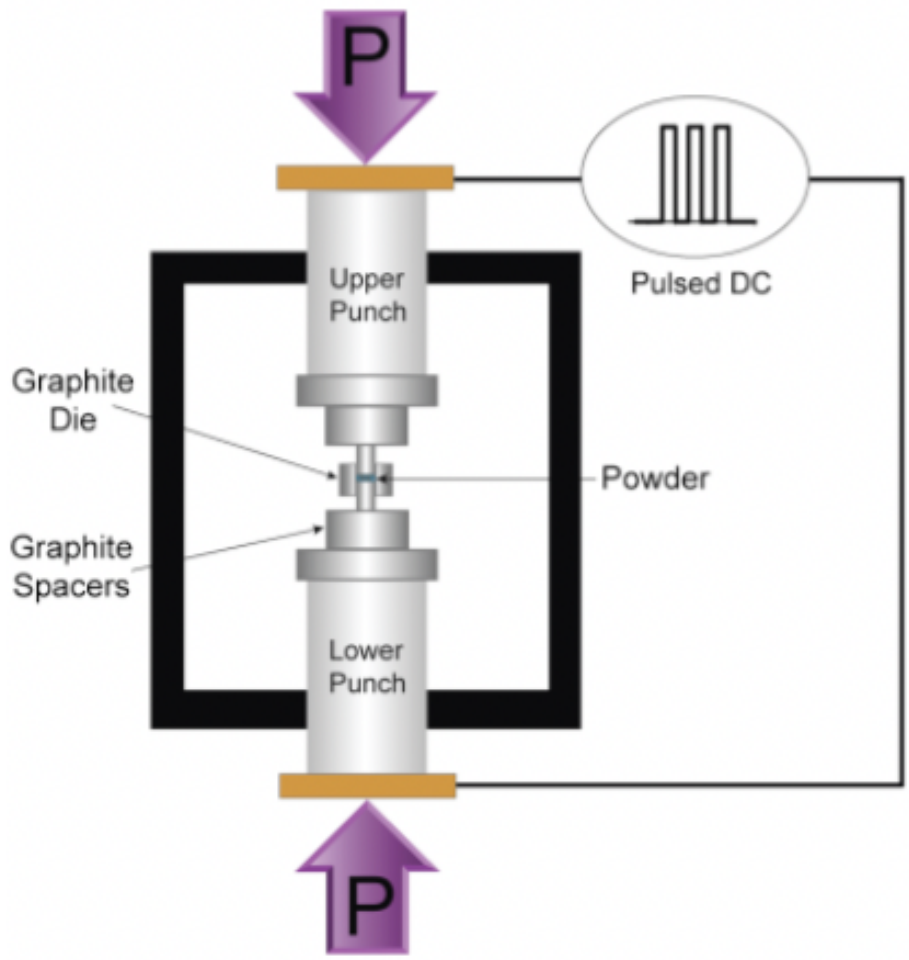

Figure 1.23: Design of spark plasma sintering device [82]. Pressure is applied from top and bottom while sample is rapidly heated by a pulsed DC current.

The advantages of SPS over conventional sintering are a lower sintering temperature and a higher heating rate [84]. By changing the current, hold time, and pulsing characteristics, the heating rates can approach 1000 C/min and temperature profiles can be altered [83]. A pulsed, DC current passes through the graphite die and the powder (if it is conductive) with a small (~1-5 V) voltage, providing Joule heating to the specimen which allows for the rapid heating rates [83]. The pulsed current in SPS is the main driving force for densification and is the distinguishing feature of the technique [85]. As mentioned above, the current heats the sample and die through Joule heating, though the amount of current flowing through the sample depends on the sample itself.

The applied DC current increases mass transport and densification [82, 86] by giving increased energy and mobility to enhance the densification kinetics. It is hypothesized that in the SPS process the current activates the surface by cleaning the surface of powder particles which can clean grain boundaries and allow for enhanced particle bonding [81, 82]. The initial stages of sintering involved grain boundary/surface diffusion. Diffusion leads to the formation of inter-particle necking, where particles elongate and contact neighboring particles [88-90], the progress of particle bonding and sintering is given schematically in Figure 1.24.

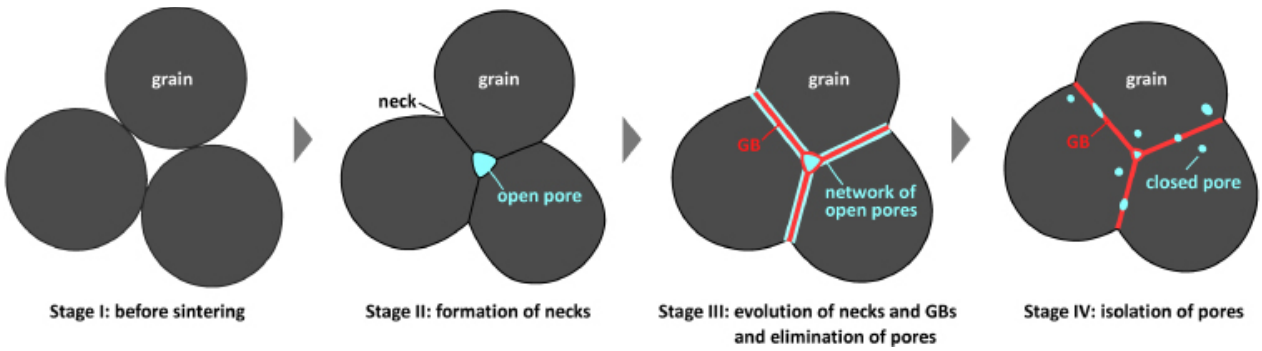

Figure 1.24: Progression of powder particle morphology during sintering process showing the compaction of particles, formation of grain boundaries, and elimination and isolation of pores [91].

Necking leads to amplified current though the contact points, which further enhances mass transport. The applied uniaxial force breaks up aggregate particles, collapses pores, and enhances densification [86, 90]. The high heating rate (up to 1000ºC/min) allows for short exposure times to high temperatures, enabling the sintering of nanostructured materials without significant grain growth. Additionally, the hold time can affect the properties of the final product. An increased holding time has been shown to increase both grain size and density [81-84].

Table 1.1: Change in microstructure and density as the sintering stage progresses, reproduced from [92].

Stage	Microstructural Features	Relative Density
Initial	Inter-particle neck growth	Up to ~65%
Intermediate	Connected porosity, particle growth	~65-90%
Final	Grain formation, isolated porosity	>~90%

During sintering, the applied current, uniaxial force, and Joule heating combine to increase mass transport and promote densification. During densification, grain boundary diffusion occurs between powder particles while the applied pressure provides stress-assisted diffusion which enhances densification [88]. In SPS and other activated sintering techniques, the surface free energy is increased and the grain boundary energy lowered to enhance kinetics and densification [90].

Following necking, grains begin to form and grain boundary diffusion contributes to mass transport. The applied pressure enhances grain boundary sliding and collapses pores [89]. The final stages of sintering involve pore shrinkage and grain growth [93]. Grain growth reduces the total grain boundary volume to minimize the grain boundary energy. During this process, pores become isolated [94, 95]. High maximum sintering temperatures and long hold times cause significant grain growth as grain growth is a thermally-activated process. Table 1.1 summarizes the growth regime as a function of final density during sintering. Figure 1.25 shows the W microstructures after sintering at different temperatures indicating greater density at higher temperatures.

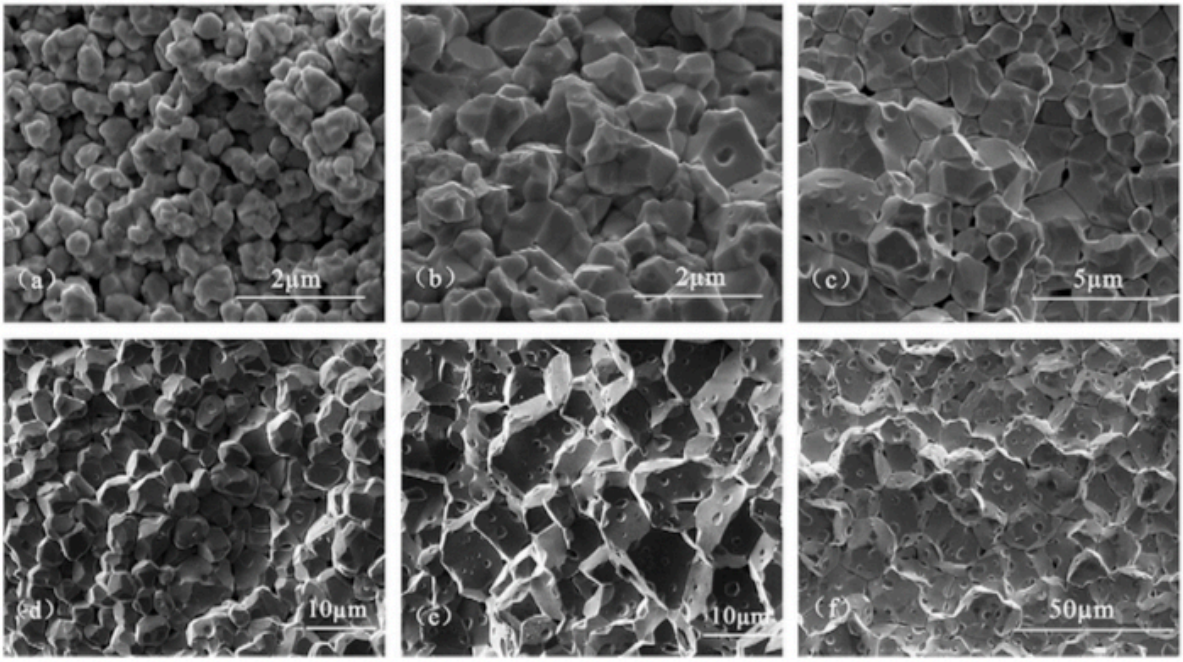

Figure 1.25: SEM micrographs illustrating the progression of powder particles coarsening into crystallized grains during sintering as the temperature increases from 1200-2000ºC (a-f) [94].

Sintering Tungsten

Conventional sintering of tungsten required the use of very high temperatures (>2000ºC) and long holding times (>20 hours) because of its high melting point, which led to non-fully-dense and coarse-grained materials [45, 46]. Therefore, conventional sintering cannot be relied upon to rapidly fabricate fine-grained W materials. Post-fabrication processing is required to reduce the grain size. Additionally, the long times required to fabricate W via conventional sintering shows that it is not scalable to produce tailored W materials for radiation environments, while activated sintering techniques may be able to bridge the gap.

With SPS, the required sintering time is drastically reduced and the microstructure can be controlled. SPS is favorable because the low process temperatures allow for the minimization of grain growth due to the temperature being below the material recrystallization temperature and a short dwell time [88, 90]. Activated sintering lowers the grain boundary energy and enhances the driving force for densification and enhances mass transport. Large nanoparticles have a large particle area which increases the densification driving force [88, 90]. Smaller nanoparticles have a higher sintering rate due to their low surface area [86].

Densification in tungsten is slower than other metals, but still achievable. Cho, et al. achieved >90% density with W powder sintered at 1750ºC, with the sample density increasing as the applied pressure increased [95]. El-Atwani, et al. achieved ~93% dense samples upon consolidation of 1 μm powder at only 1300ºC [96]. S. Chanthapan, et al. achieved >94% dense samples after sintering of sub-micron powder at 2000ºC for 5 minutes. This result also shows sample hardness increases with increasing sintering temperature due to the associated increase in density. It is also recognized that larger powder particles require a higher sintering temperature to achieve similar density as a sample fabricated from smaller powder particles [97]. S. Deng et al.

systematically studied temperature effects on sintering of tungsten. Sintering 1 μm powder under 40 MPa pressure, densification occurred at 1200-1400ºC, while grain growth without enhanced densification was observed above 1500ºC [94]. G. Lee et al. have studied the effect of hold time on sintering of tungsten powder. Sintering of micron-sized W powder at 60 MPa and temperatures of 1600-1800ºC, the highest densities (~95%) were observed with long hold times (30-60 minutes); however, the final grain size twice as large as the starting powder [98].

Sintering of tungsten alloys with SPS has also shown promise and the ability to achieve >90% density. S. Chanthapan, et al. have observed reduced sintering temperature and grain size after addition of WC particles, as well as an increase in hardness and densities near 99% [97]. Tantalum-carbide dispersion-strengthened tungsten with <1 wt. % has been sintered to ~97% density after holding at only 1800ºC for 1 minutes [66]. Similarly, Z.M. Xie, et al. have achieved ~98% dense samples of ZrC-strengthened tungsten after sintering at 1800ºC and 50 MPa for 2 minutes [64]. Finally, tungsten samples strengthened with 1.0 wt. % TiC have been achieved with 98.6% density after sintering at 1800ºC for 2 minutes [78].

Problem description and hypotheses

Tungsten is the material of choice for the divertor region in ITER as it has a high conductivity, low sputter yield, and high melting point. However, tungsten undergoes detrimental surface morphology changes under low and high energy ion bombardment. Also, due to its low DBTT, tungsten is difficult to shape and may be susceptible to cracking under transient heat loads. Thus, attempts have been made to create tungsten variations that are more ductile and suitable for use in a fusion environment. One type of these tungsten alloys is carbide-dispersion-strengthened tungsten. However, open questions remain regarding the properties of carbide-strengthened tungsten alloys under irradiation.

In prior work, the fabrication of tungsten alloys strengthened with zirconium carbide, titanium carbide, and tantalum carbide was investigated. Chemical composition and microstructure were analyzed after fabrication and correlated with alloy mechanical properties.

In this work, the behavior of these dispersion-strengthened alloys were investigated under low energy ion irradiations at low and high fluences. Exposures to ion bombardment and subsequent analysis of surface chemistry and morphology response was examined. Additionally, thermomechanical testing to understand the high temperature exposure effects and mechanical properties were performed. The following questions are proposed to guide the research:

1. Does the addition of dispersoids limit recrystallization by preventing W grain growth?
2. Is cracking and failure impacted by the presence of dispersoids?
3. Is there enhanced sputtering of dispersion-strengthened tungsten given the introduction of non-W elements?
4. Does the introduction of dispersoids trap deuterium and impede deuterium diffusion?
5. Can the dispersoids sequester helium into many small bubbles to prevent large bubble formation and effectively manage the helium inventory?

Based on these guiding questions, three main research areas of focus and associated hypotheses have been generated and will guide this work:

1. Impact of dispersoids on thermo-mechanical properties
    a. Addition of a 1.1wt.% dispersoids effectively pins W grains, limiting recrystallization. However, the W-W and W-dispersoid interfaces are not immune to cracking under loading.
2. Impact of dispersoids on deuterium trapping
    a. Deuterium retention will be increased due to the presence of dispersoids.
3. Impact of dispersoids on helium behavior
    a. The dispersoids trap He in small clusters, limiting He bubble formation in the W matrix.
    b. At low dispersoid concentrations, the near-surface behavior mirrors that of pure W.

References

[1] S. Chu and A. Majumdar. *Nature*, **488**, 2012. 294-303.
[2] J. Friedberg. *Plasma Physics and Controlled Fusion.* Cambridge: Cambridge University Press, 2007.
[3] R. Toschi. *Fus. Eng. and Des.* **36** (1997) 1-8.
[4] G. Federici, et al. *Nuclear Fusion*, **41**, No. 12R (2001)
[5] EUROfusion, "Tokamak principle." https://www.euro-fusion.org/2011/09/ tokamak-principle-2/, 2015.
[6] "Tokamaks." https://www.euro-fusion.org/fusion/fusion-technology/types-of-fusion-machines/tokamaks/, 2015.
[7] J.D. Lawson. *Some Criteria for a Power Producing Thermonuclear Reactor. Atomic Energy Research Establishment, Hanvell, Berks.*
[8] "Lawson Criterion." https://www.euro-fusion.org/2005/12/50-years-of-lawson-criteria, 2015.
[9] G.A. Cottrell. *Mat. Sci. and Tech*. **22** (2006) 869-880.
[10] E. Taglauer. *Nuc. Instr. And Meth. In Phys. Res. B*. **13** (1986) 218-224
[11] J. Wesson. *Tokamak*s. Oxford: Clarendon Press 2004.
[12] R.A. Pitts, et al. *Journal of Nuclear Materials* **415** (2011) 957–964.
[13] N. Baluc. *Plasma Phys. Control. Fusion* **48** (2006) 165–177.
[14] A. Loarte, et al. *Nucl. Fusion* **47** (2007) S203–S263.
[15] R.V. Jensen, et al. *Nucl. Fus*. **17** 6 (1977)
[16] J. Linke, et al. *Matter Radiat. Extremes* **4**, 056201 (2019).
[17] M.R. Gilbert, et al. *Nucl. Fusion* **52** (2012) 083019.
[18] S.J. Zinkle and L.L. Snead, *Annu. Rev. Mater. Res*. 2014. 44:241–67.
[19] R. Averback and D. Seidman. *Materials Science Forum Vols.* **15-18** (1987) 963-984.
[20] R. Averback. *Journal of Nuclear Materials* **216** (1994) 49-62.

[21] M.W. Guinan, et al. *Journal of Nuclear Materials* **103 & 104** (1981) 1319-1324.

[22] I. Beyerlein, et al. *Mater. Today* **16** (2013) 443-449.

[23] G. Ackland, *Science* **327** 2010.

[24] X.M. Bai, et al. *Science* **327 (**2010) 1631-1634.

[25] X. Zhang et al. *Progress in Materials Science* **96** (2018) 217–321.

[26] M. Rose, et al. *Nuclear Instruments and Methods B*, **127/128** (1997) 119-122.

[27] N. Nita et al. Journal of Nuclear Materials 329–333 (2004) 953–957.

[28] Y. Chimi, et al. Journal of Nuclear Materials 297 (2001) 355-357.

[29] O. El-Atwani et al. *Journal of Nuclear Materials* **458** (2015) 216–223.

[30] O. El-Atwani et al. *Nucl. Fusion* **54** (2014) 083013.

[31] O. El-Atwani et al. *Acta Materialia* **149** (2018) 206-219.

[32] O. El-Atwani, et al. *Materials Research Letters*, **5**:5 (2017) 343-349.

[33] Q. Wei et al. *Acta Materialia* **54** (2006) 4079–4089.

[34] Q. Wei et al. *Acta Materialia* **54** (2006) 77–87.

[35] B.E. Shuster, et al. *J. of Mater.* **63** (2011) 27-31.

[36] A. Suslova, et al. *Sci. Rep*. **4**, 6845; DOI:10.1038/srep06845 (2014).
[37] S. Simoes, *Nanotechnology* **21** (2010) 145701 (12pp).

[38] R. Dannenberg, et al. *Thin Solid Films* **379** (2000) 133-138.

[39] M.C. Iordache, *Nanostructured Materials* **11** (1999) 1343-1349.

[40] O.K. Donaldson, et al. *J Mater. Res.* **33** (2018) 68-804.

[41] J. Brodrick et al. *Journal of Nuclear Materials* **445** (2014) 291–297.

[42] B. Mazumder et al. *Nucl. Mater. & Energy* **1** (2015) 8–12.

[43] P. D. Edmondson et al. *Scripta Materialia* **65** (2011) 731–734.

[44] J. Spitznagel, et al. *J. Nucl. Mater*. **122 & 123** (1984) 253-253.

[45] E. Lassner and W.D. Schubert. *Tungsten: Properties, Chemistry, Technology of the Element, Alloys, and Chemical Compounds*. Kluwer Academic. Plenum Publishers. New York, NY. 1999.
[46] E. Pink and R. Eck. Ch. 10: *Refractory Metals and Their Alloys*.
[47] U.K Vashi, et al. *Metallurgical Trans.* **1** (1970) 1769-1771.
[48] T. Shen, et al. *Journal of Nuclear Materials* **468** (2016) 348-354.
[49] T. Dummer, et al. *Acta Mater.* **46**, No. 17, pp. 6267-6290, 1998.
[50] Y. Hiraoka et al. *Advances in Mat. Sci. and Eng*. 2011.

[51] A. Hasegawa et al. *Journal of Nuclear Materials* **471** (2016) 175-183.

[52] T. Koyanagi et al. *Journal of Nuclear Materials* **490** (2017) 66-74.
[53] M.R. Gilbert, et al. *Nucl. Fusion* **51** (2011) 043005 (13pp).
[54] A. Khan et al. *Journal of Nuclear Materials* **474** (2016) 99-104.
[55] T. Miyazawa, et al. *Journal of Nuclear Materials.* **529** (2020) 151910.
[56] M. Shimada, et al. *Fusion Engineering and Design* **136** (2018) 1161–1167.
[57] S.J. Zinkle, N.M. Ghoniem *Fusion Engineering and Design* **51–52** (2000) 55–71.

[58] A. Litnovsky. *Critical Issues of W-based PFMs for DEMO*. 6th IAEA DPWS Workship, Moscow, Russia, October 2019.
[59] R. Liu, et al. *J. Nucl. Mater.* **451** (2014) 35-39.
[60] Z. Zhou, et al. *J. Nucl. Mater.* **431** (2012) 202-205.
[61] Y. Kim, et al. *Int. J. Refractory Metals & Hard Mater.* **27** (2009) 842–846.
[62] M. Yar, et al. *J. Nucl. Mater.* **408** (2011) 129–135.
[63] Y. Kitsunai, et al. *J. Nucl. Mater.* **271-272** (1999) 423-428.
[64] Xie, Z. M. et al. *Sci. Rep*. **5**, 16014.
[65] D. Lee, et al. *Int. J. Refractory Metals and Hard Mater.* **44** (2014) 49–53.
[66] X.Y. Tan, et al. *Powder Tech.* **269** (2015) 437–442.
[67] Luo, L. et al. *Sci. Rep*. **6**, 32701.
[68] P. Makorov and K. Povarova. *Principles of the alloying of tungsten and development of the manufacturing technology for the tungsten alloys.* 15th International Plansee Seminar (2001) 1 464-484.
[69] G. Song, et al. *Mater. Sci. and Eng. A* **334** (2002) 223–232.
[70] S. Miao, et al. *Mater. Sci. and Eng. A* **671** (2016) 87–95.
[71] Y. Ishijima, et al. *Mater. Trans.*, **46,** No. 3 (2005) pp. 568 to 574.
[72] H. Kurishita, et al. *J. Nucl. Mater.* **398** (2010) 87–92.
[73] Y. Ishijima, et al. *Mater. Sci. and Eng. A* **473** (2008) 7–15.
[74] H. Kurishita, et al. *Mater. Sci. and Eng. A* **477** (2008) 162–167.
[75] H. Kurishita, et al. *Adv. Mater. Research* Vol. **59** (2009) 18-30.
[76] Y. Wang, et al. *Materials Science and Engineering* A **528** (2011) 1805–1811.
[77] G. Song, et al. *Journal of Materials Science* **36** (2001) 4625– 4631.
[78] X. Ding, et al. *Fusion Engineering and Design* **92** (2015) 29–34.
[79] C. Ren, et al. *Int. Journal of Refractory Metals and Hard Materials* **65** (2017) 2–8.
[80] S. Miao, et al. *Int. Journal of Refractory Metals and Hard Materials* **56** (2016) 8– 17.
[81] J. Groza and A. Zavaliangos. *Mater. Sci. and Eng. A* **287** (2000) 171–177.
[82] Z. Munir, D, et al. *J. Am. Ceram. Soc*., **94** [1] 1–19 (2011).
[83] J. Groza and A. Zavaliangos. *Rev. Adv. Mater. Sci.* **5** (2003) 24-33.
[84] Z. Munir, et al. *J. Mater. Sci*. **41** (2006) 763–777.
[85] J. Langer, M. Hoffmann, and O. Guillon. *Acta Materialia* **57** (2009) 5454–5465.
[86] J. Groza. *Ch. 13: Powder Consolidation* in: Non-Equilibrium Processing of Materials. Elsevier Science, Oxford, UK. (1999) 347-372.
[87] Z. Zhaohui, et al. *Materials Letters* **62** (2008) 3987–3990.
[88] Z. Gao, et al. *Metall. And Mater. Trans. B*. **43B**, 2012, 1608-1614.
[89] A. Moitra, et al. *Acta Materialia* **58** (2010) 3939–3951.
[90] N.C. Kothari. *Sintering kinetics in tungsten powder.* J. of the Less-Common Metals. 5 (1963) 140- 150.

[91] H. Tanaka, et al. *Superconductor Science and Technology,* **25** (2012) 115022.
[92] A. Upadhyaya, and G.S. Upadhyaya. Powder Metallurgy: Science, Technology, and Materials. Universities Press, India; 2011, 171-227.
[93] W. Li, et al. *J. Mater. Sci*. (2012) **47**:7036–7046.
[94] S. Deng, et al. *Powder Tech.* **310** (2017) 264–271.
[95] K. Cho, et al. *Mater. and Manufacturing Processes* **19** (2004) 619-630.
[96] O. El-Atwani, et al. *Mater. Sci. and Eng. A* **528** (2011) 5670-5677.
[97] S. Chanthapan, et al. *Int. J. Refractory Metals and Hard Mater*. **31** (2012) 114–120.
[98] G. Lee, et al. *Int. J. Refractory Metals and Hard Mater.* **61** (2016) 22–29.

CHAPTER 2: EXPERIMENTAL AND ANALYSIS FACILITIES

Numerous experimental facilities were used to examine the microstructure and behavior of DS-W materials. Experiments and analysis were performed using many different techniques and equipment at different facilities. This chapter summarizes the experimental and analysis facilities and techniques used to decipher the performance of DS-W materials.

Experimental Facilities Utilized

IGNIS

The main irradiation and analysis facility at the University of Illinois is the Ion Gas Neutral Interactions with Surfaces (IGNIS) chamber. The IGNIS chamber shown in Fig. 2.1 is an ultra-high vacuum surface modification and analysis facility that allows for *in-situ* irradiation and analysis without atmospheric exposure allowing one to investigate the irradiation-driven surface modifications. Instruments of interest attached to the chamber are the sample manipulator, a Gen IV plasma source, a KRI ion source, an x-ray source, a hemispherical energy sector analyzer, a high pressure residual gas analyzer (RGA), and multiple NTI focused ion sources.

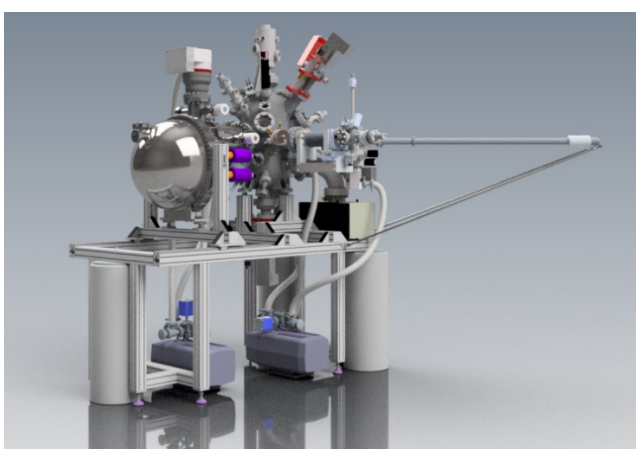

Figure 2.1**:** Computer Aided Design (CAD) rendering of the IGNIS facility at UIUC.

The sample manipulator (UHV Design) is made of stainless steel and can tilt samples to any angle, heat the sample to ~1073K, and bias the sample to ~100 V. The samples manipulator

can monitor the ion current on the sample surface in real time to give an accurate reading of the flux to appropriately calculate the ion fluence [1].

One ion source on IGNIS is a Tectra Gen IV plasma source (Tectra GmbH, Frankfurt Germany). The source utilizes a magnetron generator to create a plasma in a ceramic cup before using molybdenum grids to extract and excite ions from 100 to ~1500 eV. This source is a broad beam source with a beam width of 4 cm, that can be used with inert gases as well as reactive gases such as H, D, and He. The source has an energy range from 250 to 2000 eV and delivers ion currents varying from 15 µA to 60 µA depending on the energy and gas species. The working distance from the source to the sample is 25 cm.

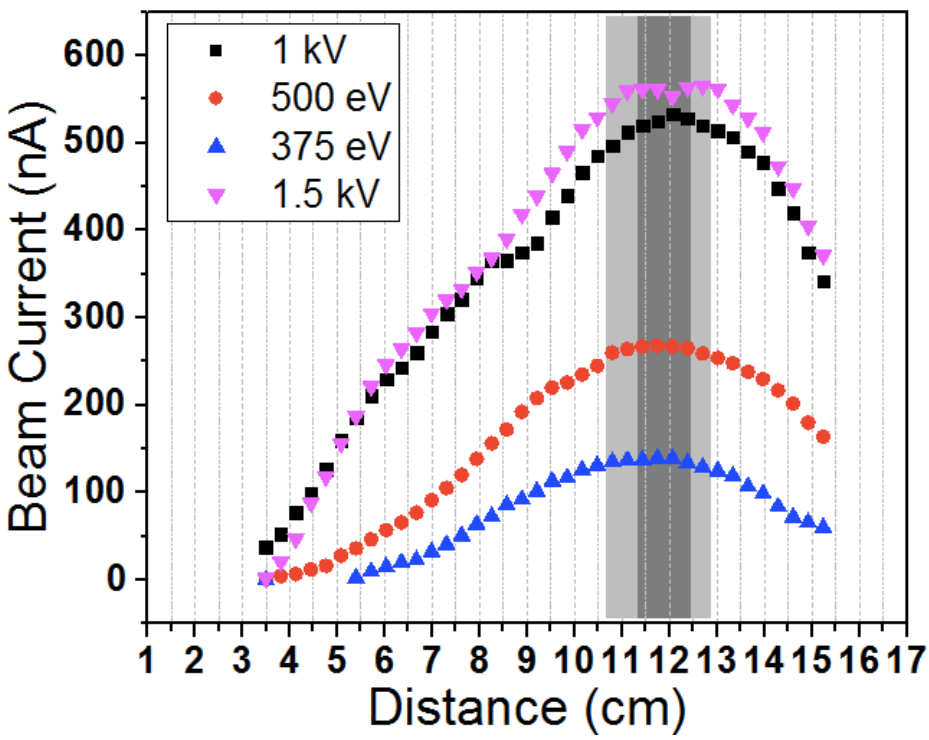

Figure 2.2: Beam profiles of Tectra Gen II plasma source for different Ar ion energies. The light grey region represents the size of the sample puck and the dark grey represents the typical size of a sample, with respect to the beam size.

Beam profiles shown in Fig. 2.2 were determined by changing the position of the ion current measurement plate across in 0.25mm increments and measuring the ion flux at each position. The beam can be approximated with a Gaussian shape with a FWHM of ~3.5 in. The beam size depends on the ion energy, with smaller beams achieved at higher ion energy [2, 3].

The low energy, high flux ion source attached to IGNIS is the KRI eH 400 source. This ion source is a Kauffman source, of the End-Hall type. The eH400 is a gridless ion source operating via DC Magnetic Confinement principles. A W filament is used to thermionically emit electrons which are attracted to a DC-biased metal anode. The electrons confined in a magnetic field and collide with the feed gas producing a high density plasma or many different gas species, including Ar, O_2, N_2, Ne, D_2, and He. It has a wide beam with a 45-degree divergence angle from the source [4].

For use with high energy or focused ion beams, a Non-Sequitor Technologies (NTI) 1402 or 1404 ion source is used. These ion sources operate in a similar manner to accelerate He, Ne, or Ar ions to the sample surface at energies from 500 to 3000 eV. These sources are filament-based sources that ionize working gas atoms and accelerated towards the sample via electrostatic lenses with a beam size of ~ 1 mm. The 1402 has a thoria-doped tungsten filament while the 1404 has a thoria-coated iridium filament.

Attached to IGNIS is a specially designed hemispherical energy sector analyzer, the PHOIBOS EP 150 (Specs, Berlin Germany), and its associated x-ray source, the XR 50 X-Ray source (Specs). The XR 50 X-ray source is a dual anode source with Mg and Al anodes that is used for in-situ XPS analysis of samples in IGNIS. The source is differentially pumped so XPS analysis can be performed at pressures above the maximum operating limit of the source. The anodes emit radiation in the K-α 1 and 2 lines, at 1253 eV for Mg and 1486 eV for Al. An aluminum window is placed on the end of the source to suppress Brehmsstralung radiation and prevent stray electrons from the filament from reaching the analyzer. X-rays then hit the sample and excite characteristic lines in the sample dependent on the sample elemental composition. When the sample is excited by the x-rays, electrons are emitted at characteristic energies and are collected by the analyzer [5].

The energy analyzer shown in Fig. 2.3 is a spectrometer designed to capture and resolve and discriminate the energy of electrons or ions emanating from the sample surface. The working distance between the sample and analyzer is 3 cm. The analyzer is differentially pumped to allow for the sample to be at mTorr pressures while the interior of the analyze is maintained at UHV conditions. There are two differential pumping stages and a third turbomolecular pump near the detector. Two apertures separate the differential pumping stages. The front iris aperture primarily limits the flux of electrons to the analyzer. The rear aperture size can be varied to change the pressure between the differential pressure stages. The pressure at the detector needs to be kept below 3.75×10^{-6} Torr during operation of the analyzer [6].

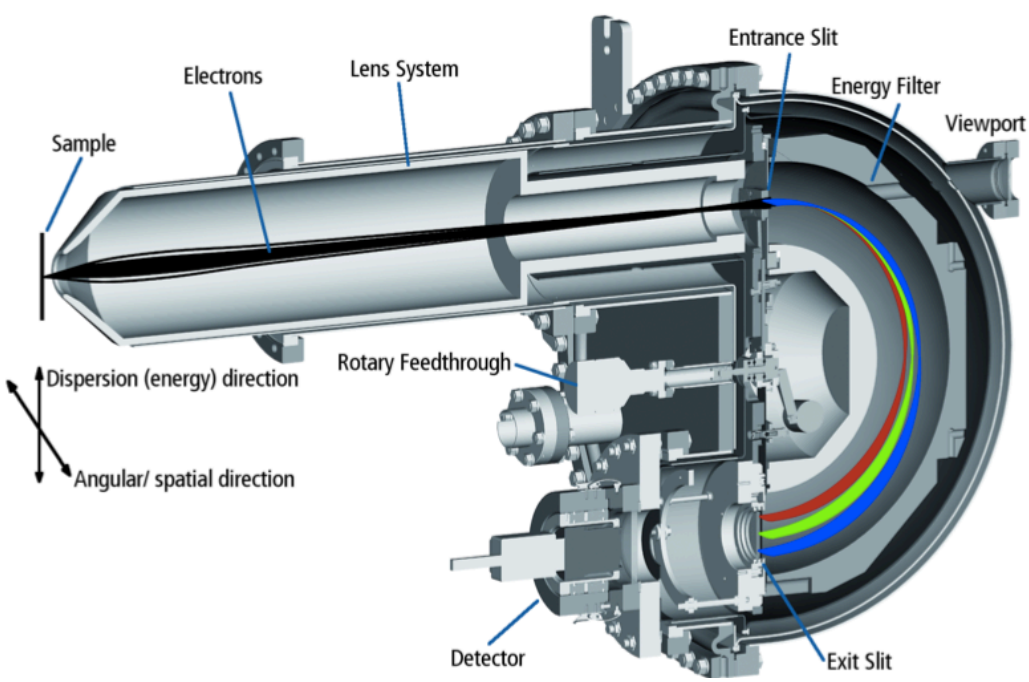

Figure 2.3: Cut-away schematic of analyzer and detector [6].

During operation, charged particles are emitted from the sample and enter the analyzer's lens system. These charged particles have a wide energy and angular distribution which are then focused by the electrostatic lenses and directed towards the energy filter. The entrance slit is used to further restrict the angular distribution of electrons allowed to the detector. A wide slit allows a lot of electrons through, but offers poor energy resolution. After passing through the entrance slit, electrons then enter the hemispherical part of the analyzer. The two concentric spheres of the analyzer are biased to allow only electrons with a particular energy range to pass through, as shown below. Electrons are the correct energy (the pass energy) pass through to the filter. Electrons with too high or too low of an energy will be rejected. Electrons with the correct energy leaving the exit slit enter the detector [6]. A sample XPS spectrum of a W-Re alloy (W-26wt.%Re) is shown in Fig. 2.4.

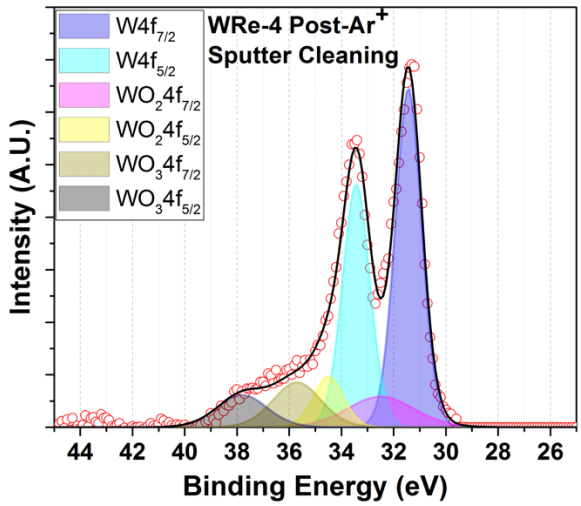

Figure 2.4: XPS spectra of the W and Re regions of the W-2.2%Re specimen after Ar sputter cleaning to remove adventitious carbon. Metallic W and W oxide peaks are observed, but no metallic Re or Re oxide peaks are present [7].

For sputtering yield investigations, a quartz crystal microbalance-dual crystal unit (QCM-DCU) is installed in IGNIS (Inficon SQC-310). It is mounted on a linear transfer arm and is inserted to the same position for each measurement to collect the same solid angle of sputtered material. A picture of the inside of the IGNIS chamber showing the QCM-DCU subtending the sample is shown in Fig. 2.5.

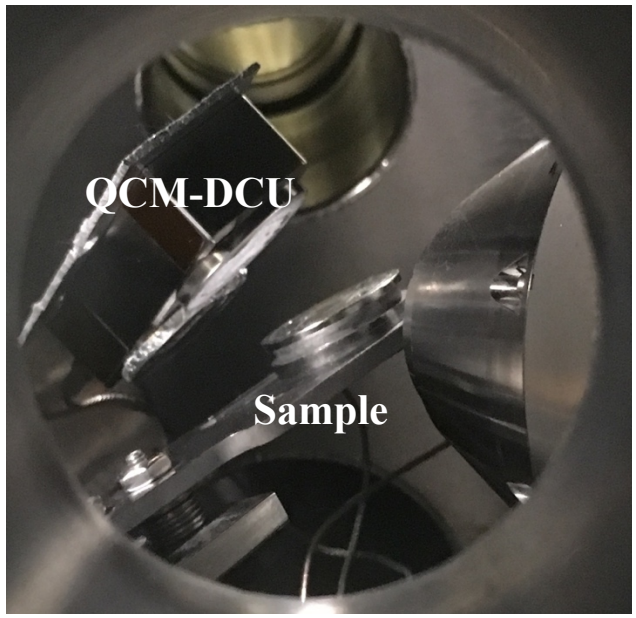

Figure 2.5: Image of QCM-DCU crystal positioned over sample in IGNIS.

The crystals are Au-coated AT-cut, quartz crystals, with a resonant frequency of 6 MHz. On the QCM-DCU, one crystal is covered with Al foil to prevent collection of material. During an experiment, the unexposed crystal collects the sputtered material, resulting in a steady decrease in its frequency. Meanwhile, the covered crystal frequency remains unchanged as a reference. The frequencies of both crystals are tracked in real time and relayed to the computer. Over the course of the experiment, the change in frequency of the exposed crystal relative to the covered crystal is tracked, and used to calculate the sputtering yield. An example of the change in crystal frequency versus time is shown in Fig. 2.6.

Physical sputtering is a kinetic process that occurs when an incident, energetic particle hits a surface atom. The incident ion loses energy to the target atom during the collision process, and the first-struck atoms are denoted as Primary Knock-On Atoms (PKAs). A surface atom is sputtered if the incident ion transfers enough energy to the target atom for it to overcome the surface binding energy and exit the surface. The maximum amount of energy that can be transferred to a surface atom by the incident ion can be described by the maximum energy transfer equation:

$$T = \frac{4m_1 m_2}{(m_1 + m_2)^2} E$$

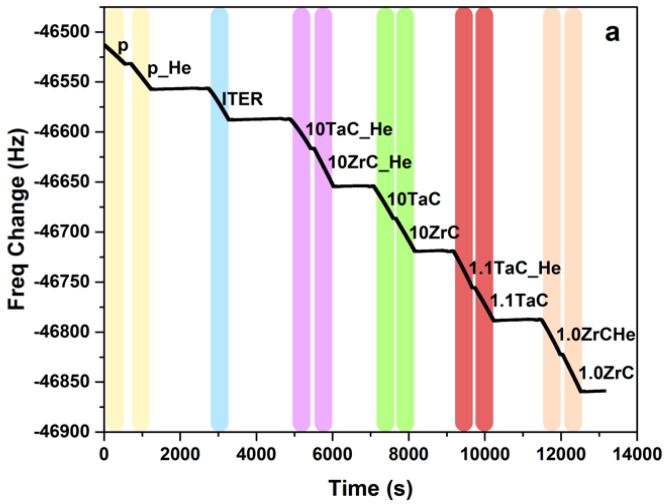

Figure 2.6: Representative QCM crystal frequency change vs. time for sputtering experiments. Slope of line can be converted to the sputtering yield.

The sputtering yield is the total number of surface atoms that are sputtered per incident ion dose. The yield depends on many factors, including the target mass, solid angle, surface binding energy, ion energy, ion angle, ion mass, among other factors. Sputtering yields increase as the incident ion angle increases from 0 to ~60 degrees, after which the yield declines. Additionally, sputtering yields increase with increase incident ion energy beyond a threshold energy below which no sputtering occurs.

Experimentally, the sputtering yield is determined by utilizing a Quartz Crystal Microbalance – Dual Crystal Unit (QCM-DCU). The sputtering yield is experimentally determined by collecting a fraction of the sputtered plume of particles and tracking the total incident ion dose [8]. As material is deposited on the crystal, the mass of the crystal changes according to the following formula:

$$M_i = \frac{DS^{QCM}Y\Omega m X_i}{N_A}$$

where D is the total incident ion fluence, S is the sticking coefficient of sputtered atoms that stick to the crystal (assumed to be 1), Y is the yield, Ω is the solid angle subtended by the crystal, m is the mass of tungsten, χ_i is the fraction of sputtered particles that are ions (assumed to be 1), and N_A is Avogadro's Number. As mass is deposited on the crystal, the frequency change relative to the starting frequency is tracked. The mass deposited on the crystal is:

$$M_{QCM} = \frac{\Delta f}{f} M_{crystal}$$

where Δf is the frequency change of the crystal and $M_{crystal}$ is the mass of the crystal. As sputtered particles are incident on the QCM crystal, material accumulated on the crystal can be sputtered. This self-sputtering term accounts for the reflection coefficient of energetic neutral particles hitting the crystal surface. This effect on the mass measured by the QCM is determined by

$$M_{QCM} = \frac{\Delta f}{f} M_{crystal}(1 + R_i Y_i^{QCM} \Omega_i)$$

Taking into account the mass lost by the tungsten sample, the mass deposited on the crystal, and the variation due to self-sputtering, the following equation can be used for approximating the sputtering yield:

$$Y = \frac{1}{DS^{QCM}Y\Omega mX_i}\frac{\Delta f}{f}M_{crystal}(1 + R_i Y_i^{QCM}\Omega_i)$$

Magnum-PSI Facility

High flux D and He irradiations were carried out at the Magnum-PSI facility at the Dutch Institute for Fundamental Energy Research (DIFFER) in Eindhoven, the Netherlands. A schematic of the facility is shown in Fig. 2.7.

In order to simulate the environment in the divertor region of a tokamak, the Magnum-PSI facility was constructed. The Magnum-PSI facility is a linear plasma device capable of delivering high flux ($10^{25}m^{-2}s^{-1}$) ions at low energies (<50 eV) to material surfaces to simulate the divertor environment in a tokamak. A cascaded arc plasma source generates a high density plasma (10^{19} m^{-3}) with electron temperatures (measured via Thomson Scattering) of 0.1 – 10 eV. The samples are biased to set the incident particle energy, and the particle flux allows for a steady-state peak heat flux of 10 MWm^{-2}. The samples are heated via ion bombardment and temperature is controlled via water cooling. Sample temperature is monitored with an FLIR fast IR camera (SC 7500-MB) and a Far Associates multiwavelength pyrometer (FMPI-I) [9, 10].

In addition to steady-state ion bombardment, the Magnum-PSI facility can also simulate Edge Localized Modes (ELMs) by pulsing a high powered Nd:YAG laser to deliver a laser pulse to raise the temperature. These plasma parameters allow for Magnum-PSI to provide the most accurate representation of the ITER divertor compared to other linear plasma devices, as shown the Figure 2.8 [10]. Thus, Magnum-PSI offers an ideal testing facility for exposing tungsten to high heat and particle fluxes to study surface damage and particle retention mechanisms.

Collaboration with Texas A&M University and Accelerator Facility of Prof. Lin Shao

High energy W^{2+} self-ion irradiation was performed on pure W samples to examine the impact of bulk displacement damage on the near-surface plasma-material interactions. Three ITER-grade tungsten samples were irradiated with 3.5 MeV W^{2+} ions at 700 C to induce knock-on damage in the bulk. Specimens were irradiated to 3 distinct fluences, $1.4x10^{14}$ cm^{-2}, $1.4x10^{15}$ cm^{-2}, and $1.4x10^{16}$ cm^{-2} to simulate knock-on damage via neutron irradiation to 1dpa, 10 dpa, and 100 dpa, respectively. Irradiations were performed with a 1.7 MeV Tandetron Accelerator at Texas A&M University [11].

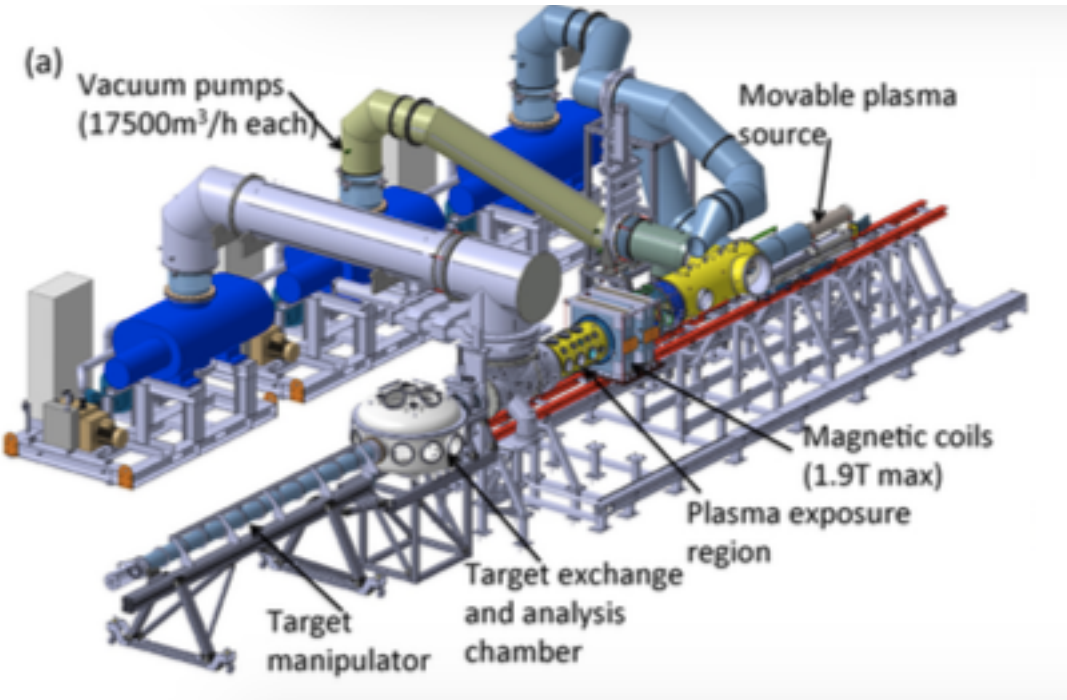

Figure 2.7: Schematic of the Magnum-PSI linear plasma device at the FOM-DIFFER institute [9]. The facility is a cascaded arc source that extracts energetic ions to the sample surface. This facility was used for high fluence, high temperature D and He exposures. In ITER, the minutes-long plasma shots combined with transient Edge Localized Modes (ELMs).

The implantation profile of 3.5 MeV W^{2+} ions in pure W calculated via SRIM-2008 using a 35 eV W displacement energy is shown in Fig. 2.9. The Stopping Range of Ions in Matter (SRIM) simulation tool is a Binary Collision Approximation (BCA) code in which an incident ion with a given energy impacts a material matrix with a given the composition. The incident ion creates knock-on damage within the matrix and results in a damage cascade. The trajectories and positions of the displaced atoms and incident ion are tracked and the position of implanted ions, distribution of displaced atoms, and amount of sputtered surface atoms (among other quantities) can be determined via SRIM. In this work, SRIM is used to estimate the displacement damage profile due to W ion bombardment (shown here) and the displacement damage and He implantation profile under He bombardment (shown in Section 2.3.1).

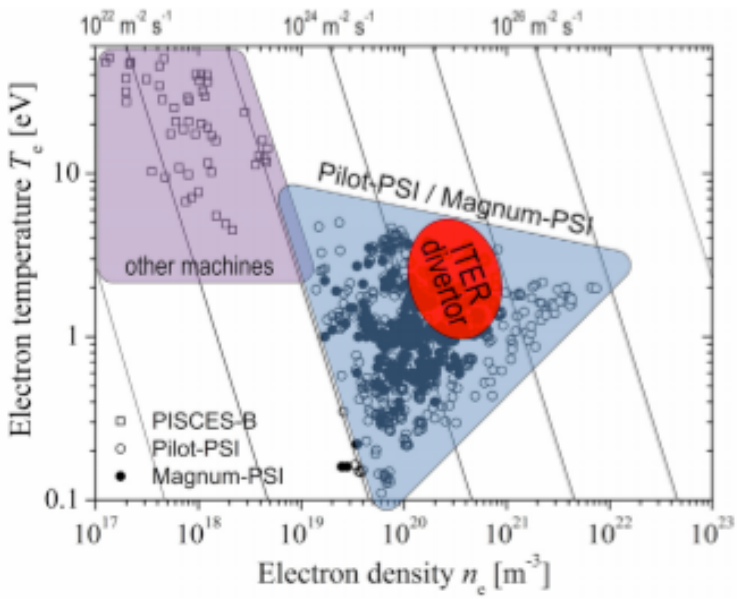

Figure 2.8: Plasma parameters of the Magnum-PSI facility and other linear plasma devices as compared to the expected conditions in the ITER divertor [10].

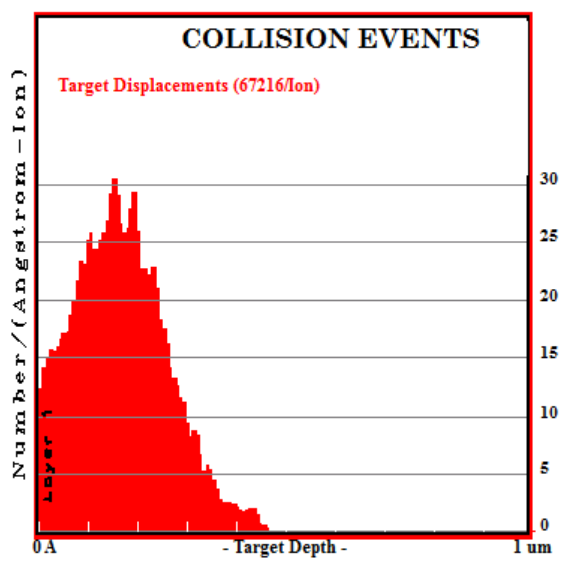

Figure 2.9: Implantation profile of 3.5 MeV W ions in a pure W target, as calculated via SRIM [14].

Following ion implantation, the surface microstructure is relatively unchanged. Figure 2.10 shows no blistering or exfoliation of the surface following irradiation.

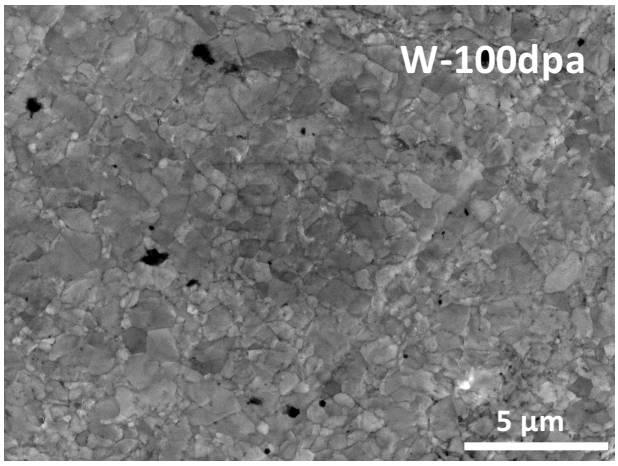

Figure 2.10: SEM micrograph of pure W sample after exposure to 3.5 MeV W^{2+} implantation to simulate 100 dpa irradiation.

However, the impact of the irradiation can be observed by investigating the near-surface mechanical properties, as shown in the increase in hardening in Figure 2.11.

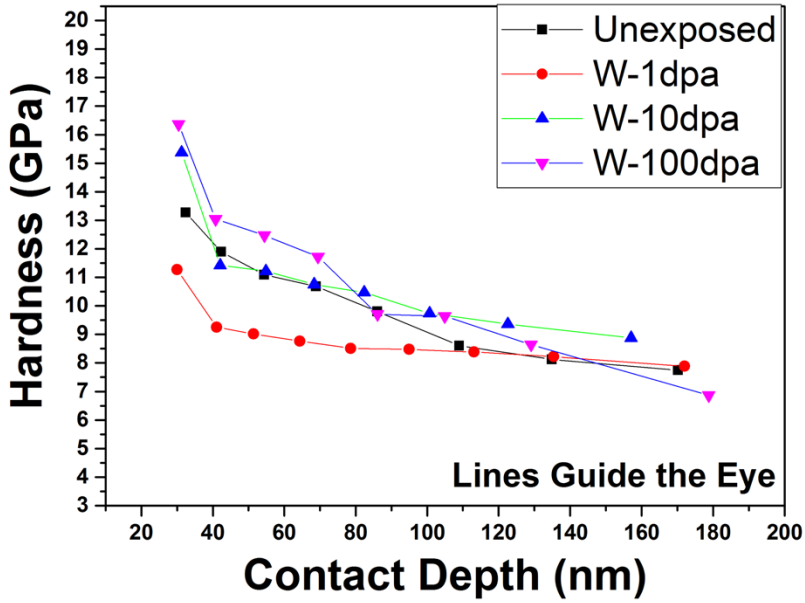

Figure 2.11: Nanoindentation hardness of pure W before (unexposed) and after (1, 10, 100 dpa) exposure to 3.5 MeV W^{2+} implantation. The increase in hardening after high dose is attributed to defect creation in the sub-surface.

The increase in hardening is attributed to point defect creation in the sub-surface that results in hardening as defects prevent dislocation motion. Therefore, it is clear that defects are introduced into the sub-surface that affect the mechanical properties and can affect the PMI properties. Therefore, these defects can be used to contrast the impact of irradiation-induced point defects in the W matrix on D/He behavior as compared to the dispersoids in the W matrix.

Oak Ridge National Laboratory

A furnace at Oak Ridge National Laboratory was used to anneal specimens for 1 hr. at various temperatures. The furnace is an W-element furnace operated under a flowing argon state. An argon pressure of ~50 mTorr was established during the annealing after purging the system three times to mTorr background gas levels. The ramp rate was 20 C/min to the desired temperature and subsequent quenches performed for one hour. The temperature was monitored with a Type C thermocouple positioned ~3" above the specimens.

Sandia National Laboratories Furnace

The furnace used to anneal samples for 2-30 hrs. at 1300 C was an effusion cell at Sandia National Laboratories at Livermore. A Veeco High Temperature Effusion Cell was used to heat samples in a UHV environment (base pressure of ~10^{-9} Torr). Samples were placed in a 6 cm^3 alumina crucible and separated with alumina spacers. Utilizing a W crucible, samples were heated to 1300 C. Tantalum shielding is utilized surrounding the cell to reduce radiative losses.

FZ-Julich Facilities

High heat flux (HHF) exposure tests were performed at FZ-Julich in Julich, Germany. All samples were cut into 12x12x4mm^3 prisms and polished to a mirror finish before exposures. High heat flux only exposures were performed using a Nd:YAG laser (1064 nm) with a beam diameter of 2mm and a box profile beam shape [12]. Exposures were broken down into four distinct regions on each sample surface, as shown in Fig. 2.12.

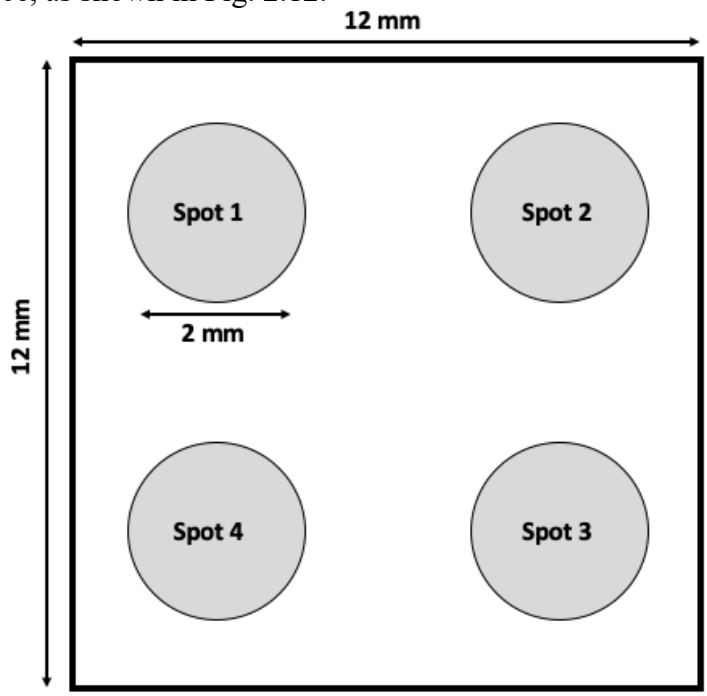

Figure 2.12: Schematic for laser exposures on samples for HHF-only testing. Only for representative purposes, not to scale. The sample was held at a constant temperature and the spots represent different laser pulsing conditions (different power and pulse numbers).

University of Huddersfield Facilities

In-situ He ion irradiations in the TEM were performed at the University of Huddersfield, utilizing the MIAMI facility (Microscope and Ion Accelerator for Materials Investigation). This facility utilizes a tandem accelerator attached to a 300 kV Hitachi H-9500 TEM, a 350 kV National Electrostatics Corporation (NEC) ion accelerator and a 20 kV Colutron G-2 ion gun to investigate ion bombardment within a TEM. In this study, the Colutron ion source was used to bombard W-5TaC samples with 2 keV He ions at a flux of $1x10^{18}$ $m^{-2}s^{-1}$ at 950ºC using a TEM heating holder. Figure 2.13a shows the MIAMI facility showing the ion beams and TEM, while Figure 2.13b shows the ion beam in relation to the TEM electron beam, showing co-incidence on the sample.

Analysis Facilities Utilized

Frederick Seitz Materials Research Laboratory

Much of the analysis of specimens was carried out at the Frederick Seitz Materials Research Laboratory at the University of Illinois. The following tools have been and will be utilized.

For Scanning Electron Microscopy (SEM), a JEOL 7000F Analytical SEM was used, complete with backscatter, secondary electron imaging and energy dispersion of X-Ray (EDS) capabilities. An SEM accelerates electrons to 5-30 keV incident on a specimen and rastered across the surface of interest. When interacting with the surface, secondary and back-scattered electrons are generated. These electrons are collected and used to generate an image of the specimen surface. Focused Ion Beams were used for cross-sectional imaging and TEM sample preparation. An FEI Helios 600i DualBeam SEM/FIB and Thermo Scios 2 DualBeam SEM/FIB were used for FIB analysis with a gallium ion beam. A FIB utilizes a Ga^+ ion beam to mill the surface of a specimen to access the sub-surface. The system has a Pt injection system and probe for manipulation of micro-scale specimens. Electron Backscatter Diffraction was performed on the JEOL 7000F using a HKL Technology EBSD System, as well as on the Scios 2 FIB with the EDAX TEAM EBSD analysis software utilizing a Hikari Super EBSD detector. EBSD is an electron microscopy technique utilizing the backscattered electrons off the specimen surface that exit at the Bragg angle and diffract to form Kikuchi bands. The patterns are indexed by computer software to match the underlying crystal grain orientation of the grain on the surface of the specimen. This technique can be used to map the grain structure, phase, and orientation of crystalline materials.

Transmission Electron Microscopy (TEM) was performed using a JEOL 2010 LaB_6 TEM operated at 200 kV. Over- and under-focusing was used to identify He bubbles. A TEM accelerates electrons to 200 keV which allows electrons to pass through a thin (<100nm thick) specimen, after which they are imaged on a screen to provide information about the fine microstructure of the specimen. Additionally, a FEI Themis Z Advanced Probe Aberration Corrected Analytical TEM/STEM operating at 300 kV was used for Scanning Transmission Electron Microscopy (STEM) investigations using the High Angular Annular Dark Field (HAADF) detector. STEM-EDS was performed with this instrument using the FEI Super-X, 4-crystal EDS detection system. A STEM is similar to a TEM, except the electron beam is focused to a point and the beam rastered across the TEM specimen. Electrons pass through the specimen and collected by detectors. The

HAADF detector collects only electrons that are scattered to high angles, providing the best Z-contrast imaging conditions. STEM-EDS uses the x-rays generated by the incident electron beam to map the composition of the TEM specimen. TEM sample prep was primarily done using the FIB to allow for site-specific analysis. However, TEM analysis of W fuzz tendrils was performed by scraping tendrils off the surface of the irradiated samples and collecting them onto a methanol-soaked lacey carbon support grid.

Optical microscopy was performed using a Keyence VK-X1000 3D Laser Scanning Confocal Microscope, using a 405 nm laser to map specimen surfaces. Surface roughness calculations were carried out with laser confocal microscopy using this instrument.

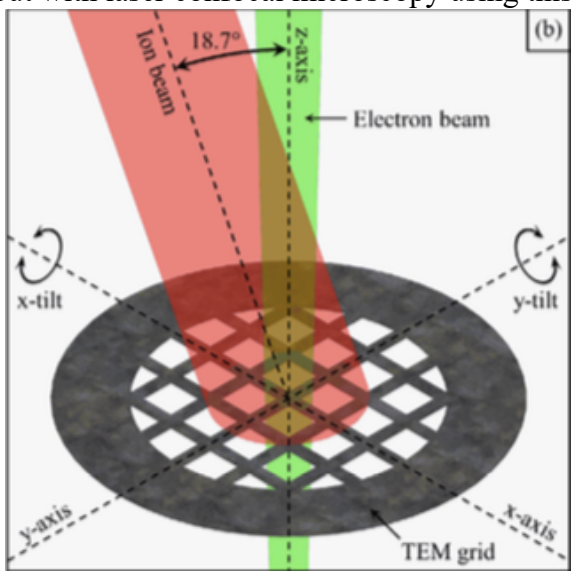

Figure 2.13: Schematic of the MIAMI-2 *in-situ* TEM facility at University of Huddersfield and the schematic of the electron and ion beams on TEM specimens [14, 15].

Vickers Hardness tests were performed on specimens after polishing. A Leitz Wetzlar microhardness tester with a diamond tip was used. A 200g was applied for 25 seconds to all specimens before measuring the diagonal lengths of the indent. Fifteen indents at random locations on the specimens were performed. The equation below was used to calculate the hardness (in Vickers Hardness value).

$$HV = 1854.4 * \frac{Load}{d^2}$$

In Equation 6, d is the length of the diagonal created in the sample after indenting with a Vickers tip.

Micropillar compression tests were carried out on 5wt.% samples dispersion strengthened W samples (W-5TaC, W-5TiC, and W-5ZrC) as well as a pure W control. Micropillars were fabricated via FIB milling utilizing a 6-step annular milling process shown in Table 1. 30 keV Ga^+ ions were utilized for all milling steps, progressively decreasing from a 9.3nA to a 0.79nA ion current to shape the micropillars with a 2µm diameter, 5µm tall pillar. At least eight pillars were fabricated in each sample.

The final dimensions of pillars were 6 μm in height and 2 μm in diameter. Figure 2.14 shows an as-fabricated pillar on the W-5TiC specimen.

Pillars were subsequently compressed inside an FEI Helios NanoLab 600i DualBeam FIB/SEM using a Hysitron PI-85 nanoindenter. Compressions were performed in constant displacement mode with a 6 nm/s loading rate. Up to seven compressions were performed on each pillar until the pillar failed. At least 3 pillars were tested in the as-fabricated state on each sample.

After fabrication of pillars and compression of as-fabricated pillars, an NEC Pelletron Accelerator was used for 2 MeV He implantation. The penetration depth and damage profile of He in pure W calculated via SRIM simulations is given in Fig. 2.15 [16]. After He implantation, the 4 remaining uncompressed pillars were tested using the same testing procedure as the unimplanted, as-fabricated pillars.

Table 2.1: FIB Milling procedure utilized to shape micropillars.

Current (pA)	**Outer diameter (μm)**	**Inner diameter (μm)**	**Depth (μm)**
9300	25	5	8
790	6	3	5
790	4	3	4
80	3	2.2	4
80	2.6	2.2	1
80	2.4	2.2	5

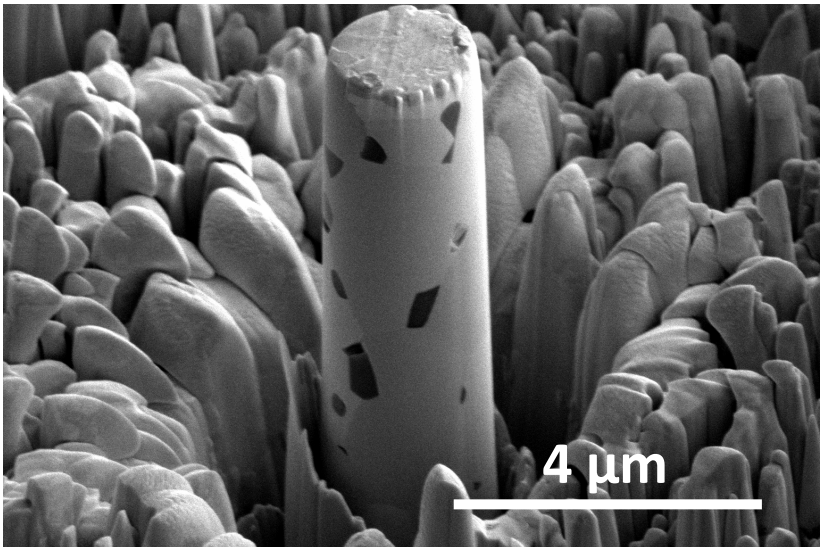

Figure 2.14: Pillar in the W-5TiC specimen using FIB-milling procedures.

In this work, measurements were carried out at the Cambridge Laboratory for Accelerator Study of Surfaces (CLASS), a 1.7 MV accelerator at MIT [17, 18].

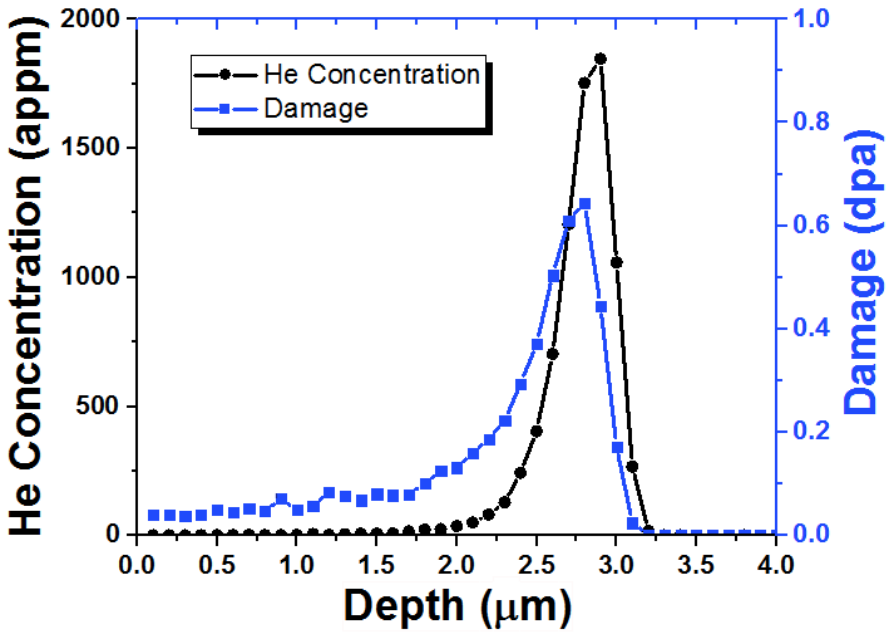

Figure 2.15: Helium depth profile and damage profile from 2 MeV He^+ into W calculated via SRIM [14].

Elastic Recoil Detection (ERD) will be used to examine the D and He depth profiles in DS-W materials. ERD is an ion beam analysis technique for measuring low-Z elements in materials, commonly used to depth profile H, D, and He. In ERD, forward scattering events of incident ions by light elements in the material are recorded by detectors. The incident ions are heavier than the element being detected and the ions are incident on the surface at 75 degrees (grazing incidence) and light atoms are ejected from the surface. In an ERD spectrum, the position from edge represents the species present, the width of the peak represents the atom layer distribution. Due to the geometry and high Z nature of probing beam, the information depth of ERD is hundreds of nanometers.

In this work, ERD will be performed with 8.9 MeV ^{16}O beam directed at 75-degrees incident on the surface to probe the depth of D and He atoms in DS-W materials. Forward scattered oxygen ions are detected at a 30 degree scattering angle and an aluminum foil is used to attenuate the scattered ions.

In addition to ERD, Nuclear Reaction Analysis (NRA) will be performed to provide a depth profile of D content microns beneath the specimen surface in DS-W materials. NRA of fusion materials uses high energy ^3He ions incident on a sample to induce nuclear reactions with elements in the subsurface, and the products of the reactions are detected by detectors as they exit the sample. Typically, a ^3He beam incident on a D-loaded W specimen exploits the $^3He(d,p^+)\alpha$ reaction, and either the p^+ (energy of 12 MeV) or α (energy of 3 MeV) particle can be detected.

Using this technique, deuterium depth profiles in W can be performed up to 7 μm beneath the surface. In this work 1.8 MeV ^{3}He was used to probe specimen. For both ERD and NRA, the SimNRA software was used for analysis of spectra [19].

Idaho National Laboratory

For analysis of D-irradiated samples, Glow discharge optical emission spectroscopy (GD-OES) was utilized to provide a surface depth profiling. GD-OES was performed at Idaho National Laboratory using a Horiba Profiler 2 GD-OES device. The system utilizes an Ar plasma operated at 700 Pa and 40 W RF power to sputter the surface of the irradiated specimens. After 450 s exposure to the Ar plasma ~45 μm of material was eroded in a 4mm diameter crater. The depth of the crater was measured by a differential interferometer profiler that measures the real-time depth of the crater during the sputter process.

The sputtered sample material becomes immersed in the Ar plasma and the sputtered atoms undergo an excitation-de-excitation process and emit light. The light emitted by all of the sputtered elements passes through a diffraction grating to photomultiplier tubes that collect the intensity of designated wavelengths.

Idaho National Laboratory facilities were also used to investigate helium retention and release via Thermal Desorption Spectroscopy (TDS). The TDS setup uses an infrared tube furnace to heat samples at a linear ramp rate of 1 K/s to 1373K. The sample temperature was monitored via a K-type thermocouple placed directly on top of the sample surface. A quadrupole mass spectrometer (MKS e-Vision) was used to track the He release (mass 4). Prior to experiments, the TDS system was calibrated using standard leak elements.

Dispersion-Strengthened Tungsten Sample Fabrication and Tungsten Control Samples

Fabrication of Dispersion-Strengthened Tungsten at UIUC

The samples used in this study are dispersion-strengthened tungsten materials fabricated via spark plasma sintering. Spark plasma sintering is a powder metallurgy process. The starting powders were sub-micron, high purity W, ZrC, TiC, and TaC powders with average sizes of 500 nm, 40-60 nm, 80-100 nm, and 1 μm, respectively. Prior to sintering, powders were weighed in the desired weight fractions and milled together using yttria-stabilized zirconia media.

Spark plasma sintering was performed with a Dr. Sinter SPS-615 device manufactured by Fuij Electronic Industrial Co. Powders are loaded into a high-strength carbon die and punch before being placed into the SPS machine. The die is 21.4mm in diameter and multiple layers of graphite foil were placed between the die and the powders and punches (20mm diameter). Powders were sintered under an Ar atmosphere following multiple atmospheric purging steps. Specimens were sintered at 1800ºC and 60 MPa pressure, with a 100ºC/min ramping rate and a 4-minute hold at 1800ºC. The device uses a 12:2 on:off pulse to provide a DC current for joule heating. Prior to

sintering, multiple Ar purges were performed. The temperature is monitored via optical pyrometer positioned to measure the temperature through an orifice in the die. Consolidated specimens are ~4mm in height and ~20mm in diameter and are cut to desired dimensions using wire electric discharge machining (EDM) methods [20].

Control samples

Multiple control samples were used in the various studies to compare to the behavior of the dispersion-strengthened W samples.

ITER-grade tungsten is a special type of pure W material that is fabricated to have a microstructure benefitting performance in a fusion reactor. ITER-grade W has elongated grains perpendicular to the surface. It is a rolled, sintered, and forged product that undergoes a post-fabrication hot rolling process to develop an anisotropic microstructure consisting of elongated grains perpendicular to the surface, resulting in an average grain size of 1-3µm and 5µm long [21]. The elongated grain structure is accordance with ITER specifications to have grain orientation parallel to the heat flow direction to potentially mitigate delamination [22]. In this work, ITER-grade W samples were purchased from Sumitomo Electric Corp. A cross-sectional micrograph of the grain structure of the ITER-grade W is shown in Fig. 2.16. In the rest of this document, ITER-grade W samples are referred to as "IGW." In addition, pure W samples with carbide dispersoids were fabricated via spark plasma sintering at UIUC using the same sintering parameters.

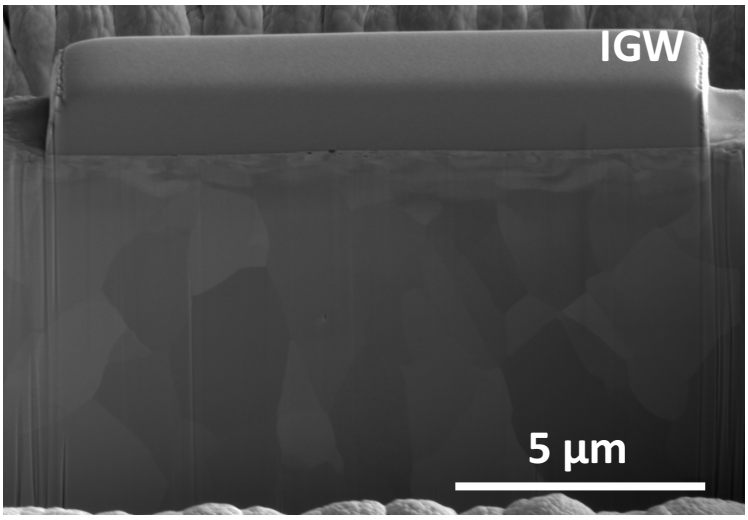

Figure 2.16: FIB cross-section SEM micrograph showing microstructure of W grains in ITER-grade W (IGW) sample.

References

[1] *Product Manual: Multicentre Operating Guide XLT-11991-002.* UHV Design Ltd., East Sussex, England.
[2] "Tectra: Plasma Sources." http://tectra.de/deposition-progress/plasma-sources/. Tectra, 2017.
[3] *Tectra Gen II Plasma Source Operating Manual*. Tectra. Frankfurt, Germany. 2012.
[4] *eH 400 Ion Source Manual: Filament Cathode Version, Version A.* Kaufman and Robinson,

Inc. Fort Collins, CO, USA. 2013.
[5] *Specs User Manual: PHOIBOS EP – Elevated Pressure Hemispherical Energy Analyzer*, Version 1.0. SPECS Surface Nano Analysis GmbH. Berlin, Germany. 2014.
[6] *Specs User Manual: XR-50 X-Ray Source*, Version 3.1. SPECS Surface Nano Analysis GmbH. Berlin, Germany. 2016.
[7] E. Lang, et al. *Fusion Science and Technology.* **75** (2019) 533-541.
[8] J.P. Allain. *Kinematic and Thermodynamic Effects on Liquid Lithium Sputtering.* PhD Dissertation, University of Illinois, 2001.
[9] G. De Temmerman et al. *Fusion Engineering and Design* **88** (2013) 483–487.
[10] H.J.N. van Ecka, et al. *Fusion Engineering and Design* **89** (2014) 2150–2154.
[11] B. Heidrich et al. *Nuclear Inst. and Methods in Physics Research B* **441** (2019) 41–45
[12] M. Wirtz et al. *Journal of Nuclear Materials* **438** (2013) S833–S836.
[13] C. Linsmeier, et al. *Nucl. Fusion* **57** (2017) 092012.
[14] J.A. Hinks, et al. *Journal of Vacuum Science & Technology A* **29**, 021003 (2011); doi: 10.1116/1.3543707.
[15] G. Greaves, A.H. Mir, R.W. Harrison et al. *Nuclear Inst. and Methods in Physics Research, A* **931** (2019) 37–43.
[16] http://srim.org, SRIM.

[17] G.M. Wright, et al. *Review of Scientific Instruments* **85**, 023503 (2014).
[18] K. Woller, et al. *Journal of Nuclear Materials* **463** (2015) 289-293.
[19] M. Mayer. *SIMNRA User's Guide,* Report IPP 9/113 Max-Planck-Institut für Plasmaphysik, Garching, Germany (1997).
[20] E. Lang. *Synthesis, characterization, and properties of carbide dispersion- strengthened tungsten alloys for use as a plasma-facing material in nuclear fusion reactor*s. University of Illinois, Master's Thesis, 2017.
[21] V.Kh. Alimov, et al. *Journal of Nuclear Materials* **420** (2012) 370–373.
[22] G Kalinin, et al. *Fusion Engineering and Design* **55** (2001) 231–246.

CHAPTER 6: CONCLUSIONS

This work set out to continue to the work of advanced tungsten materials for use as plasma-facing components in fusion reactors, by expanding the scope to dispersion-strengthened tungsten. Through experimentation and analysis, examinations of the synthesis of dispersion-strengthened tungsten through spark plasma sintering, the effects of the dispersoids on the microstructure, and the subsequent effects of the altered microstructures on the thermal, mechanical, and irradiation properties. Specifically, this work sought to address the following questions:

1. Does the addition of dispersoids limit recrystallization by preventing W grain growth?
2. Is cracking and failure impacted by the presence of dispersoids?
3. Is there enhanced sputtering of dispersion-strengthened tungsten given the introduction of non-W elements?
4. Does the introduction of dispersoids trap deuterium and impede deuterium diffusion?
5. Can the dispersoids sequester helium into many small bubbles to prevent large bubble formation and effectively manage the helium inventory?

From these guiding questions, the following hypotheses were proposed:

4. Impact of dispersoids on thermo-mechanical properties
    a. Addition of a 1.1wt.% dispersoids effectively pins W grains, limiting recrystallization. However, the W-W and W-dispersoid interfaces are not immune to cracking under loading.
5. Deuterium trapping
    a. Deuterium trapping will be increased due to the presence of dispersoids.
6. Helium behavior
    a. The dispersoids trap He in small clusters, limiting He bubble formation in the W matrix.
    b. At low dispersoid concentrations, the near-surface behavior mirrors that of pure W.

Each of these hypotheses have been examined in the previous chapters. Here, the conclusions of each chapter are presented, the ability to answer the proposed hypotheses addressed, and the impact of DS-W development and progress is discussed in the context of fusion PFC research.

Conclusions

Microstructure, Mechanical Properties, and Recrystallization Behavior

The addition of all types of dispersoids (TiC, TaC, ZrC) alter the W microstructure by refining the W grain size and resulting in the presence of second phase dispersoids. These dispersoids primarily exist at grain boundaries, although in some samples, exist within W grains. The dispersoids have their desired effect of capturing impurity oxygen atoms in the W matrix during fabrication, purifying the W grain boundaries and resulting in the formation of mixed metal-oxy-carbide dispersoids This is the desired impact of the dispersoids on the W microstructure.

The dispersoids are able to limit recrystallization and grain growth during annealing. The specific temperature of recrystallizing depends on the sample composition, but all dispersoid types increase this temperature above that of pure W (~1200 C in this study). Under long-time annealing, the kinetics of recrystallization and recovery are slowed as compared to pure W, indicating that the dispersoids are able to pin W grains and prevent grain growth. Low concentrations of dispersoids are most effective at limiting this grain growth and also do not have the development of potentially detrimental surface oxides that appear on the 10wt.% samples.

Micropillar compression experiments investigate the mechanical properties in the near-surface region, in a similar interaction volume that will be subject to ion, neutron, and heat flux exposure during use as a plasma-facing material in a fusion reactor. catastrophic failure is observed at W-TaC and W-ZrC interfaces, indicative of poor cohesion. W-TiC pillars with a high fraction of TiC dispersoids do not fail and behave similarly to pure W. From this work, it is clear that an even distribution of fine dispersoids is necessary to a) accurately sample the material volume in order to ensure the pillar compression mirrors the bulk testing, and b) enhance the mechanical properties to limit the stress concentrations that may occur at large W-dispersoid interfaces.

An even distribution of fine dispersoids may improve performance under high heat flux loading, as an even distribution of dispersoids may limit the stresses that would accumulate at any one interface. This may limit cracking that would occur.

It was hypothesized that a 1.1wt.% addition of second phase particles will effectively pin W grains and inhibit recrystallization. This is supported by the annealing experiments indicating a higher recrystallization temperature and delayed grain growth kinetics as compared to pure W. It was also proposed that cracking will occur at the W-dispersoid interfaces, if the load is sufficiently high. This is supported by micropillar compression experiments showing cracking at W-dispersoid interfaces, if the load is concentrated on that interface. Therefore, there is a need to increase the number of interfaces to distribute the load evenly.

This work shows that dispersion-strengthened tungsten PFCs have a significantly larger temperature operating window in a fusion reactor than pure W. Additionally, the component lifetimes can be significantly extended through microalloying as the stable microstructures under high temperature loading will portend stable material properties. This is a significant development, indicating that the mechanical and microstructural stability of DS-W materials can be relied upon for predictable and stable properties in a fusion environment, and can effectively be employed in a fusion reactor at operating temperatures without worry of microstructure degradation. This work significantly advances DS-W development and research for a fusion PFC application and can effectively guide future fabrication and research directions. The long-time effects of high temperature exposure, combined with mechanical stresses, must be studied to investigate reactor-relevant structural loading conditions on the failure and microstructural stability.

Deuterium Effects

The dispersoid microstructure has a significant impact on the deuterium transport and distribution in DS-W materials. The addition of any dispersoids to the microstructure increases the amount of D retained at all depths, compared to pure W. The dispersoids alter the specimen chemistry and offer D trapping sites, trap sites which are estimated to be stronger than other material defects, such as vacancies. The dispersoids affect the oxygen distribution in the bulk material, allowing enhanced D diffusion along W grain boundaries. Strengthening with TaC leads to the highest D concentrations at all depths, in both low and high fluence studies. W-ZrC samples have lower D concentrations than W-TaC after high fluence irradiation. Grain size effects between these two samples are not thought to play a large role, therefore the difference in the D concentrations are attributed to chemistry differences between Ta and Zr. Under low fluence irradiation, W-TiC samples consistently have the lowest D concentrations, attributed to the presence of fine TiC dispersoids, some of which are within W grains which can trap D atoms before getting to grain boundaries. Finally, the DS-W materials still develop surface blistering, indicating that D atoms can still accumulate into bubbles and are not completely trapped at dispersoids. Further studies are needed, however, to systematically understand the blistering behavior.

A high concentration of small dispersoids will provide a high number of traps while simultaneously purifying the W grain boundaries, that could allow for enhanced diffusion. If the wt.% is low, then D diffusion could be enhanced into the bulk. If the wt.% is high, then D diffusion could be limited by trapping at the dispersoids. These results show that the TaC dispersoids may want to be avoided if D diffusion and retention must be mitigated.

It was hypothesized that deuterium trapping will be enhanced in the presence of the second phase dispersoids. This is supported through low and high fluence D irradiations showing that DS-W materials have higher D concentrations throughout a variety of sub-surface depth profiling investigations, as compared to pure W. Additionally, compared to pre-damaged W with a high number density of point defects, DS-W materials still have higher D concentrations in the near-surface, indicating that the second phase dispersoids are stronger D traps than other defects in W. Finally, surface nanostructuring after D irradiation supports that D trapping is occurring, as the density of D-induced blisters correlates with the dispersoid density.

This work represents the first work comparing the depth distributions of D in DS-W compared to pre-damaged W under reactor-relevant D irradiation conditions. Multiscale D depth investigations indicate that microalloying of W may enhance the D inventory in fusion PFCs. This is a significant result indicating that DS-W materials may have a potential drawback compared to pure W as high D concentrations can be a fueling and safety concern. Further work is needed, however, to understand how the D is trapped within the DS-W microstructure, as the increased D concentration may not be a long-term issue if it can be thermally released at reactor operating temperatures. Therefore, these results show that despite the promise of DS-W materials to have many enhanced PMI properties compared to pure W, excessive D retention may by a limiting factor limiting the extent of alloying allowed to force there to be a balance in the alloying type and concentration to improve the overall PFC performance, despite having decreased performance in one material metric.

Helium Effects

Incident He ions on a DS-W surface can have multi-scale effects, depending on the ion energy, fluence, and sample temperature. High energy bombardment can lead to surface sputtering, but the sputtering yields are not enhanced compared to pure W. Experimentally, no preferential sputtering is observed, but higher fluence simulations indicate that the surface chemistry may change at higher fluences, resulting in W surface enrichment. These results show that sputtering yields should not be the deciding factor in dispersoid material selection. However, to potentially avoid significant changes in surface composition at high fluences, the 1.1wt.% samples may be preferred over 10wt.% samples.

When the irradiation temperature is increased and ion energy lowered, incident He ions can be trapped in the W matrix and form sub-surface bubbles and surface nanostructures. At low fluence, the dispersoids develop nanostructuring dependent on the dispersoid type, with TaC dispersoids developing no nanostructuring and TiC dispersoids developing tendril-like nanofeatures at lowest fluences. No concentration or type of dispersoid prevents nanostructuring on W grains, while a high concentration of TaC and ZrC dispersoids can limit the total overall surface area that develops nanostructuring.

The subsurface dispersoids do not appear to preferentially trap He in TEM-visible He bubbles, although the dispersoid microstructure does limit the thickness of He-induced fuzz growth. *In-situ* TEM experiments show no He bubble formation within dispersoids while W grains develop bubbles. This is attributed to the trapping of small He bubbles within the dispersoids, preventing accumulation, due to the mixed metal-oxy-carbide composition of the dispersoids. The

nanostructures that form appear to be stable under high heat flux loading, and are slightly enhanced in non-W elements compared to the bulk matrix.

Retention and thermal release of He is governed primarily by the concentration of dispersoids, and the type of dispersoid has minimal impact. Additions of 10wt.% traps more He in higher energy trap sites, preventing He release at low temperatures, while additions of 1.1wt.% slightly shifts desorption to higher temperatures, but does not significantly affect total He desorption compared to pure W. To ensure He concentrations do not build up in the microstructure that could affect D retention and mechanical properties, He must be desorbed at reactor-relevant temperatures. Therefore, a low concentration of dispersoids is preferred over a high concentration of dispersoids.

Implanted He in the matrix is not observed to impact the W-TiC mechanical properties under micropillar compression experiments. This may be due to the high concentration of dispersoids limiting large He bubble formation within the W grains which could detrimentally affect the mechanical properties. Thus the TiC-dispersoid microstructure may limit He-induced hardening compared to pure W. However, the limited testing and irradiation conditions indicate that no clear conclusions can be drawn. Additionally, if dispersoids act as trapping sites, results show that a high concentration of dispersoids would limit He concentrations at any one interface. Significant He accumulation at an interface may limit the future effectiveness of the interface to trap He and affect the interfacial strength, detrimentally impacting mechanical properties. Thus, a high number density of small dispersoids is preferred over large dispersoids.

It was hypothesized that He interactions with the surface of DS-W materials will mirror He interactions with pure W, but enhanced erosion of the dispersoid particles will occur. Sputtering investigations showed that the DS-W materials do not have enhanced sputtering under He bombardment. Additionally, the surface composition is stable, indicating no preferential sputtering under ion bombardment. This important result shows that DS-W materials may not have significant sputter emission of impurities into the plasma in a fusion reactor and DS-W materials can be chosen for other material properties without affecting the sputtering properties.

It was hypothesized that the second phase dispersoids will trap He and limit He accumulation in the W matrix to help suppress He bubble formation. No direct evidence of He sequestration in the W matrix is observed, however significant indirect evidence for the effect of the dispersoids on the He dynamics have been presented. Helium bubbles are observed within W grains, but not at W-W grain boundaries or W-dispersoid interfaces. The thickness of He-induced nanostructured fuzz layer is decreased, indicating that He bubble nucleation, agglomeration, and diffusion are limited by the presence of dispersoids. This is supported by the dispersoids having different nanostructuring response (decreased in size and density) and decreased He desorption at high temperatures. *In-situ* TEM irradiations show the development of He bubbles within W grains, but not within dispersoids, indicating that the composition of dispersoids limits He bubble formation within the dispersoids and at their interfaces. While no direct evidence shows He trapping at dispersoids, the differences in nanostructuring and desorption shows that the dispersoids have an impact on the subsurface He behavior. Therefore, the inclusion of the dispersoids improves the radiation resistance of W without the detrimental effects of significant grain boundary segregation of He bubbles experienced by nanocrystalline W.

This represents a significant improvement in W PFC development, as the ability to sequester He and limit He bubble and He-induced nanostructuring growth can prolong W PFC lifetimes and improve performance. In a similar manner to nanocrystalline W, DS-W materials exhibit greater resistance to fuzz formation to higher He fluences. However, the DS-W materials

are thermally stable and also present no detrimental He bubble accumulation at W grain boundaries. These significant results show that microalloying W may be an effective path towards developing radiation-tolerant W-based materials for fusion PFCs.

Significance and Implications in Driving Fusion Materials Development

This work has shown the promise of dispersion-strengthened W materials. The materials investigated here provide an avenue towards future materials development: promising material compositions and processing schema have been identified. Multiscale investigations of the material performance in fusion reactor-relevant environmental conditions have identified how DS-W improves upon pure W, which can guide future material design and inform future experiments. These results show the promise is DS-W materials to address the concerns of pure W in a fusion environment, and urge the continued study of advanced W materials for PFC applications.

Through investigations of mechanical properties (recrystallization behavior), deuterium irradiation (cumulative D retention), and helium irradiation (sputtering yields, He desorption), quantitative measures of the impacts of dispersoids can be determined. To quantify the impacts of the dispersoids, the % change of hardness after annealing at 1800 C, the cumulative D content in the first 3µm beneath the surface, the He-induced sputtering yields, and the total He desorption amount can be summarized. We wish to transform these quantities to a 0 to 1 scale, where 1 is better. For recrystallization inhibition, a lower change in hardness is desired, so the inverse of the % change is used. For cumulative D retention, a lower He concentration is desirable, so the inverse is taken. For sputtering yield, a lower yield is better, so the inverse of the sputtering yield is used. Finally, for He desorption, a greater amount of He desorption is desirable so no inverse is required. To put all quantities in each category on the same scale, each quantity is divided by the maximum in each category to normalize all quantities on a 0 to 1 scale. The quantities broken down as a function of composition can be displayed in the radar chart in Fig. 6.1.

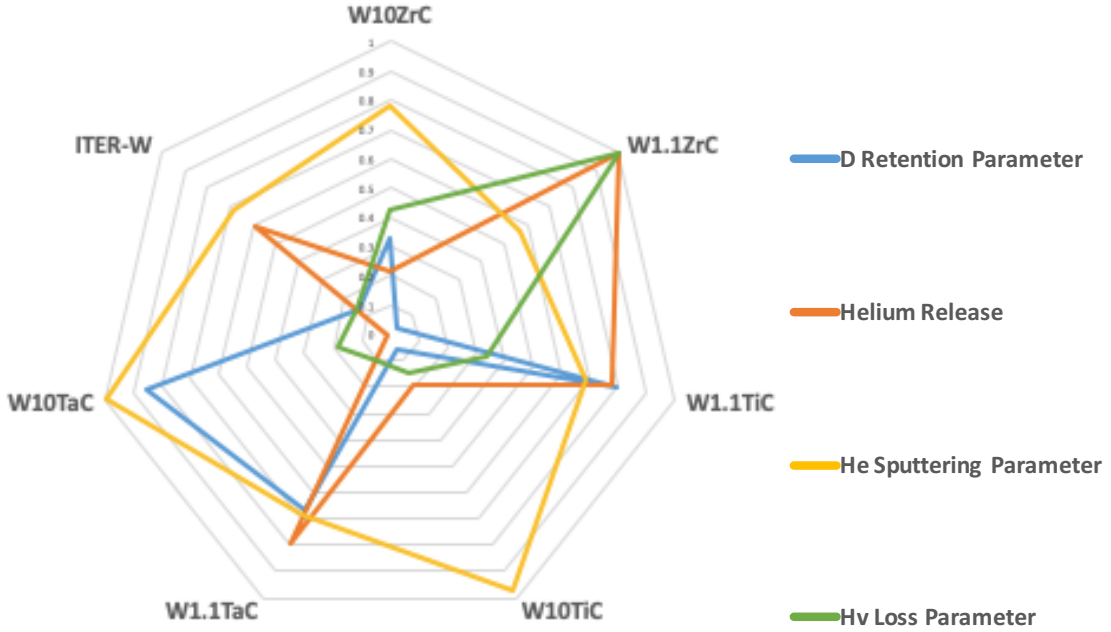

Figure 6.1: Radar chart of relevant quantitative measures of material properties. A value of 1 indicates the best performance, showing that the 1.1wt.% samples have the best combinations of qualities that enhance material performance.

The average score of each material composition can be calculated, and the highest score (closest to 1.0) represent the material composition that best balances all properties that are relevant for use in a fusion reactor and has the most promise for use a plasma-facing material. These scores show that the W-1.1TiC and W-1.1ZrC materials have the best balance of properties and should be investigated further. The 10wt.% materials have a worse combination of properties, on average, with an overall average score similar to that of pure W, indicating no significant overall improvement in the material properties. Thus, in balancing the irradiation and thermo-mechanical properties, DS-W specimens with low weight fractions of an added second phase, but with a high concentration of dispersoids, improves most upon the properties of pure W to widen the temperature operating window and improve the radiation tolerance. This work motivates further experiments and study of processing of DS-W materials to fully evaluate their promise as PFCs in future fusion reactors.

The fusion community has indicated that while W is a promising material for fusion applications, there are some properties that a well-developed for use in a fusion environment, while others leave a lot to be desired. For example, sputtering, H/D interactions, and thermal properties are assumed to be sufficient for use as a PFC. However, the oxidation and mechanical properties of pure W need to be improved.

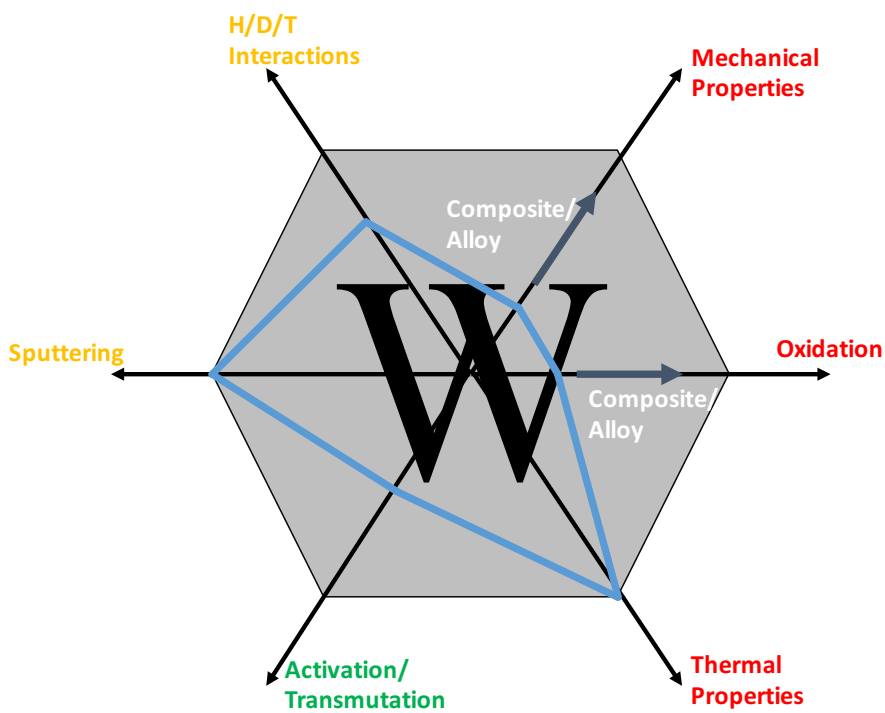

Figure 6.2: Radar chart of properties relevant in a fusion PFC environment and corresponding W performance.

Based on the schematic in Fig. 6.2, the DS-W materials should have similarly high performance as pure W, but should improve on the poor performance of pure W. Therefore, DS-W should have enhanced mechanical and oxidation performance. This work on DS-W materials shows that the sputtering properties are unchanged, but the D/H/T Interactions may be worse than pure W. The oxidation performance may be enhanced, as the second phase dispersoids become oxidized under high temperature exposure, but the W grains do not show evidence of oxidation. XPS investigations following high temperature annealing do not show the development of tungsten

oxides. The above schematic can be altered given the current work on DS-W. The purple lines show the DS-W materials while the blue still shows pure W.

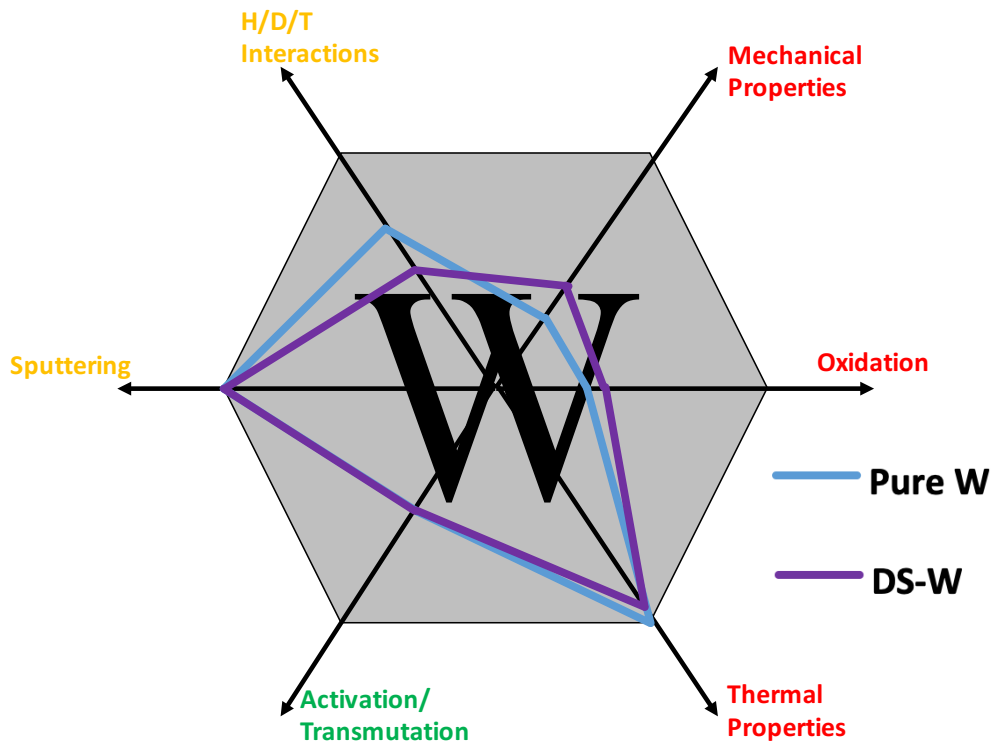

Figure 6.3: Schematic comparing DS-W properties to pure W. Current work has demonstrated an improvement in the mechanical properties, similar sputtering properties and thermal properties, but diminished H/D/T interaction performance.

The mechanics and thermal properties need to be further investigated, but this work has shown that the recrystallization properties can be improved through dispersion strengthening. The thermal properties can be tested through thermal conductivity testing. If the dispersoid fraction is large and if the dispersoids have a large size, then the thermal conductivity may be detrimentally affected. However, if the dispersoid fraction is small, then the material is primarily W and the thermal conductivity may be minimally affected. Oxidation resistance can be investigated with thermal gravitation analysis to ensure that volatile tungsten oxide does not form. It would be desirable to have the second phase elements segregate to the surface and oxidize preferentially over the W.

The focus of the research given the current and future capabilities of the group will focus on the plasma-material interaction properties, and less on the bulk properties. Therefore, with a focus on the PMI properties, a new radar chart can be formed to compare W and DS-W.

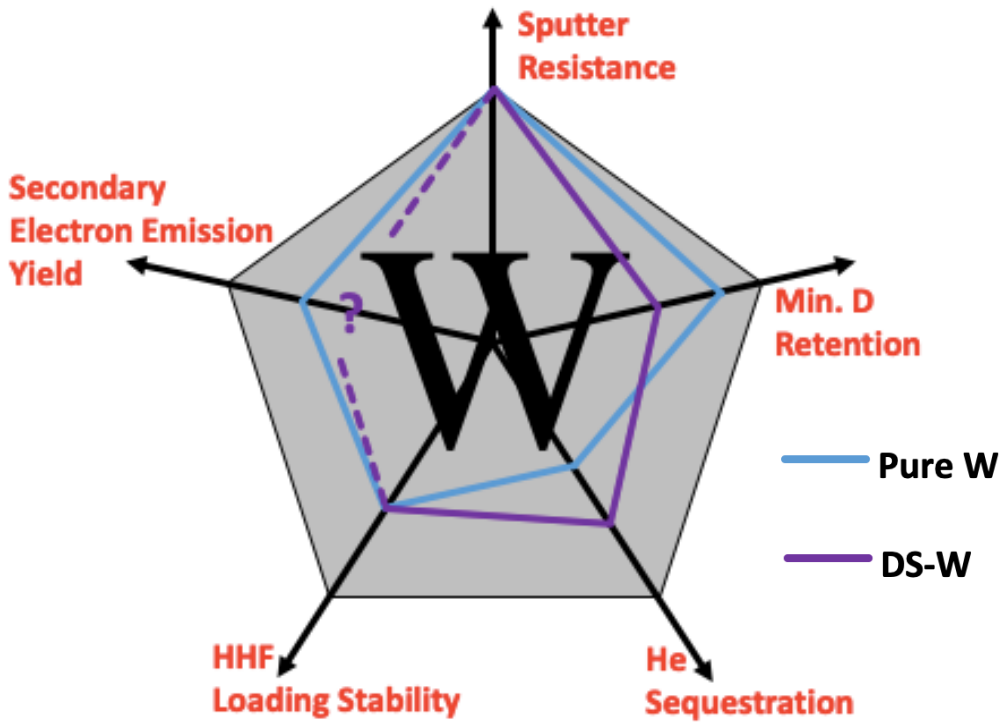

Figure 6.4: Radar chart comparison of the PMI properties of pure W to DS-W. The DS-W materials exceed pure W in sequestering He and limiting He nanostructuring. However, they increase the D retention. Pure W and DS-W have comparable sputtering yields and responses under high heat flux (HHF) loading, while the secondary electron emission yields of DS-W remain in question.

Focusing on PMI-relevant properties, we can examine how the DS-W materials, on average, perform relative to pure W. This work has shown that DS-W materials have higher D concentrations in the near-surface compared to pure W. Therefore, DS-W materials perform worse at minimizing D retention. However, the DS-W materials provide better He sequestration abilities compared to pure W, which can improve material performance in a He irradiation environment. Additionally, similar performance is observed between pure W and DS-W for sputter resistance and stability under high heat flux loading. Open questions remain regarding secondary electron emission and other PMI properties of DS-W materials, to be expanded upon in Chapter 7.

CHAPTER 7: FUTURE WORK

This work was born out of the work on nanocrystalline and ultra-fine grained tungsten that showed enhanced irradiation tolerance, but unstable properties at high temperatures. In order to maintain the microstructure while continuing to provide He irradiation resistance, the path of dispersing second phase particles within the tungsten matrix was explored. The research has now progressed to the point where significant conclusions on multiple material properties can be formed that can help guide future materials development and testing in this area.

This work has shown that the microstructure can be controlled via dispersoid addition, although the ability to control the size and distribution of dispersoids to increase the fraction of small, intra-granular dispersoids can be explored further. DS-W materials have shown to have enhanced recrystallization resistance, but the recovery, recrystallization, and recovery kinetics following fusion-relevant irradiation and the thermal shock performance of all specimens must be elucidated. Finally, the trapping of implanted fuel species must be further elucidated through multi-scale investigations of D/He interactions with DS-W.

Proposed Future Work

The DS-W materials were studied for use in a fusion reactor environment, an environment in which synergistic transient and quiescent heat and particle loads impact the material surface. Plasma-facing materials must tolerate these harsh conditions, to have their properties maintained during operation without drop in performance, while simultaneously not introducing impurities back to the core plasma to maintain fusion reactor performance. To qualify material performance for use a potential plasma-facing material in fusion reactors, there is a need to focus on testing of the plasma-material interactions (PMI) properties. These DS-W materials can be envisioned as a coating on a bulk, structural materials, such that the surface-relevant PMI properties are the properties of most interest for the DS-W materials. The bulk mechanical properties will be most influenced by the bulk material to which it is attached, while the DS-W coating will influence the bulk PFC performance. Before additional testing of PMI or bulk material properties can be performed, the DS-W specimen microstructure must be optimized through exploration of the material processing. Currently, the developed specimens are cm's in size, and the scalability of SPS to process potential PFC materials must be determined. The processing of powders and investigations of scalable fabrication technologies must be explored before DS-W can be economically deployed for use in a fusion reactor. Therefore, the material composition should be chosen based off of its PMI properties, and testing along these lines can most easily be continued in the RSSEL group. To drive this work, the following schematic is proposed to indicate the properties of interest and studies that should be undertaken to decipher material performance under these conditions.

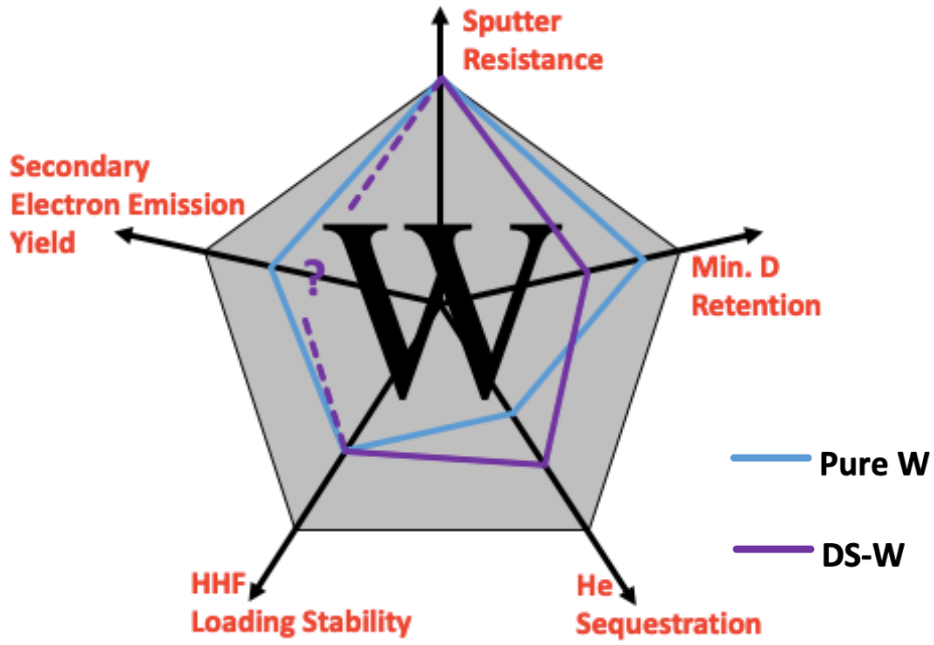

Figure 7.1: Radar chart schematic of PMI-centric properties showing relative DS-W performance compared to pure W.

This work has investigated 4 of the 5 proposed properties, but not in enough detail. Further work can be done to drive deeper understanding and qualification of material performance. The schematic above shows the relative scores of DS-W in general compared to pure W. This is attempted to be an aggregate of the DS-W material properties of all compositions to display the differences with pure W to show the progress that has been made and the areas for further investigation to motivate studying DS-W as an alternative PFC.

The five main PMI properties in Fig. 7.1 are identified as crucial for PFCs, some of which have been investigated in the current study. Sputtering is one main PMI property, as impurity introduction into the plasma though knock-on damage of surface atoms must be limited. This work has investigated physical sputtering of DS-W under controlled, ideal conditions. However, more realistic investigations would study chemical sputtering and sputter erosion under combined ion and heat loading. The DS-W material to be chosen would need to have a high sputtering resistance, and therefore a low yield. The presence of the dispersoids may alter the chemical sputtering yield, as pure W has a low chemical sputtering yield. Further testing is needed to understand the synergistic effects of heating and high energy impurity (C, O) bombardment on the surface chemistry and total sputtering yield of DS-W materials to truly gauge their sputter resistance.

The second parameter of interest is limitation of He bubble accumulation. While He bubble accumulation can lead to surface nanostructuring that may be detrimental to PMI performance, He bubble accumulation may also lead to a degradation of the near-surface mechanical properties. If enough sinks are present in the material (grain boundaries or dispersoids), then He bubble accumulation can be diminished and the growth of large bubbles and accumulation of bubbles at W-W grain boundaries can be mitigated. Further testing should focus on understanding the He sequestration performance of the dispersoids to clarify that they are trapping He and preventing large bubble formation and clustering at W-W grain boundaries to enhance material radiation tolerance.

The third parameter is deuterium retention. Deuterium retention must be minimized in PFCs to ensure safety and fuel inventory concerns. This has been studied via GD-OES methods on all DS-W materials and with NRA methods on select DS-W materials. However, establishing a reliable baseline and database for D retention in these materials may ultimately decide if DS-W materials are suitable for PFC use. Experiments with thermal desorption spectroscopy can be used to determine the total amount of retained deuterium, and their desorption pathways. Through analysis of the desorption peaks, the trapping sites of D in the DS-W matrix can be elucidated. Additional depth profile techniques for examining D concentrations must also be utilized. High Resolution Rutherford Backscatter Spectroscopy (within ~1 μm), Elastic Recoil Detection (within ~200 nm), and Direct Recoil Spectroscopy (within ~10 nm) can be used to examine the H/D concentration on various length scales of DS-W specimens to understand how the dispersoid addition affects D transport at the surface and near sub-surface.

The fourth parameter is stability under high heat flux loading. While no solid material can likely prevent damage under the high heat flux loading that will be present during off-normal events in a fusion reactor, the best materials will prevent melting and will limit cracking. The best material will limit the width and depth of cracking and will not have recrystallization under the loading. The current studies have shown that W-ZrC materials do not have significantly superior performance compared to pure W in limiting crack formation. However, the recrystallization studies have shown that under high heat exposure, recrystallization and grain growth can be limited. Therefore, there is a need to understand the response of DS-W materials under high heat flux loading to determine if the dispersoids can help maintain microstructural stability.

The fifth parameter is related to the secondary electron emission yield. Most edge plasma physics models have utilized a secondary electron emission yield for pure W. The secondary electron emission yield can alter the plasma dynamics near the surface, there is a need for computational simulations to use an accurate yield to accurately model plasma dynamics. Therefore, to provide the most appropriate material information for computation studies of the plasma performance in the presence of DS-W plasma-facing materials, the secondary electron emission yields must be understood. Since many prior computational studies have been performed on the plasma dynamics with pure W as the plasma-facing material and plasma confinement schemes have been identified to adapt to pure W as a PFC it would likely be desirable to have a DS-W material that has a secondary electron emission yield that is similar to that of W.

Material Development and Composition

The current work has indicated that the addition of 1.1wt.% second phase particles is most beneficial compared to pure W, 5wt.%, or 10wt.%. Therefore, future work should focus on the development and testing of 1.1wt.% materials. Having a high number fraction of small dispersoids is beneficial for mechanical and irradiation properties. Therefore, materials processing should focus produces materials with small (~100 nm diameter) dispersoids dispersed more evenly within a W matrix. A large number density of small dispersoids has been most favorable in ODS steels, as well. In ODS steels, the irradiation hardening can be suppressed if the dispersoid density is greater than 10^{24} m^{-3} [1], offering a sink strength of ~10^{16} m^{-2}, where the sink strength of an incoherent particle is defined as $Z = {3F_v}/{r^2}$ where F_v is the dispersoid volume fraction and r is the dispersoid radius [1,2]. In the materials studied in this work, the sink strength is a maximum of ~10^{13} m^{-2}. Therefore, there is a need to refine the dispersoids to have a high fraction of smaller particles in order to offer a strong defect sinks to combat radiation damage and specifically prevent large He bubble formation.

Numerous fabrication and processing techniques have been studied to produce these microstructures, achieved through advanced powder processing and post fabrication heat treatment and processing. The control of oxygen during the fabrication steps has been shown to be crucial for ODS microstructure fabrication. Post-processing annealing and thermo-mechanical treatments can further refine the microstructure. Therefore, to develop DS-W materials with finer dispersoids, post-fabrication processes such as rolling may reduce the dispersoid size. Additionally, ODS steels have benefitted from longer milling times of Y and Fe powders [2]. Therefore, through increasing the milling time, the size of dispersoids may be reduced. However, there is still a wide range of ODS particle sizes due to the variability in processing and fabrication.

Conversely, more advanced materials development techniques could be employed, such as 3-D printing processes, like selective laser melting (SLM), powder bead fusion melting (PBFM), or selective e-beam melting (SEBM). These methods utilize metal powders that flow over a surface and are simultaneously melted by a high powered laser or electron beam, and then re-solidified. Schematics of these processes are shown in Figure 7.2. The powders can either be deposited coaxially through a stream along with the laser beam, or laid out in a bed for the beam to pass over.

Additive manufacturing of W is difficult due to tungsten's high melting point, low DBTT, high thermal conductivity, and high surface tension [5]. Improvements have been made recently to increase the density and reduce the cracking. It has been shown that there is an important balance between powder particle shape, substrate temperature, laser power, oxygen gas concentration, and laser scanning parameters needed to effectively build W-based materials, and repeatability and densification remains an issue [4-11]. However, additive manufacturing can fabricate components rapidly and offers significantly greater geometric freedom [10]. However, the material properties can be anisotropic due to the build parameters [11]. Additive manufacturing techniques, while promising, are not yet viable for large-scale reliable production of W materials, as the processing results in specimens with lower densities, lower hardness, and larger grain sizes than conventionally processed W. There are significant un-answered questions about the effects of the processing parameters on the material microstructure and the resulting effects of the microstructure thermo-mechanical and irradiation performance of additively manufactured W.

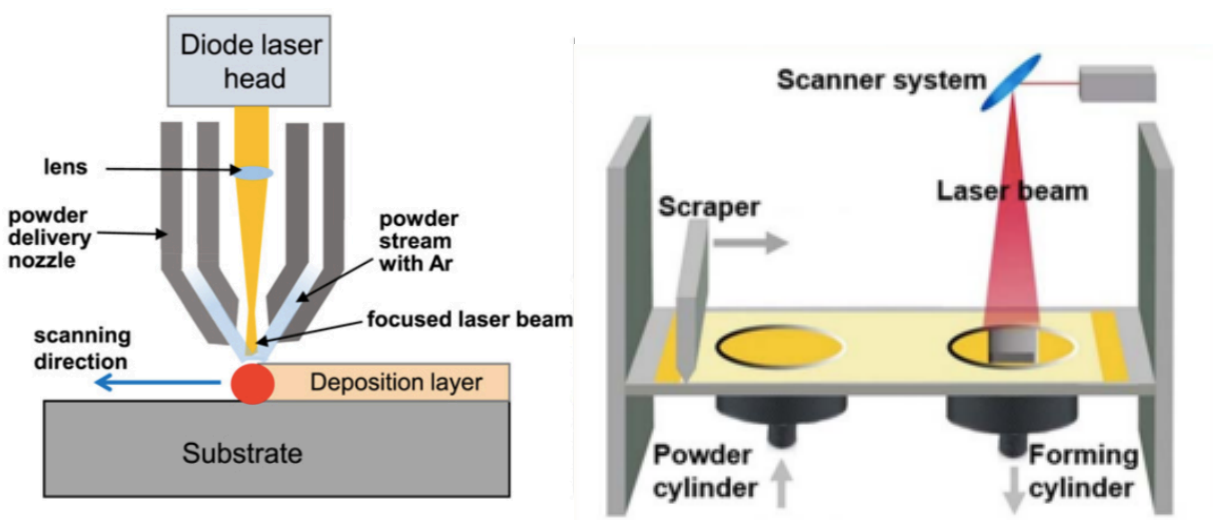

Figure 7.2: Schematics of different metal 3-D printing techniques showing how a laser beam can be rastered across a bed of metal powder to rapidly consolidate specimens [3,4].

Most work has focused on fabrication of pure W materials, and the technology is maturing. However, it may not be difficult to combine spheroidized W and TiC/ZrC/TaC powders in the desired concentrations, and feed them simultaneously through the SLM processing. This may be able to distribute dispersoids more evenly throughout the W matrix to be both within grains and at grain boundaries. Additive manufacturing techniques have been used to fabricated ODS steels [3, 12]. Issues regarding the agglomeration dispersoid powders need to be addressed, but sub-micron sized oxide particles have been observed to be uniformly distributed within a steel matrix. Therefore, additive manufacturing techniques have been used to fabricate dispersion-strengthened steels and it is not unreasonable to predict that similar techniques can be utilized to fabricated dispersion-strengthened tungsten.

Additionally, the size of SPS-fabricated samples is not an issue for laboratory-scale tests, but for use in a reactor, larger size components need to be fabricated. Larger spark plasma sintering devices exist and could be utilized to fabricate larger components, and may also be utilized to fabricate angled specimens or those with complex shapes. Three-dimensional printing techniques may be able to achieve larger dimensions and more complex geometries. For example, functionally graded materials and scaffolding geometries can be effectively fabricated via 3D printing technologies.

Further Irradiation Testing

Fundamental understandings of ion interactions with the dispersoid microstructure can be illuminated through *in-situ* irradiation experiments. Utilizing the *In-situ* Ion Irradiation TEM (I^3TEM) at Sandia National Laboratory – Albuquerque or the Microscope and Ion Accelerator for Materials Investigation (MIAMI) facility at the University of Huddersfield shown in Fig. 7.3, low energy (~keV) He bombardment can be performed on TEM specimens *in-situ* in the microscope. These experiments could allow for real-time understanding of the defect dynamics to track He bubble formation and accumulation at W-dispersoid interfaces and have been used to analyze defect dynamics in a variety of materials [13-15].

Other laboratory scale experiments can be performed to study the fundamental irradiation interactions that can mimic a fusion environment on a low fluence, lab scale. For example, the interactions of D and He must be further investigated. Irradiations were performed at Magnum-PSI on W-1.1ZrC and W-10ZrC samples. However, analysis of the materials can be performed to look at the D retention. The D trapping and release in the surface and bulk must be further examined through multiple techniques. Through multi-scale depth profiling analysis of direct recoil spectroscopy (DRS) combined with NRA and ERD, the D concentration in the near surface and up to 10 μm beneath the surface can be mapped. Additionally, Atom Probe Tomography can be applied to map the D distributions near dispersoids. These examinations can be performed after D irradiations, He-seeded D plasma exposure (95/5 D/He plasmas at 700 C at FZ-Juelich), and following heavy ion or neutron bombardment (at the Penn. St. University Neutron Beam Laboratory or Oak Ridge National Laboratory).

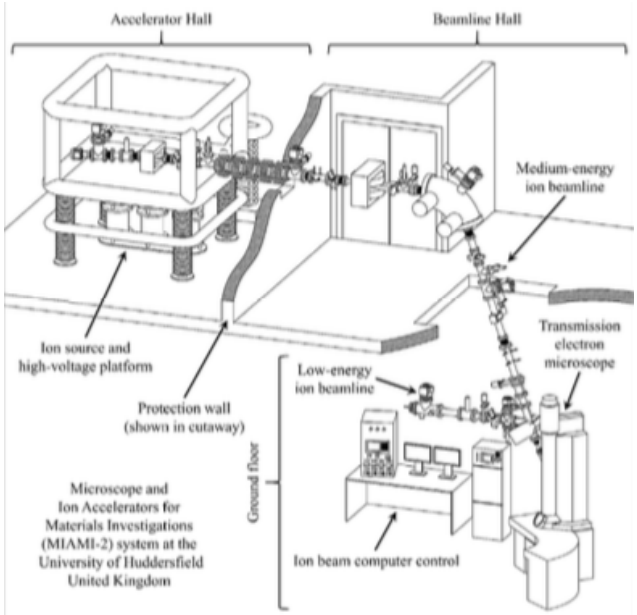

Figure 7.3: Schematic of the MIAMI-2 *in-situ* TEM facility at University of Huddersfield with dual-ion irradiation capabilities (low and high energy beam lines) [14].

Additionally, the combined effect of recrystallization and He irradiation can be examined. Previously annealed DS-W samples can be exposed to low energy He bombardment to investigate how the annealed microstructure responds to He implantation. Additionally, samples that have been exposed to He irradiation can be annealed at temperatures up to 1800 C to investigate the effect of the He bubbles on the recrystallization. Helium trapping visualization to confirm the conjecture of He trapping in TEM-invisible clusters within the dispersoids needs to be confirmed with Atom Probe Tomography investigations.

Finally, high energy (MeV-level) heavy ion irradiation can be performed on the DS-W materials. High energy heavy ion irradiation of ODS steels has shown dispersoid dissolution, amorphization, and shrinkage. Ion irradiation may also induce dispersoid chemical changes through ballistic dissolution [2, 16]. Therefore, it is important to understand how the dispersoid microstructure will respond to bulk irradiation to ensure dispersoid stability. Following heavy ion bombardment, the PMI properties such as D/He retention can be investigated to understand how bulk defect damage alters the trapping.

Moving beyond irradiation testing, there is a need to better understand basic PMI properties such as secondary electron emission. Secondary electron emission can drive plasma behavior at the plasma-material boundary that can correlate back to the bulk plasma behavior by affecting electron concentrations and temperatures in the plasma [17-19]. Secondary electron emission under ion bombardment can alter the sheath performance and have been studied on pure W under different surface conditions in a laboratory setting [20-22]. The IGNIS facility can be used to examine the secondary electron emission characteristics of DS-W materials under ion bombardment, as the secondary electron emission yields of DS-W materials has never been investigated.

Further thermal shock testing on the other alloy compositions beyond just W-1.1ZrC must be performed to gather a complete dataset to fully determine DS-W performance under thermal shocks. Using the JUDITH-II facility at FZ-Julich and the EB-60 facility at Penn. St. University,

high heat flux testing can be performed to expose samples to up to 10^4 MWm^{-2} heat fluxes to decipher the effect of dispersoid composition on the response to high heat fluxes.

High fluence exposures will be performed at the Material Plasma Exposure eXperiment (MPEX), or its precursor, proto-MPEX, at Oak Ridge National Laboratory, a schematic of which is shown in Fig. 7.4. This facility will be the largest linear plasma device in the world, capable to exposing samples to a 10^{24} $m^{-2}s^{-1}$ flux up to a $1x10^{31}$ m^{-2} fluence. Current operation of the device allows for a $5x10^{23}$ m^{-2} deuterium ion flux with a pure D plasma [23]. A key feature of MPEX is the ability to expose samples to angled irradiation (up to 45-degrees incidence) without tilting or biasing the sample, instead utilizing magnetic fields to produce angled ion bombardment that mirrors the incident angle of ions in the sheath in the divertor region of a tokamak [24]. Combined with the plasma-material interactions end-station, this facility will allow for examination of the surface morphology and chemistry changes that may result from long-time exposures to low energy ion bombardment.

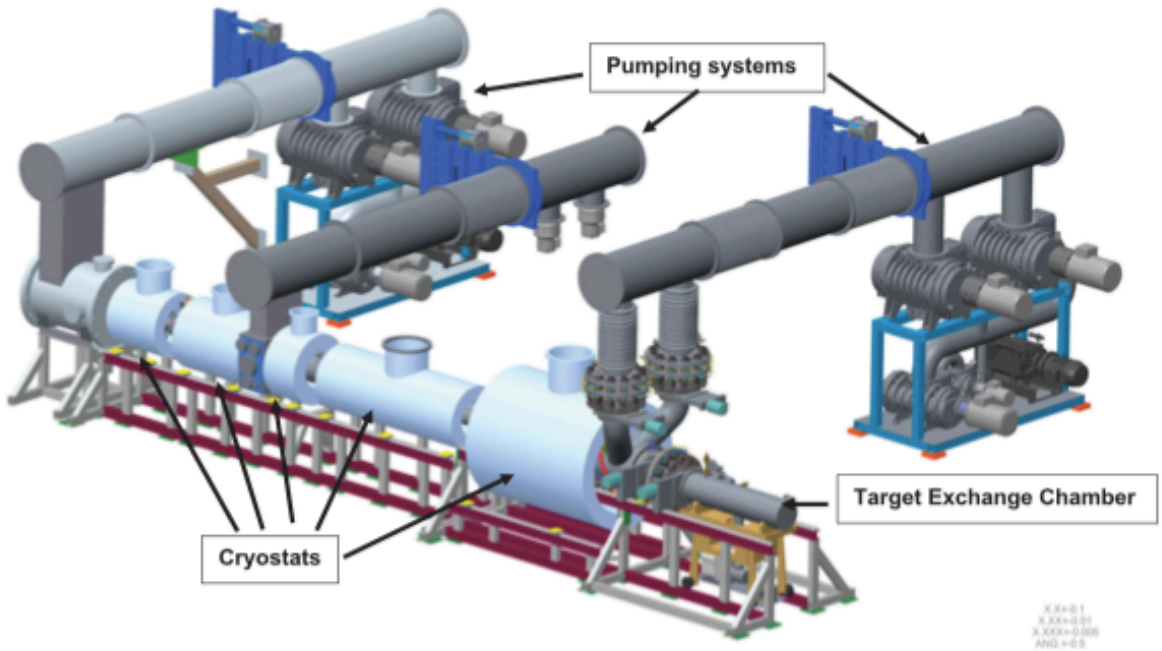

Figure 7.4: Schematic of the MPEX facility at Oak Ridge National Laboratory to be used for future high fluence plasma exposures [24].

Laboratory-scale experiments will help elucidate the fundamental physics mechanisms guiding the plasma-material interactions However, to best evaluate material performance in a reactor environment, exposures in a tokamak would offer the most realistic conditions to analyze material performance. To accomplish this, future exposures are planned using the DiMES (Divertor Material Evaluation System) probe on the DIII-D tokamak at General Atomics. Experiments plan to expose samples to D plasmas in the outer strike point (OSP) of the divertor region during both L-mode and H-mode discharges to simultaneously study the impact of ELMs. These experiments with quiescent and transient heat and particle fluxes that will cause erosion and re-deposition which will allow for the most accurate analysis of dispersion-strengthened W behavior in a fusion reactor environment. The DiMES probe allows for study of erosion and redeposition of W and dispersoid material via optical spectroscopies which would elucidate preferential erosion mechanisms of DS-W materials under tokamak operating conditions [25, 26].

Desired testing would include experiments that sweep the OSP over DiMES in quiescent vs ELMying plasma conditions. This would allow us to study the behavior of these materials under both steady-state plasma exposure and transient, off-normal events. Divertor Thompson Scattering (DTS) and other nearby Langmuir probes are desired. For measuring erosion, tracking of the Zr_I (360.1 nm), Ti_I (399.8 nm), Ta_I (271.4 nm), and W_I (400.8 nm) lines by a CMOS camera and MDS spectrometer system in-situ will allow for a measure of the erosion of these samples. Following exposure, thermal desorption spectroscopy can be performed to study the deuterium retention in DS-W materials to examine the impact of the plasma condition (ELMy vs. non-ELMy) on the deuterium retention.

In order to be effective in a fusion reactor environment, a plasma-facing material must not be catastrophically damaged by high neutron fluxes. Prior work has shown that Ta and Zr may be compatible with W in a fusion environment under neutron bombardment [27]. However, one must examine the changes in the material properties under neutron bombardment. To test the performance of dispersion-strengthened W samples in a neutron environment, select samples will be exposed in the High Flux Isotope Reactor (HFIR) at Oak Ridge National Laboratory. Through these studies, we wish to examine the impact of the dispersoids on the irradiation-induced hardening and effect on the Re/Os precipitation. In this work, the dispersoids are shown to be effective defect sinks under ion irradiation, but it remains to be seen if they will maintain their performance following neutron bombardment. Prior work has been performed on W-0.5TiC, K-doped, and La-doped W under neutron irradiation. These materials have shown similar black-dot and void damage, but may show reduced irradiation hardening as compared to pure W, while the second phase particles appear stable [28]. However, further testing must be performed on other DS-W materials to further examine the impact of dispersoid type and concentration on the response to neutron irradiation.

References

[1] S.J. Zinkle, et al. *Nucl. Fusion* **53** (2013) 104024 (13pp).
[2] S.J. Zinkle, et al. *Annu. Rev. Mater. Res*. 2008. **38**:471–503.
[3] B.M Arkhurst, *Korean J. Met. Mater.*, **55**, No. 8 (2017), pp.550-558.
[4] D. Gu, et al. *Int. J. Extrem. Manuf.* **2** (2020) 025001.
[5] A. Ivekovic, et al. *International Journal of Refractory Metals & Hard Materials* **72** (2018) 27-32.
[6] R.K. Enneti et al. *International Journal of Refractory Metals & Hard Materials* **71** (2018) 315–319.
[7] S. Wen, et al. *Optics and Laser Technology* **116** (2019) 128–138.
[8] C. Tan, et al. *Science and Technology of Advanced Materials* (2018) **19**, no. 1, 370–380.
[9] R. Enneti, et al. *International Journal of Powder Metallurgy* **53**, No. 4, 2017.
[10] R.E. Nygren, et al. *Fusion Engineering & Design* **136** (2018) 1007-1011.
[11] G. Yang, et al. *International Journal of Refractory Metals & Hard Materials* **84** (2019) 105040.
[12] H. Kim, et al. *Nuclear Engineering and Technology*, **46** No.4 August 2014.
[13] K. Hattar et al. *Nuclear Instruments and Methods in Physics Research B* **338** (2014) 56–65.
[14] J.A. Hinks, et al. *Journal of Vacuum Science & Technology A* **29**, 021003 (2011); doi: 10.1116/1.3543707.
[15] G. Greaves, A.H. Mir, R.W. Harrison et al. *Nuclear Inst. and Methods in Physics Research,*

A **931** (2019) 37–43.
[16] J.P. Wharry et al. *Journal of Nuclear Materials* **486** (2017) 11-20.

[17] P. Tolias, *Plasma Phys. Controlled Fusion* **56**, 123002 (2014).
[18] P. Tolias, *Plasma Phys. Controlled Fusion* **56**, 045003 (2014).
[19] J. P. Gunn, *Plasma Phys. Controlled Fusion* **54**, 085007 (2012).
[20] M. I. Patino, Y. Raitses, B. E. Koel, and R. E. Wirz, *J. Phys. D: Appl. Phys*. **48**, 195204 (2015).
[21] M. Patino *Appl. Phys. Lett.* **109** 2016, 201602.
[22] R. M. Chaudhri and A. W. Khan, *Proc. Natl. Inst. Sci. India* **7**, 197 (1941).
[23] C.J. Beers et al. *Fusion Engineering and Design* **138** (2019) 282–288.
[24] J. Rapp, A. Lumsdaine, C. J. Beers, T. M. Biewer, T. S. Bigelow, J. F. Caneses, J. B. O. Caughman, R. H. Goulding, N. Kafle, C. H. Lau, E. Lindquist, P. A. Piotrowicz, H. Ray & M. Showers and the MPEX Team (2019): Latest Results from Proto-MPEX and the Future Plans for MPEX, *Fusion Science and Technology*, DOI: 10.1080/15361055.2019.1610315.
[25] C.P.C. Wong, et al. *Divertor materials evaluation system at DIII-D*. *Journal of Nuclear Materials* **196-198** (1992) 871-875.
[26] D.L. Rudakov, et al. *DiMES PMI research at DIII-D in support of ITER and beyond*. Fusion Engineering and Design **124** (2017) 196–201.
[27] M.R. Gilbert, et al. *Nucl. Fusion* **51** (2011) 043005.
[28] M. Fukuda, et al. *Journal of Nuclear Materials* **442** (2013) S273–S276.

APPENDIX A: SPUTTER YIELD CALCULATIONS

To properly analyze the error in the sputtering yields, one must begin with an analysis of the uncertainty in the sputtering yield expression

$$Y = \frac{1}{DS^{QCM}Y\Omega mX_i}\frac{\Delta f}{f}M_{crystal}(1 + R_iY_i^{QCM}\Omega_i)$$

The uncertainty of a measurement is calculated by propagating the uncertainties of all variables during a measurement, a general expression of which is shown below.

$$u = \sqrt{\sum_i \left(\frac{\partial y}{\partial x_i}u_i\right)^2}$$

where u_i is the uncertainty y dependent on independent variables x_i that each have an uncertainty u_i. In analysis of the sputtering yield, the $M_{crystal}$ and $(1 + R_iY_i^{QCM}\Omega_i)$ terms do not contribute significantly to the error, so it is defined as a constant

$$C = M_{crystal}(1 + R_iY_i^{QCM}\Omega_i)$$

The subsequent partial derivatives of the yield Y with respect to each independent variable are:

$$\frac{dY}{dD} = \frac{-\Delta fC}{D^2f_iS^{QCM}\Omega mf}$$
$$\frac{dY}{df_i} = \frac{-\Delta fC}{Df_i^2S^{QCM}\Omega mf}$$
$$\frac{dY}{dS^{QCM}} = \frac{-\Delta fC}{Df_i(S^{QCM})^2\Omega mf}$$
$$\frac{dY}{d\Omega} = \frac{-\Delta fC}{Df_iS^{QCM}\Omega^2mf}$$
$$\frac{dY}{d\mathrm{m}} = \frac{-\Delta fC}{Df_iS^{QCM}\Omega m^2f}$$
$$\frac{dY}{d\mathrm{f}} = \frac{-\Delta fC}{Df_iS^{QCM}\Omega mf^2}$$
$$\frac{dY}{d\Delta f} = \frac{C}{Df_iS^{QCM}\Omega mf}$$

After determining the partial derivatives, the uncertainties in the measurements must be undertaken. The uncertainty in the dose is determined by

$$uD = \sqrt{(Ip \cdot uI)^2 + (tp \cdot utp)^2}$$

where *Ip=t/q, tp=I/q, utp=0.5 sec, and uI=0.5 nA.* The uncertainty in time is defined as 0.5 seconds, while the uncertainty in the current measurement is 0.5 nA. The partial derivative of the current and time are defined with respect to the total time and current of the measurement, and the fundamental charge q.

The uncertainty in the sticking coefficient, *uS* requires analysis of the reflection coefficient. The reflection coefficient *R* is defined as *R=1-S* where *S=0.9.* The uncertainty in *R* is

defined as *uR=0.5R* and the partial derivative *Rp=-1*. Overall the uncertainty in the sticking coefficient *uS=(Rp)(uR)=0.08*.

Uncertainty in the solid angle depends on approximating the fraction of the solid angle subtended by the crystal which requires analysis of the distance from the crystal to the sample. This requires approximating the uncertainty and differentials in the distance to the crystal:

$$dp=0.4$$
$$Lp=1.2$$
$$uL=0.1$$
$$ud=0.1$$
$$u\Omega = \sqrt{(dp \cdot ud)^2 + (Lp \cdot uL)^2}$$

The uncertainty in the mass of tungsten is defined as *um=0.005 g/mol.* The uncertainty in the original crystal frequency and difference in the frequency are defined as *uf=0.5 Hz* and *udf=0.5 Hz*.

Combining all of these terms gives the total uncertainty in the sputtering yield.

$$uY = \sqrt{(uD \cdot Dp)^2 + (ufi \cdot fip)^2 + (uS \cdot SCp)^2 + (u\Omega \cdot \Omega p)^2 + (um \cdot mp)^2 + (udf \cdot dfp)^2 + (uf \cdot fbp)^2}$$

These calculations were carried out for all sputtering yield measurements [1].

In addition to calculation the D-induced sputtering yields (Ch. 4) and He-induced sputtering yields (Ch. 5), the sputtering yields under Ar and Ne were also calculated. Argon sputtering measurements were used to calibrate the sputtering setup. First, to determine the integrity and experimental accuracy of the setup, calibration experiments were performed first on pure W. Sputtering was performed with 2 and 3 keV Ar on W at 12.5-72.5 degrees. The sputtering yields under angled bombardment are shown in Fig. A.1.

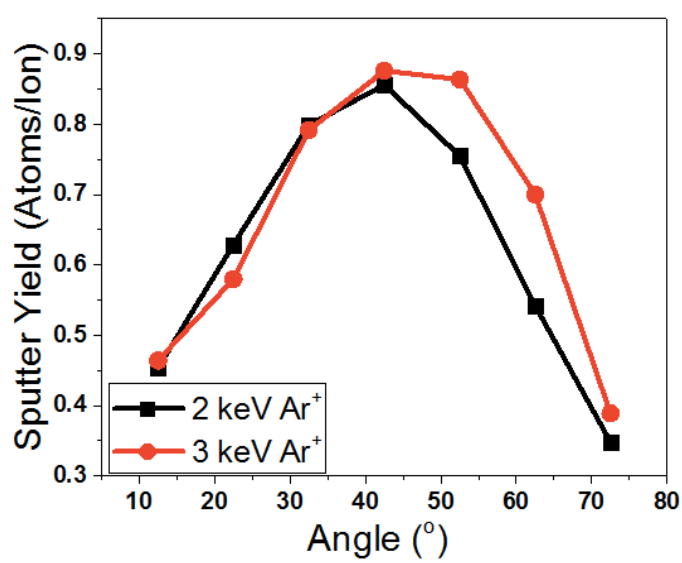

Figure A.1: Sputtering yields for Ar^+ on ITER-W for different angles and Ar^+ energies, as indicated.

As shown in Fig. A.2, the yields for 2 and 3 keV Ar^+ on W align reasonably well with the literature values. At 45° incidence, the yield for 3 keV Ar^+ on W is cited to be ~0.9 atoms/ion [2]. In IGNIS for Ar^+ on W, a value of 0.87 atoms/ion is measured for 3 keV Ar^+. Thus, our setup is reliable and robust enough to be used for further investigations.

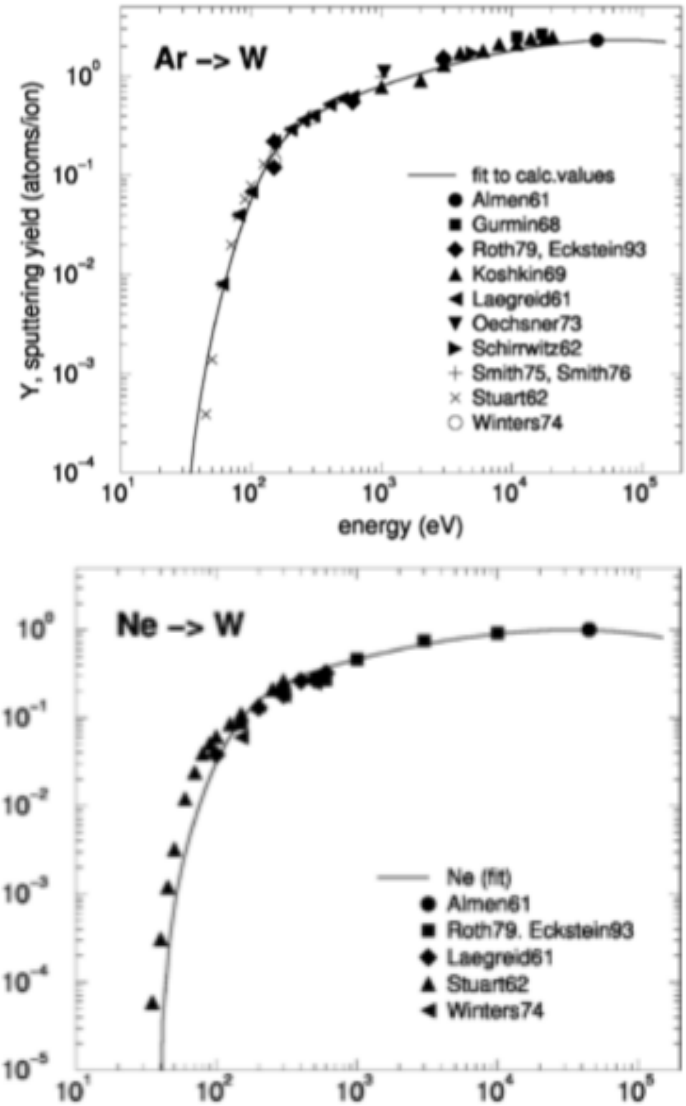

Figure A.2: Sputtering yield versus energy for Ar and Ne on W indicating that the yield for 3 keV Ar^+ on W is ~1.0 and 500 eV Ne^+ on W is ~0.2 [2].

The sputtering yields of the dispersion-strengthened W materials under 3 keV Ar^+ were subsequently calculated. Table 1 below shows the calculated sputtering yields.

Table A.1: Argon-induced and neon-induced sputtering yields of dispersion-strengthened W samples under 3 keV Ar^+ bombardment at 45-degree incidence and 500 eV Ne^+ bombardment at 30-degree incidence.

Sample	Ar Yield (atoms/ion)	Ne Yield (atoms/ion)
W Literature	~1.00	~0.20
ITER-W	0.99	0.28
W-10ZrC	1.01	0.30
W-10TiC	0.84	0.29
W-10TaC	0.98	0.33
W-1ZrC	1.08	0.36
W-1TiC	0.93	0.29
W-1TaC	0.98	0.31

The change in surface composition was also tracked in real-time during the Ar sputtering with XPS. Surface concentration evolution over the Ar irradiation fluence shown in Fig. A.3 shows that the 3 keV Ar^+ did not significantly alter the starting surface composition. The surface is stable under room temperature argon irradiation, indicating that no preferential erosion occurs at the irradiation fluences tested.

In summary, sputtering investigations of DS-W materials under low energy Ar and Ne bombardment were investigated. The sputtering yields of DS-W materials are similar to those of pure W, indicating that the DS-W materials do not have enhanced sputtering. *In-situ* XPS studies following Ar sputtering show that the DS-W materials do not have preferential sputtering, as the surface composition is stable across a $6x10^{16}$ cm^{-2} fluence.

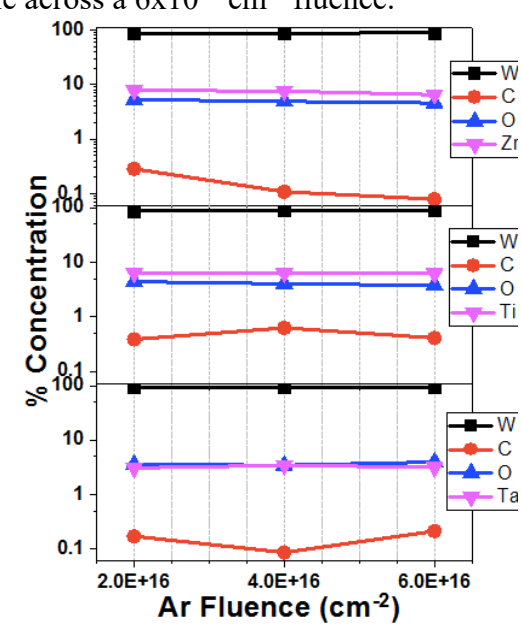

Figure A.3: Change in surface composition of 10wt.% alloys as a function of incident Ar^+ fluence. No significant change in the surface composition is observed.

References

[1] J.P. Allain. *Kinematic and Thermodynamic Effects on Liquid Lithium Sputtering.* Ph.D. Dissertation. University of Illinois. 2001.

[2] W. Eckstein, R. Behrisch. *Topics in Applied Physics 110: Sputtering by Particle Bombardment.* Springer. Berlin, 2007.

APPENDIX B: ESHELBY CALCULATION

Eshelby calculations were carried out to estimate the magnitude of thermal stresses induced due to the high heat flux pulses. The problem was modeled as an Eshelby inclusion problem, with the interaction volume of the heat affected zone beneath the surface being modeled as the inclusion. Additionally, since the samples that were tested were W-1.1ZrC and these 98.9%W by mass and 97% by volume, material properties for bulk W were used, instead of a rule of mixtures for W and ZrC. While the values such as bulk modulus and thermal expansion coefficient of pure W likely differ from those of a W-ZrC alloy, the differences are assumed to be slight enough that the effects on these calculations will not impact the relative magnitude.

The heat affected zone was modelled as an ellipsoidal inclusion, as shown in Fig. B.1.

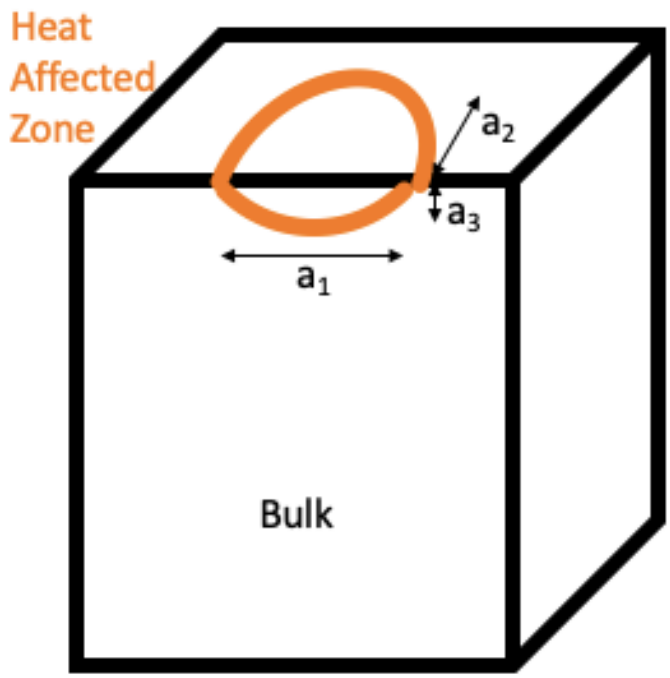

Fig B.1: Model of Heat Affected Zone Eshelby calculation. The black box represents the W-1.1ZrC sample that was bombarded with the laser high heat flux pulse. The orange region represents the heat affected zone by the laser pulse where a_1 and a_2 represent the area of the pulse on the surface while a_3 represents the depth of the heat affected zone into the sample bulk.

In the calculation the dimensions for the ellipsoid were calculated by analyzing the area of the heat affected zone on and beneath the sample surface, and were determined to be a_1=3mm, a_2=2.8mm, a_3=250µm.

To calculate the stresses induced in a thermoelastic Eshelby inclusion, the bulk modulus and thermal expansion coefficient are needed at the temperatures of the bulk sample and inclusion, respectively [1, 2]. Table B.1 below shows the bulk modulus and thermal expansion coefficient of pure W at different temperatures of interest for these high heat flux-exposed samples.

Table B.1: Bulk modulus and thermal expansion coefficient of pure W at given temperatures [3].

Temperature [K]	Bulk Modulus [GPa]	Thermal Expansion Coefficient [x10^{-5} K^{-1}]
300	311.8	1.33
700	304.4	1.49
1300	293.0	1.62
1600	286.4	1.75
1800	282.1	1.83
2200	273.1	2.04
3400	240.4	3.13
3700	230.7	3.57

The general relation for thermoelastic properties for an Eshelby inclusion calculation is

$$e^{(h)} = S^{(h)}\sigma + \beta^{(h)}\theta$$

Where σ is the applied external stress, $S^{(h)}$ is the compliance tensor of the host material, $\beta^{(h)}$ is the thermal expansion coefficient of the host material, and θ is the temperature change. When a uniform strain occurs in the inclusion leads to uniform expansion or contraction in the composite and inclusion, the strain e in the inclusion can be written as

$$e^{(h)} = \frac{\theta}{3K^{(i)}}(X - 3\beta^{(i)}K^{(i)})$$

where $K^{(i)}$ is the bulk modulus of the inclusion, $\beta^{(i)}$is the thermal expansion coefficient of the inclusion, and X relates the thermal and mechanical properties of the inclusion and host:

$$X = 3\frac{\beta^{(h)} - \beta^{(i)}}{\frac{1}{K^{(h)}} - \frac{1}{K^{(i)}}}$$

$S^{(h)}$ is the Eshelby tensor and is a function of the elastic properties of the solid and the dimensions of the ellipsoid. The components of the tensor can be calculated as:

$$S^*_{1111} = \frac{3}{8\pi(1-v)}a_1^2 I_{11} - \frac{1-2v}{8\pi(1-v)}I_1$$

$$S^*_{1122} = \frac{3}{8\pi(1-v)}a_2^2 I_{12} - \frac{1-2v}{8\pi(1-v)}I_1$$

$$S^*_{1133} = \frac{3}{8\pi(1-v)}a_3^2 I_{13} - \frac{1-2v}{8\pi(1-v)}I_1$$

$$S^*_{1212} = \frac{a_1^2 + a_2^2}{16\pi(1-v)}I_{12} - \frac{1-2v}{16\pi(1-v)}(I_1 + I_2)$$

Where the *I's* can be calculated as

$$I_1 = \frac{4\pi a_1 a_2 a_3}{(a_1^2 - a_2^2)(a_1^2 - a_3^2)}F(\theta, k)$$

$$I_3 = \frac{4\pi a_1 a_2 a_3}{(a_2^2 - a_3^2)(a_1^2 - a_3^2)}\left\{\frac{a_2(a_1^2 - a_3^2)^{\frac{1}{2}}}{a_1 a_3} - E(\theta, k)\right\}$$

Where

$$F(\theta, k) = \int_0^b \frac{dw}{(1 - k^2\sin^2 w)^{1/2}}$$

$$E(\theta, k) = \int_0^b (1 - k^2\sin^2 w)^{1/2}\, dw$$

$$b = \sin^{-1}\left(1 - \frac{a_3^2}{a_1^2}\right)$$
$$k = \frac{a_1^2 - a_2^2}{a_1^2 - a_3^2}$$
$$I_1 + I_2 + I_3 = 4\pi$$
$$3I_{11} + I_{12} + I_{13} = \frac{4\pi}{a_1^2}$$
$$3a_1^2 I_{11} + a_2^2 I_{12} + a_3^2 I_{13} = 3I_1$$
$$I_{12} = \frac{I_2 - I_1}{a_1^2 - a_3^2}$$

From the quantities given in Table B.1, these quantities were calculated. The stresses in different directions can then be calculated [1-3]. Based on these calculations, the maximum stresses are calculated to be ~100-900 MPa, depending on the bulk temperature and the temperature rise incurred in the heat affected zone, given in Table B.2. Therefore, the thermal stresses introduced may be larger than the material strength at 1000°C, which may be the cause for the cracking observed on the W-1.1ZrC specimens exposed to laser pulsing at 1000°C base temperature.

Table B.2: Estimated maximum stresses incurred in the heat affected inclusion as a result of the high heat flux pulses.

Sample (W-1.1ZrC)	**Spot**	**Power Density (GW m^{-2})**	**Estimated Temperature Rise (C)**	**Estimated Stress in heat-affected zone (MPa)**
30 C	**1**	0.19	400	120
	2	0.38	800	440
	3	0.38	800	440
	4	1.9	3000	890
400 C	**1**	0.19	400	70
	2	0.38	800	170
	3	0.38	800	170
	4	1.9	3000	960
1000 C	**1**	0.19	400	110
	2	0.38	800	225
	3	0.38	800	225
	4	1.9	3000	1060

References

[1] J.G. Berryman. *Generalization of Eshelby's Formula for a Single Ellipsoidal Elastic Inclusion to Poroelasticity and Thermoelasticity.* Lawrence Livermore National Laboratory. UCRL-JC-126047 (1997).
[2] A.F. Bower. *Applied Mechanics of Solids.* CRC Press, 1st Edition, 2009.
[3] P.I. Dorogokupets, et al. *Petrology* **7** (1999) 574–591.